Award Number: **W81XWH-12-1-0591**

TITLE: **Organizing the Cellular and Molecular Heterogeneity in High-Grade Serous Ovarian Cancer by Mass Cytometry**

PRINCIPAL INVESTIGATOR: **Garry P. Nolan, Ph.D.**

CONTRACTING ORGANIZATION: **The Leland Stanford Junior University**
Standford, CA 94305

REPORT DATE: **October 2017**

TYPE OF REPORT: **Annual**

PREPARED FOR: **U.S. Army Medical Research and Materiel** Command
Fort Detrick, Maryland 21702-5012

REPORT DOCUMENTATION PAGE

Form Approved
OMB No. 0704-0188

1. REPORT DATE	**2. REPORT TYPE**	**3. DATES COVERED**
October 2017	Annual	30 Sep 2016 - 29 Sep 2017

4. TITLE AND SUBTITLE
Organizing the Cellular and Molecular Heterogeneity in High-Grade Serous Ovarian Cancer by Mass Cytometry

5a. CONTRACT NUMBER

5b. GRANT NUMBER
W81XW H-12-1-0591

5c. PROGRAM ELEMENT NUMBER

6. AUTHOR(S)
Garry P. Nolan,
Ph.D.
gnolan@stanford.edu
Wendy J. Fantl,
Ph.D.
wifantl@stanford.edu

5d. PROJECT NUMBER

5e. TASK NUMBER

5f. WORK UNIT NUMBER

7. PERFORMING ORGANIZATION NAME(S) AND ADDRESS(ES)
The Leland Stanford Junior University
Stanford, CA 94305-2004

8. PERFORMING ORGANIZATION REPORT NUMBER

9. SPONSORING / MONITORING AGENCY NAME(S) AND ADDRESS(ES)
U.S. Army Medical Research and Materiel Command
Fort Detrick, Maryland 21702-5012

10. SPONSOR/MONITOR'S ACRONYM(S)

11. SPONSOR/MONITOR'S REPORT NUMBER(S)

12. DISTRIBUTION / AVAILABILITY STATEMENT
Approved for Public Release; Distribution Unlimited

13. SUPPLEMENTARY NOTES

14. ABSTRACT
Tumor heterogeneity in high grade serous ovarian cancer (HGSOC) represents a significant barrier for successful therapeutic intervention. To further understand the cell types contributing to this heterogeneity we performed a comprehensive phenotypic characterization of 22 primary ovarian tumor samples. Our unsupervised analysis revealed shared and circumscribed patterns of tumor cell types across multiple HGSOC primary samples. In addition to identifying cells characteristic of epithelial tumors we found several repeatedly observed, though previously unrecognized, cell types. These included three unique E-cadherin-expressing cell subsets, cell subsets co-expressing E-cadherin and vimentin and critically one subset that co-expressed high levels of all stem cell markers interrogated. Poorer prognosis tumors had an increased frequency of cells co-expressing vimentin, HE4 and cMyc and also showed greater overall phenotypic heterogeneity quantified by Simpson's Diversity Index. Importantly the novel cell types identified have the potential to become a focus for developing new therapies as well as a means of monitoring the disease.

15. SUBJECT TERMS- Tumor initiating cells, Modularity Optimization in Networks of Cellular Phenotypes (MONOCLE), primary diagnostic samples, Indivumed, dissociation conditions, evaluation of viability and apoptosis, immunohistochemistry, validation of tumor antibodies, validation of immune cell antibodies, ovarian cancer cell lines, future plans.

16. SECURITY CLASSIFICATION OF:			**17. LIMITATION OF ABSTRACT**	**18. NUMBER OF PAGES**	**19a. NAME OF RESPONSIBLE PERSON**
a. REPORT	**b. ABSTRACT**	**c. THIS PAGE**			**19b. TELEPHONE NUMBER** *(include area code)*
U	U	U	UU	52	USAMRMC

Table of Contents

Page

INTRODUCTION

High-grade serous ovarian cancer (HGSOC) is the fifth most lethal cancer in women and the most lethal of gynecological malignancies[4,5]. Most often diagnosed at more advanced stages, a great challenge in treating HGSOC is the apparent large number of disease subclasses based on genetic analyses[4,6-9]. Defective DNA repair mechanisms are characteristic of the disease and are most likely responsible for the extensive genetic abnormalities, most frequent of which are focal copy number alterations and epigenetic modifications, confounding a systematic approach to successful treatment the disease. Furthermore, given the genetic plasticity of HGSOC each patient can manifest one disease at diagnosis and other subtypes over time. At present, platinum-based therapeutic regimens are the most commonly used in the clinical settings of first diagnosis and relapse. Frequently, a more aggressive platinum resistant form emerges. According to a seminal review by Vogelstein et al. the vast array of genetic events found in cancer all converge on three essential cellular processes, cell fate, cell survival and genome maintenance all regulated by twelve intracellular signaling pathways[10]. This is consistent with cancer having a "structure".

The hypothesis of our DoD proposal is that in spite of the vast range of genetic aberrations detected in HGSOC, there must exist a unifying architecture that links biology to pathology across these tumors. By dissecting diagnostic, chemo-naïve clinically annotated HGSOC primary samples into single cells for analysis of their phenotypes and signaling states, at the *deepest possible resolution currently available*, we will provide a unifying vision of *ovarian cancer "systems biology"* to bring about more informed changes to treatment modalities. To accomplish this vision with HGSOC, we are using a single cell technology, mass cytometry, or CyTOF (**Cy**tometry by **T**ime-**O**f-**F**light), largely developed in our laboratory, for immunologic and cancer cell studies[11-15]. CyTOF uses antibodies conjugated to chelated metal ion tags, allowing for the simultaneous measurement of up to 40 parameters on a cell-by-cell basis, including surface markers and intracellular signaling proteins. CyTOF has been applied to complex tissues such as blood, bone marrow and, recently, ovarian ascites as well as single-cell suspensions derived from primary HGSOC tumors.

Over the past reporting period (2016 to 2017), we have greatly expanded the scope of our analysis and revealed new information about the relationships between the novel tumor and immune cell types we identified which has led to enhanced understading of HGSOC biology and has promising clinical potential. One of our findings (described in last year's progress report) regarding a new cell type we discovered that co-expresses vimentin/HE4 and cMyc is in the process of being licensed for conversion into a diagnostic test. This will be discussed below as well as the new data from our analysis of the tumor immune infiltrate and how the relationship between the tumor immune cells and the vimentin/HE4/cMyc cells may have important clinical implications. Our manuscript entitled: "Commonly occurring cell subsets in high grade serous ovarian tumors identified by single-cell mass cytometry" is in revision. The abstract will be included in the body of this report and the manuscript itself will be submitted in the Appendix.

Text in green font is the update of aims for this year's report with updates from our 2014 report (red font) from our 2015 report (blue font) and in this current 2016/2017 report in maroon font. Within the body of the text, a detailed discussion will be provided for our progress over the last year, which continues to build on **Task1** as well as report on studies initiated for **Task 2** and some exciting new findings in our tumor immune studies in **Task 3.**

KEYWORDS
Serous ovarian cancer, primary tumors, mass cytometry, single cell, antibodies, stem cells, heterogeneity, epithelial mesenchymal transition, relapse, platinum resistance, Simpson's Index of diversity, vimentin/HE4/cMyc, immune compartment, clustering, correlation analyses, diagnostic, PARP inhibitor, decidual-like NK cells, NK cell ligands, T cells, macrophages, immune checkpoints.

OVERALL PROJECT SUMMARY

A. Background

Single mass cytometry facilitates high-dimensional, quantitative analysis of the effects of bioactive molecules on cell populations at single-cell resolution[11-15]. Datasets are generated with panels of 41 optimized antibodies, in which each antibody is conjugated to a polymer chelated with a stable metal isotope, usually in the Lanthanide series of the Periodic Table[12,14,16]. The antibodies recognize surface markers to delineate cell types, such as immune, epithelial, mesenchymal, and intracellular signaling molecules demarcating multiple cell functions such as survival, DNA damage, cell cycle and apoptosis. By measuring all these parameters simultaneously, the signaling network state of an individual cell can be measured. The ultimate goal of this work, and beyond, will be to assign molecular status and function to cell subsets defined by 40 parameters at the single cell level. Over the course of this award the focus of our work has been on characterizing the tumor and tumor-immune infiltrating immune cells and their relationships with one another. We identified new cell types, new therapeutic targets, a potential diagnostic test and some important new insights regarding HGSOC biology. Furthermore, during the time of this grant PARP inhibitors emerged as one of the most promising therapies in decades for HGSOC patients and therefore we developed mass cytometry antibody panels with which to study DNA damage in HGSOC at the systems-level. **The work is now published in Cell Reports (Gonzalez et al. 2018 22(7):1875-1888), was selected as an issue highlight and press release from Stanford.** (See further down in this report).

B. Overview of status of tasks

Task 1

Subtask 1a. Establish conditions for dissociation of solid tumors into single cells that maintain cells' ability for functional signaling. **Done with protocols transferred to Indivumed Inc, Hamburg Germany and now routine. We continue to procure de-ideintified samples from Indivumed who are now the preferred provider of quality samples to the NCI. Our protocols for HGSOC tumor dissociation are now in the form of established SOPs.**

Subtask 1b. Select a panel of extracellular modulators with which to measure signaling responses in both tumor cells and peripheral blood cells. **A preliminary list of modulators has been made including but not limited to, TBF□, BMP2, EGF, TGF□, heregulin, amphiregulinn, LPA, IL6, LPS, IL6, IFN□, and IFN□ has been made and protocols for exposing single cell dissociation of primary tumors are in the process of being transferred to Indivumed. Work in progress is prioritizing this list. This next phase will involve transferring our protocols to Indivumed which is planned for later in the year. We are currently performing studies with HGSOC cell lines treated with TBF□□as a means to monitor EMT and recapitulate the findings of the cell types we identified in primary tumors that co-express E-cadherin and vimentin. This will permit us to design in vitro models and iterate back to tumors. We have optimized a set of cytokine "cocktails" that can be used to interrogate peripheral whole blood for phosphorylation of intracellular signaling molecules incorporating the major immune cell pathways. The versatility of these cytokines makes them relevant to the study of blood matched with HGSOC tumor samples either in the context of a clinical trial or from a purely discovery-based study.**

Subtask 1c. Select two panels of ~40 antibodies each. Done. **We constructed two antibody panels in which**

the second was a variant of the first based on a mass cytometry experiment with six primary samples. *The data from two independent experiments with each panel will be described in the body of the text.* We assembled three panels with 40 antibodies each. One panel was focused on the tumor cells and the two others on the tumor-immune infiltrate. Throughout the duration of this award we have validated and optimized hundreds of metal-polymer conjugated antibodies resulting in our ability to assemble multiple CyTOF panels interrogating multiple biological functions of HGSOC.

Subtask 1d. We have submitted the necessary HRPO (IRB) and the ACURO and are awaiting approval. **Done.**

Subtask 1e*.* Acquire 10 primary diagnostic (no treatment) ovarian tumor or ascites samples with matched blood samples. **Done. We have performed two mass cytometry experiments: i) six primary naïve tumors and ten HGSOC ovarian cell lines described to be genetically most similar to primary HGSOC[3]. We acquired 22 samples which were all processed for CyTOF with the three antibody panels. Unfortunately, the matched blood was destroyed during shipment.**

Subtask 1f*.* Develop and apply new informatics tools and algorithms to the data generated from subtask 1d (Nolan lab and Pe'er lab at Columbia) (these efforts will be ongoing throughout mos of the duration of this award) **New tools developed: from the Nolan Lab: Citrus[17], X-shift[18], Gatefinder (unpublished), Pe'er Lab: DREMI[19]. A manuscript describing X-shift has been submitted and a manuscript about gatefinder is accepted for publication in nature Biotechnology. We are using these algorithms in combination with standard statistical tools for analyzing our data. The X-shift clustering algorithm specifically developed for CyTOF datasets was published earlier this year in Nature Methods[18].**

Subtask 1g*.* Pending data from subtask 1e modify antibody panels. Titrate any new antibodies (3-36 months. Anticipate continuous low-level activity for this subtask throughout the award period). ***See subtask 1c.*** **Our three new and modified antibody panels include new antibodies which were all conjugated and titrated. Concentrations where signal to noise was maximal were selected for our CyTOF experiments. The antibody panels were finalized last year and activities surrounding panels were replenishments. As mentioned above we validated several hundred antibodies during the course of this proposal.**

Subtask 1h*.* Acquire >er than 150 primary diagnostic (Neel lab at UHN Toronto, and Berek at Stanford) serous ovarian cancer samples (from Neel at UHN and Berek at Stanford) and process for mass cytometry with modified panels (6-40 months). Twenty five of these will be processed for xenotransplant (the Neel Lab currently has Research Ethics Board approval to conduct all of the tests described), requiring 10 mice for each subject tumor for 250 mice. **In progress. Continues in progress. Continues.**

Subtask 1i*.* Using SPADE and other algorithms, segregate and aggregate cell subsets in hierarchical pattern with intracellular and cell surface marker combinations. **Using a new deterministic K-nearest neighbor-clustering algorithm, called X-shift we see important relationships between tumor cell subsets. This information will be presented in the body of the text. We analyzed the new set of 22 HGSOC samples with this algorithm and noted some new findings especially as they pertain to the tumor and immune cell compartments. This analysis will be presented. The new analysis from of the last reporting period identified key attributes of HGSOC tumors and this work will be presented. Further mechanistic insight around HGSOC revealed from a variety of correlation analyses.**

Subtask 1j*.* Building of subset space in relationship to therapy/outcome (6-48 months). **We have not run enough samples and also for those we have run, not enough time has elapsed to fully evaluate patient outcome. We are expecting the outcomes data regarding platinum sensitivity in the next couple**

of weeks and may not be able to incorporate those findings into this report. We have identified a tumor cell subset that pre-exists in diagnostic samples that is predicts relapse. Additionally we have quantified heterogeneity using the Simpson's index of diversity that considers HGSOC tumors as an ecosystem. We have revealed new relationships between tumor cells with themselves, immune cells with themselves and tumor cell with immune cells. This will be discussed in the body of this eport.

Subtask 1k. Assess relative tumor-initiating properties of cell subsets from subtask 1h with established quantitative xenograft assay (Neel lab, 6-40 months). **In progress. In the next year we plan to FACS-sort the three new tumor cell subsets we identified and perform functional studies such as growth in soft agar combined with patient-derived xenograft models.**

Task 2

Previous work from the Nolan group showed that measuring the signaling responses of cancer cells to perturbations is more informative than assessing basal phosphorylation states. This task is focused on measuring signaling responses to extracellular perturbants such as growth factors, cytokines and drugs with relevance to ovarian cancer. In this task, the objective will be to uncover druggable pathways in serous ovarian cell subsets within and across primary samples.

Task 2 has subtasks that are dependent and independent of Task 1. For Task 2 we have set up foundational studies to measure drug responses in HGSOC cell lines. Specifically, we have set MTT assays (colorimetric readout) to measure the effects of drugs on proliferation, and growth in soft agar assays. We are evaluating carboplatin and paclitaxel and other investigational agents such as PARP inhibitors, JQ1 (an epigenetic modifier) and others that are under evaluation based on our primary tumor work in Task 1. Due to the relative immaturity of these studies, we will focus this report on the 1c, g and i. **We have established growth in soft agar assays using HG- SOC cell lines for evaluating their tumorigenic potential with and without drugs. In the past few months we have focused on PARP inhibitors. The assays is ready for application to cell subsets isolated from primary tumors which is imminent. Over the last year we have directed our drug studies around two classes of targeted inhibitors, the data of which will be presented. The first is the screening of HGSOC cell lines with bromo-domain inhibitors based on our CyTOF analysis. The second class is the PARP inhibitors, in recognition of their surge into the clinic for HGSOC patients. Data from our PARP inhibitor and bromodomain studies will be presented.**

Task 3

Although the presence of infiltrating cytotoxic T cells correlates with good prognosis, whereas regulatory T cells correlate with poor prognosis in SOC, there is limited understanding of the factors that contribute to the generation of these opposing responses. Understanding the mechanisms by which a given tumor microenvironment is able to promote immune surveillance could eventually lead to the clinical development of biomarkers that could select patients responsive to immune therapy. We will use mass cytometry to evaluate the tumor microenvironment in the same SOC samples as above utilizing antibodies against immune cell subsets. **We analyzed 22 HGSOC primary samples from Indivumed with two panel focused on the immune infiltrate. The panels included checkpoint inhibitors and the data will be presented in detail. From our continued analysis we identified a subset of NK cells that correlated with tumor cell abundance. We provide our detailed analysis regarding the interplay between NK cells and specific tumor cell subsets that importantly identify potential new targets for HGSOC. We have a deeper correlation analysis that has revealed intriguing relationships between the tumor immune infiltrate with the new tumor cell types we identified. Our analysis of the intracellular pathways continues.**

Subtask 3a. Assemble panel of extracellular modulators based on the known biology of the cell types that infiltrate ovarian tumors; immune cells, endothelial cells and stromal cells. **Ongoing *Subtask 3b***. Validate reagents to monitor signaling pathways mediated by extracellular modulators in cell lines and peripheral

blood. (1-24 months). **We have available a large repository of agents (growth factors, cytokines and drugs) with which to characterize immune cell subsets from peripheral blood taken from HGSOC patients. We are currently prioritizing which agents to use. Ongoing. See Task 2**

Subtask 3c*.* Acquire 10 primary serous ovarian cancer samples with which to test response of tumor infiltrating cells to extracellular modulators identified in 3a. **(Ongoing). Ongoing. Ongoing. Ongoing.**

Subtask 3d. Culture tumor-infiltrating lymphocytes from samples in Subtask 3c and characterize them for cytokine and chemokine production. (Ohashi lab 12-24 months). **This subtask has changed and the Nolan Lab is generating enriched immune fractions from primary tumors and establishing in vitro assays to determine immune-suppressive versus immune-enhancive activities of the tumor immune compartment. Based on our data with the tumor immune cell infiltrate (discussed in the body of the text) we are following up with our findings regarding NK cell subsets and performing co-culture experiments between peripheral NK cells and HGSOC cell lines which are discussed in the text below. Data will be presented. New data will be presented co-culturing HGSOC cell lines with immune cells.**

Subtask 3e*:* Acquire >er than 150 primary serous ovarian cancer samples (Neel lab at UHN Toronto, and Berek at Stanford) with which to test response of tumor infiltrating cells to extracellular modulators identified in 3a. (24-50 months). **In progress.**

Subtask 3f*.* Culture tumor-infiltrating lymphocytes from samples in Subtask 3c and characterize them for cytokine and chemokine production. **See Subtask 3d. Data will be presented below.**

Subtask 3g*:* Using SPADE and other algorithms, segregate and aggregate tumor infiltrating cell subsets in hierarchical pattern with intracellular and cell surface marker combinations. Build computational models that correlate intracellular signaling responses in tumor infiltrating cell subsets with intracellular signaling responses of tumor cells with clinical outcomes (12-60 months). **In progress and update will be in body of text. This is a continuous activity for us and the latest data will be discussed in the text below. New data analysis will be presented.**

C. Description of studies and results

The bulk of this report will describe the continued data analysis of 22 primary OC tumor samples with over 100 antibodies providing, to date, the most comprehensive single cell proteomic analysis of HGSOC that examines both the tumor and immune cell compartments. One major result to emerge is that the heterogeneity of HGSOC is far more circumscribed than would be predicted. Application of single cell CyTOF has identified three new cell types that define this more limited heterogeneity and of greatest relevance to patients we identify potential new therapeutic targets. In addition we shed new light on tumor-immune cells and suppression of the host immune system.

C.1 Introduction and Background

As in years 1, 2, 3 and 4 we continue to pay close attention to obtaining samples of the highest quality, minimizing their ischemic time and optimizing all pre-analytical variables. This has been discussed in the previous progress reports. One of the outputs from this award is established SOPs for preparing single cell suspensions of HGSOC tumors which we can share with other HGSOC investigators.

Throughout the term of this award our data analysis continued with the development of new algorithms revealing new insights about HGSOC heterogeneity such as previously unrecognized tumor and immune cells types as well as correlations between tumor cells and immune cells providing insight as to how HG-SOV tumor cells subvert the host immune system. It is readily apparent that the depth of data generated by CyTOF requires significant data mining and is revealing unrecognized and revolutionary insights into the disease. Several key results have great potential to benefit patients. One paper “Commonly occurring cell subsets in high grade serous

ovarian tumors identified by single-cell mass cytometry" is in revision at Cancer cell and is attached to this report in the Appendix. Several other manuscripts are in preparation and this will be noted when the data is described below.

C.2 Results

Assay performance

As mentioned repeatedly in our annual progress awards we emphasized the production of reproducible and high quality data and especially the rigorous control of pre-analytical variables in the handling of primary tumor samples. Much of this information has been converted into SOPs and is included in our paper in the Appendix. A brief summary is however below. Given the potential of our data to be developed into clinical tests our focus on highly reproducible data is essential. In brief, this was demonstrated from: a) multiple replicates across fluorometric and mass cytometry platforms b) technical and biological replicates from two mass cytometry runs separated by a period of weeks. ***Our close attention to pre-analytical variables and the processing steps of tumor specimens is as much to do with respect for every HGSOC patient that has consented to provide their samples as well as to the generation of high quality data needed to translate our findings to the clinic.***

Summary of key findings in manuscript ***(Gonzalez et al. Commonly occurring cell subsets in high grade serous ovarian tumors identified by single-cell mass cytometry Cell Reports 2018 22(7):1875-1888).***

We performed a comprehensive single-cell phenotypic characterization of high-grade serous ovarian cancer (HGSOC) tumors by mass cytometry to determine relationships between the presumed diverse cell subsets generated within different samples, in concert with known patient outcomes. Unsupervised computational analysis revealed HGSOC tumor cell phenotypes that were less diverse than would have been predicted from the broad sets of genotypes reported in other studies. Amongst previously unrecognized cell subsets, each sample harboured a dominant cell (DC) subset as well as varying frequencies of cell subsets that co-expressed E-cadherin and vimentin (EV). Notably, tumors from patients with a poorer outcome had an increased frequency of cells co-expressing vimentin, HE4 and cMyc and populated more cell niches as quantified by Simpson's Diversity Index. That ovarian cancer shows reproducible cellular hierarchies suggests that programmed phenotypic behaviour dominates the mutational landscape offering a new focus for therapeutic development and monitoring the disease.

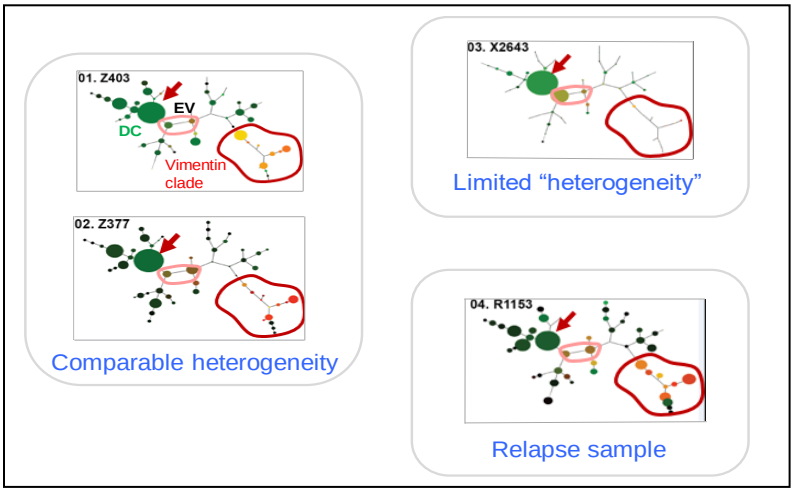

Figure 1: Cell types recur across samples: Heterogeneity can be defined by frequency of different cell types across samples with examples shown.

Relationships between tumor cell types

Given that our CyTOF data analysis allowed us to identify new cell subsets that were also present across multiple tumors, we wanted to gain a greater understanding of their relationships to one another and the features a cell needs for metastatic conversion. Therefore, we performed a network analysis to identify changes in correlations between specific cell types in non-relapse versus relapse samples [20-22]. For this analysis, pairwise Spearman correlation coefficients were

calculated between the following parameters for all samples: i) cell frequency for the 56 X-shift clusters, ii)

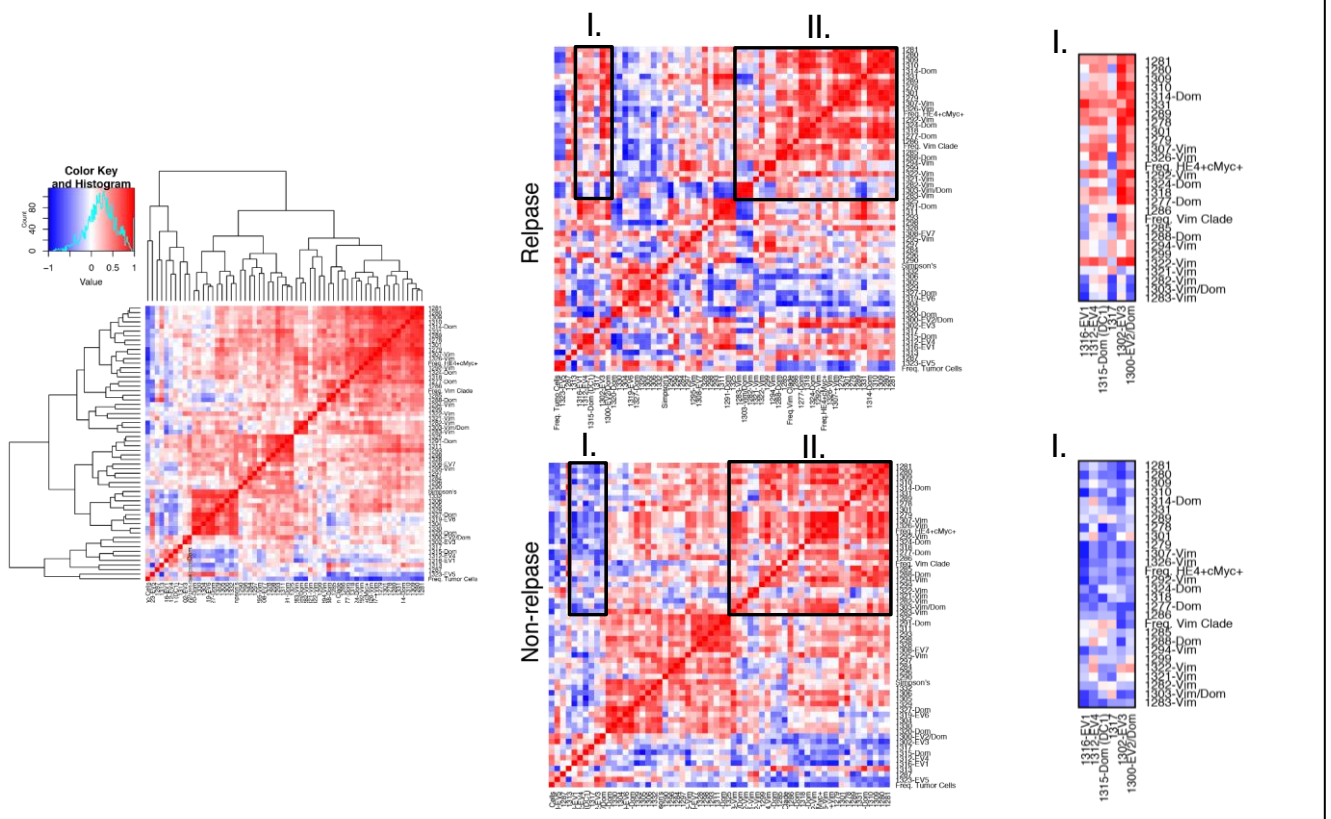

Figure 2: Pairwise correlations of cluster frequencies in non-relapse and relapse samples. Pairwise correlations and clustering were performed to generate a "parent" heat-map with the features detailed in the text. Based on the clustering in the parent heat-map, row order was imposed in the two subsequent correlation heat-maps shown for non-relapse (lower panels) and relapse samples (upper panels). The two black outlines demarcate modules, picked out visually that differ (I) or remain comparable (II) between non-relapse and relapse samples. Scale shows Spearman correlation coefficient.

frequency of cells in the vimentin clade, iii) frequency of manually gated HE4/cMyc cells, iv) total tumor cell frequency and v) the Simpson's diversity index. Strikingly, although many features between the tumor cells were interspersed in the non-relapse and relapse matrices, coordinated modules were evident (Figure 2, Modules I and II). Specifically, in module 1, correlations were predominantly negative for non-relapse samples (Figure 2, lower panel) whereas those same correlations were predominantly positive for the relapse samples (Figure 2, upper panel). Module 1 was notable in that it incorporated EV clusters 1 to 4 and DC1 and their correlations with: i) cells in the vimentin clade ii) HE4/cMyc cells, iii) vimentin-expressing cell clusters, iv) E-cadherin cell clusters and v) four DC clusters. Together these data suggest that in non-relapse samples, a constraint could be in place that precludes a trajectory to a metastatic phenotype whereas in the relapse samples a coordinated intra-tumoral change has overcome this constraint. In contrast to module I, any differences in module II between non-relapse and relapse samples were subtle and revealed overall positive correlations within and between the E-cadherin and vimentin tumor compartments. The absence of any EV clusters in module II was notable lending further support of a role for these clusters in the trajectory to a metastatic phenotype.

It necessarily follows that the relationships we defined between the tumor cell types are greatly influenced by the host immune system. Strikingly, we when we computed the relative size of the immune compartment (cells that were CD45+) with those of the tumor compartment (cells that were CD45- CD31- FAP-) we saw reciprocity

between the two compartments. This result is interesting since the tumor also includes stromal cells. However, most striking of all *the ratio of the tumor and immune compartments greatly differed between individual tumor samples* **(Figure 4).** Recently, several groups have shown that ovarian tumors are often infiltrated by activated T cells at the time of diagnosis, and patients with dense infiltrates of CD3+CD8+ T cells experience unexpectedly favorable progression-free and overall survival. Other cell types in the immune infiltrate oppose anti-tumor immunity, including CD4+CD25+FoxP3+ regulatory T cells, CD8+ regulatory T cells, macrophages, and dendritic cells. The composition of immune infiltrates is shaped by the expression of cytokines, chemokines, antigens, major histocompatibility complex molecules, and costimulatory molecules[23]. Understanding how this balance between a pro-tumor immune response versus a tumor immune suppressive response could be translated into predicting patients that would benefit the most from immune-therapeutic agents is a key issue for HGSOC patients. This is particularly relevant since response rates to immune check-point inhibitor therapy have been disappointing with objective response rates ranging from 5.9% to 15% in early phase Ib-II trials, including patients with platinum-resistant ovarian cancer[24]. As we investigated the tumor immune infiltrate in our HGSOC tumors the differing relative ratios between the tumor and immune infiltrating cells **(Figure 4)** could provide an important parameter to take into account when personalizing immune-therapy for HGSOC patients.

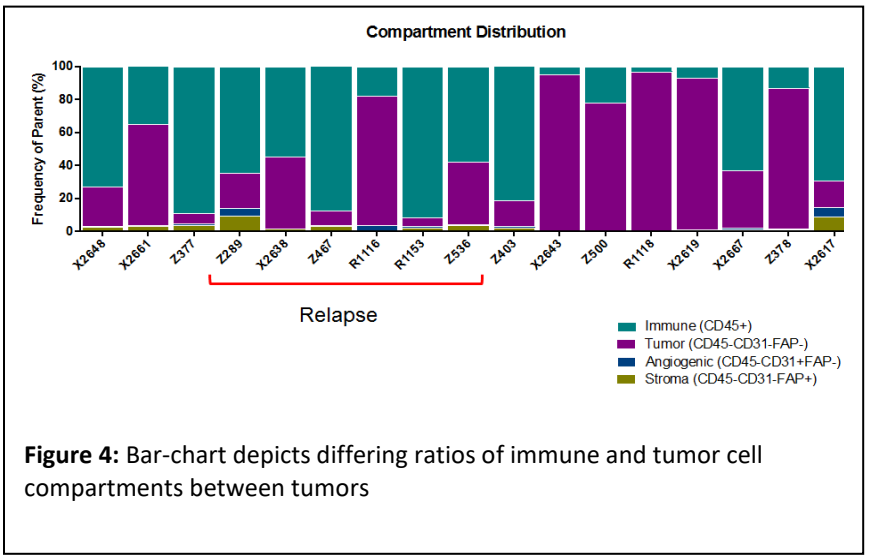

Figure 4: Bar-chart depicts differing ratios of immune and tumor cell compartments between tumors

Overall, our approach for understanding any disease is to take a systems-level view given that it very unlikely that one parameter alone could be a biomarker for determining disease prognosis, and/or guiding choice of therapy. Therefore, we set out to analyze our data in-depth in order to provide a greater understanding of the tumor-immune system and to identify a set of mechanistic biomarkers that could be translated to the clinic. We first determined whether any patterns emerged for manually gated anchor immune cell subsets (e.g. B-cell, T-cells, monocytes) that could be related to the relative ratios of the tumor to immune cells. As can be seen **(Figure 5)** no such relationships could be discerned. However, there were a significant amount of unaccounted immune cells thereby prompting an unsupervised analysis of the tumor-immune cells.

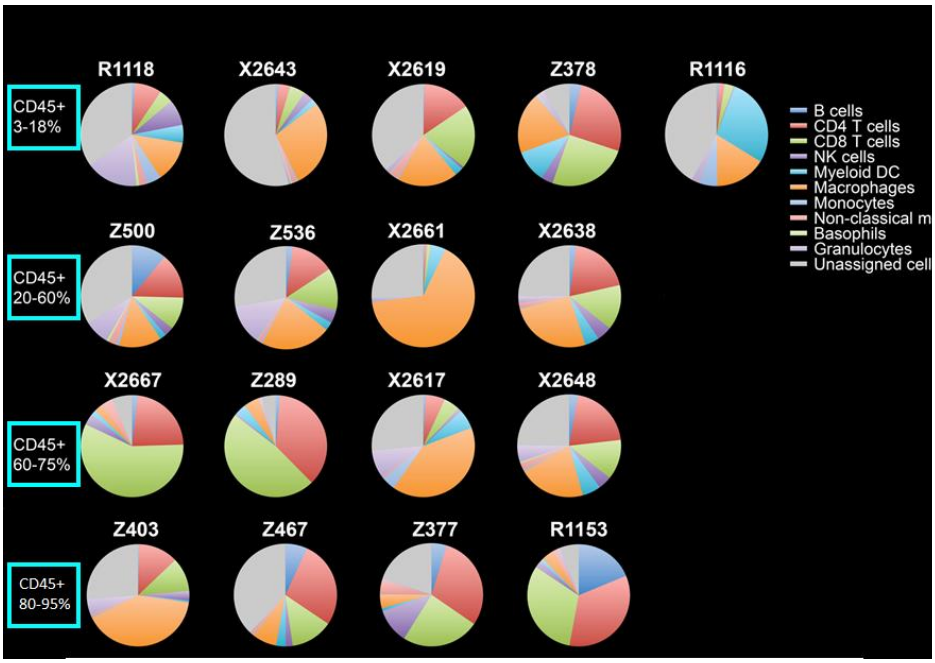

Figure 5: Pie-charts depict relative frequencies of manually-gated immune cell subsets in each sample. Pie-charts are organized by the relative size of the CD45+ immune cells. The grey "slices" show non-anchor unassigned immune cell types.

In our unsupervised analysis we performed an extensive correlation analysis to determine whether certain cell types changed IN CONCERT with other cell types. In other words if the frequency of one of the novel tumor cell types (e.g vimentin/HE4/cMyc) we discovered rose did anther immune cell type rise or fall in a correlated manner. Pairwise Spearman correlation were performed between all tumor and immune cell types with each other and then hierarchically clustered to denote “cassettes” of changes where groups of cell types were changing as modules. The results are shown in **Figure 6**.

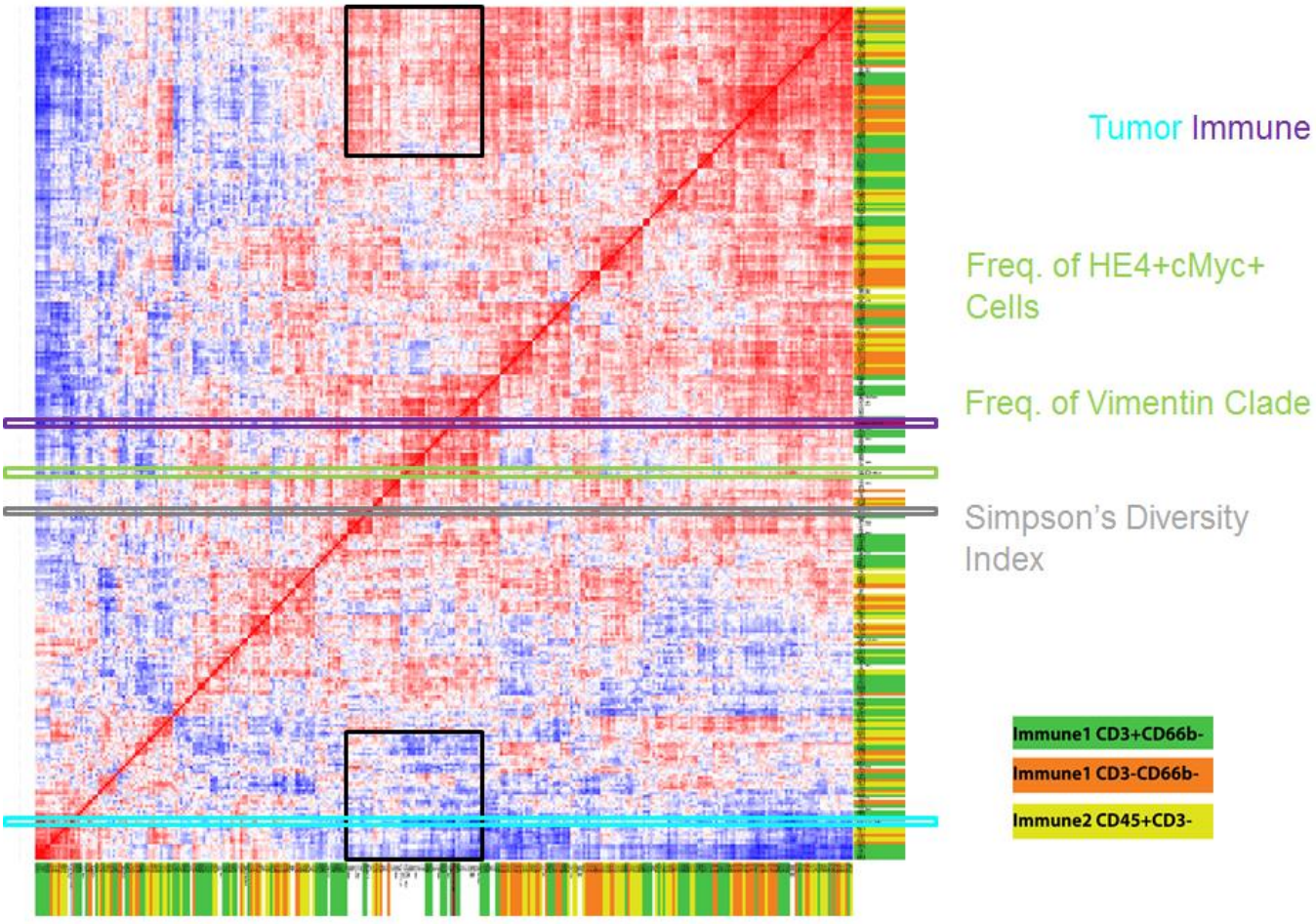

Figure 6:

Given our Kaplan-Meier data showing that poor-prognosis patients have an increased frequency of vimentin/HE4/cMyc cells (see manuscript in Appendix) we reasoned that this must necessarily be correlated with changes to the host immune system. Indeed, correlation analysis between vimentin/HE4/Myc cells revealed a positive correlation between these tumor cells with the CD45+ immune compartment (Spearman corr. r = 0.7). Given that CyTOF analysis can delineate specific cell-types, our subsequent analysis was to reveal which specific immune cell subsets correlated with the vimentin/cHE4/Myc tumor cells. We found the highest correlations to be with two M2 macrophage cell subsets, r = 0.614 and r = -0.608. This is of great relevance given that infiltrating myeloid cells, including

macrophages are potent regulators of tumor-associated immune suppression, cell invasion, and metastases, and targeting of these innate immune cells may be the key to developing new immunotherapies[25]. The understanding of the role that myeloid/macrophage cells play in human cancer comes from evidence provided by retrospective cohort studies employing IHC where myeloid cells are identified by the expression of one or at most two markers, most commonly CD68 or CD163. This has led to a significant body of work demonstrating that the presence of tumor-associated macrophage (TAM) infiltrates correlate with poor patient prognosis. This is true across a variety of tumor types including breast, bladder, and ovarian cancer[26,27] . Yet in other studies, a high degree of macrophage infiltration has been associated with improved patient outcome[28] .

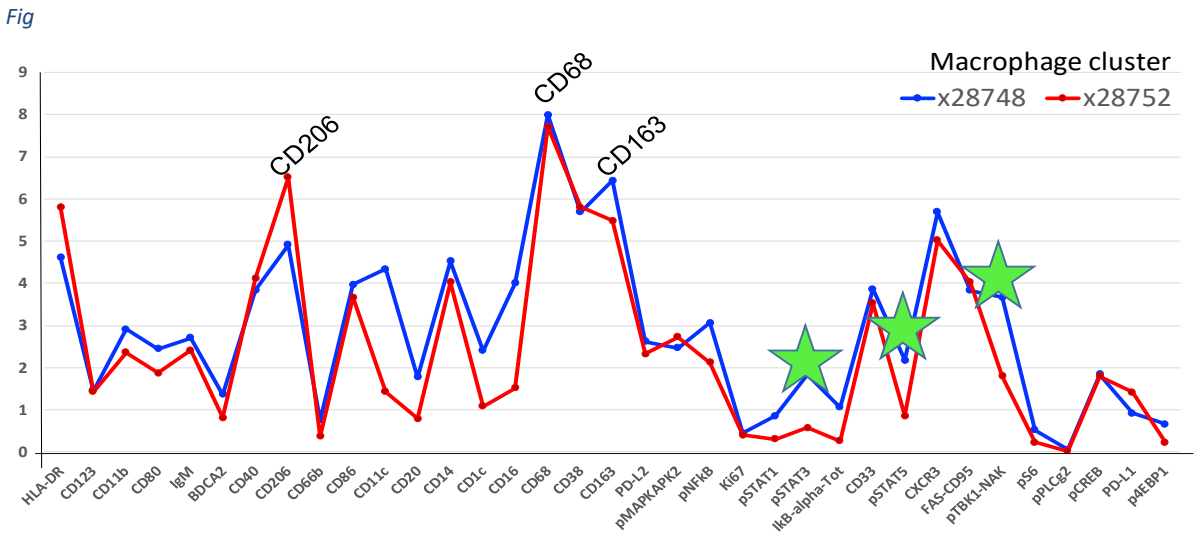

Figure 7: Protein expression of two macrophage clusters x28752 and x28748 that correlate positively and negatively respectively with vimentin/HE4/cMyc tumor cells. Red graph shows the positively correlated macrophage cell type and the blue shows the negatively correlated macrophage cell type. Macrophage markers are shown and the green stars depict signaling differences between the two macrophage cell subsets.

The differentially correlated macrophage cell types are consistent with the confusion in the literature. However, CyTOF has enabled us to identify distinguishing feature which lie in the activation states of intracellular signaling pathways. Thus, the negatively correlated macrophage cell subset has activated intracellular pSTAT3, pSTAT5 and pTBK/NfKb. This suggests that in these macrophages intracellular signaling of specific pathways may be important for reducing metastasis if indeed vimentin/HE4/cMyc cells are surrogates of this biological process.

We also observed other immune cell types that correlated positively with the tumor cell frequency; M2 macrophages, granulocytes, decidual-like NK cells, CD8 T cells. We are developing algorithms to integrate these features and provide a metric that could reprsent the overall activation state of the tumor immune infiltrate within individual HGSOC tumors.

DNA damage and PARP inhibitors

Until recently our knowledge of a genetic contribution to ovarian cancer focused almost exclusively on mutations in the *BRCA1/2* genes. However, through germline and tumor sequencing an understanding of the larger phenomenon of homologous recombination deficiency (HRD) has emerged. HRD impairs normal DNA damage repair which results in loss or duplication of chromosomal regions, termed genomic loss of heterozygosity (LOH)[29-31]. The list of inherited mutations associated with ovarian cancer continues to grow with the literature currently suggesting that up to one in four cases will have germline mutations, the majority of which result in

HRD. Furthermore, an additional 5-7% of ovarian cancer cases will have somatic HRD.

DNA damage and its repair or lack thereof are central to the induction of mutations, which drive the development of nearly all cancers. Healthy cells defend themselves against the deleterious effects of DNA damage through an interrelated series of molecular pathways, the DNA damage response (DDR), that recognize DNA damage, stall the cell cycle, and mediate DNA repair, thus maintaining the integrity of the genome. Key to the DDR are the poly(ADP-ribose) polymerase 1 and 2 (PARP1 and PARP2) enzymes, DNA damage sensors and signal transducers that operate by synthesizing negatively charged, branched poly(ADP-ribose) (PAR) chains (PARylation) on target proteins as a form of posttranslational modification

An understanding of the functions of PARP1 and PARP2 in the DDR drove long-standing efforts to develop small-molecule PARP1/2 inhibitors (PARPi). The original rationale was that PARPi could sensitize tumor cells to conventional treatments that cause DNA damage, including multiple chemotherapy or radiotherapy approaches, which remain the backbone of treatment for most cancer patients. By inhibiting PARP-mediated repair of DNA lesions created by chemo- or radiotherapy, greater potency might be achieved. About 30 years ago, small-molecule nicotinamide analogs were shown to inhibit PARylation and to enhance the cytotoxicity of dimethyl sulfate, a DNA damaging agent. Subsequent drug discovery efforts led to the development of clinical PARPi, including veliparib (Abbvie), rucaparib (Pfizer/Clovis), olaparib (KuDOS/AstraZeneca), and niraparib (Merck/Tesaro). More recently, a second generation, more potent PARPi, talazoparib (Lead/Biomarin/Medivation/Pfizer) has also been developed. These PARPi all interact with the binding site of the PARP enzyme cofactor, β nicotinamide adenine dinucleotide (β-NAD^+), in the catalytic domain of PARP1 and PARP2 but, have differing effects in terms of their cytotoxic potency and ability to “trap” PARP1 on DNA.

When cells become HRR deficient, whether driven by defects in BRCA1, BRCA2, or other pathway components, non-conservative forms of DNA repair predominate, such as non-homologous end joining (NHEJ). These processes either fuse broken DNA ends at the DSBs without using a homologous DNA sequence to guide repair or fuse regions of DNA close to the site of the DSB that exhibit short regions of DNA sequence homology, deleting the intervening DNA sequence. The preferential use of these non-conservative repair mechanisms in the absence of HRR therefore may lead to DNA alterations, including deletions of genetic material. Some of the mutations that arise in this way may foster cancer initiation or progression, potentially explaining at least in part why mutations in *BRCA1* and *BRCA2* increase cancer risk; additional roles of BRCA1 and BRCA2 in processes such as chromatin remodeling and transcriptional regulation may also be relevant to pathogenesis

Patients with germline or somatic HRD are candidates for targeted therapies to poly (ADP-ribose) polymerase (PARP) inhibitors, and, as a result, establishing an infrastructure for widespread HRD testing is imperative. Although genetic testing of defects in HRD genes is now becoming the norm, it is ultimately protein function that is a truer reflection of how the disease, in this case HGSOC is responding to targeted therapy and the emergence of resistance. For this reason we built a DNA damage/cell cycle CyTOF antibody panel

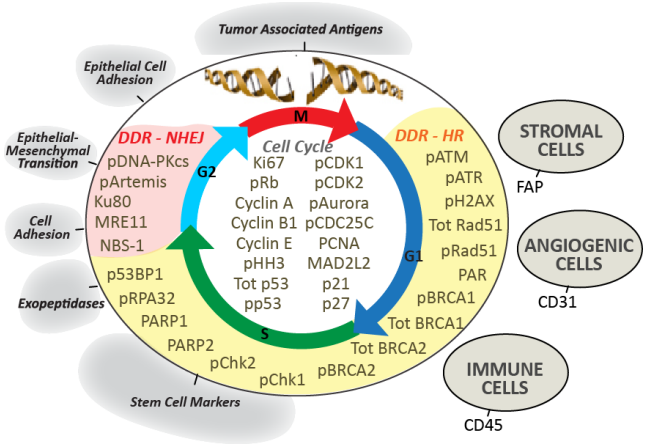

Figure 8: CyTOF antibody panel focused on the cell cycle and two types of repair mechanisms for DNA double strand breaks; homologous recombination (HR) and non-homologous end joining (NHEJ)[1,2]. The panel will also include antibodies we used against surface markers to define tumor cell type.

to generate a systems-level view of the DDR.

Our study used a panel of high grade serous ovarian cell lines shown molecularly and genetically to resemble HGSOC tumors based on their comparison with primary tumors analyzed genetically and molecularly by the TCGA[3]. We phenotyped the HGSOC cell lines using the same CyTOF antibody panel that we used for

Conditions/Experiment Duration:		
None		
IR	5Gy, rest for 30min	dsDNA breaks
UVC	100J/m2, rest for 90min	UVC causes predominantly DNA damage to cells in the form of pyrimidine dimers and 6-4 photoproducts. These DNA lesions halt RNA polymerase II elongation and are repaired enzymatically by two types of nucleotide excision repair (NER)
Nocodazole	100ng/ml, 18hrs	Nocodazole is an antineoplastic agent which exerts its effect in cells by interfering with the polymerization of microtubules. Microtubules are one type of fibre which constitutes the cytoskeleton, and the dynamic microtubule network has several important roles in the cell, including vesicular transport, forming the mitotic spindle and in cytokinesis. Cells treated with nocodazole arrest with a G2- or M-phase DNA content
Etoposide	10uM, 24hrs	Etoposide forms a ternary complex with DNA and the topoisomerase II enzyme (which aids in DNA unwinding), prevents re-ligation of the DNA strands, and by doing so causes DNA strands to break (dsDNA break)
Olaparib	1.2uM, 72hrs	Olaparib is a PARP inhibitor, inhibiting poly ADP ribose polymerase (PARP), an enzyme involved in DNA repair. Enhanced cell death in cells with ssDNA break, leading to dsDNA breaks.
Talazoparib	10nM, 72hrs	Talazoparib is a PARP inhibitor, inhibiting poly ADP ribose polymerase (PARP), an enzyme involved in DNA repair. Enhanced cell death in cells with ssDNA break, leading to dsDNA breaks.

Table 1: DNA-damage inducing agents used in our experiments.

characterizing newly diagnosed HGSOC tumors and showed that an individual cell line recapitulated individual proteomic features of the primary tumor (**Figures 9 and 10**).

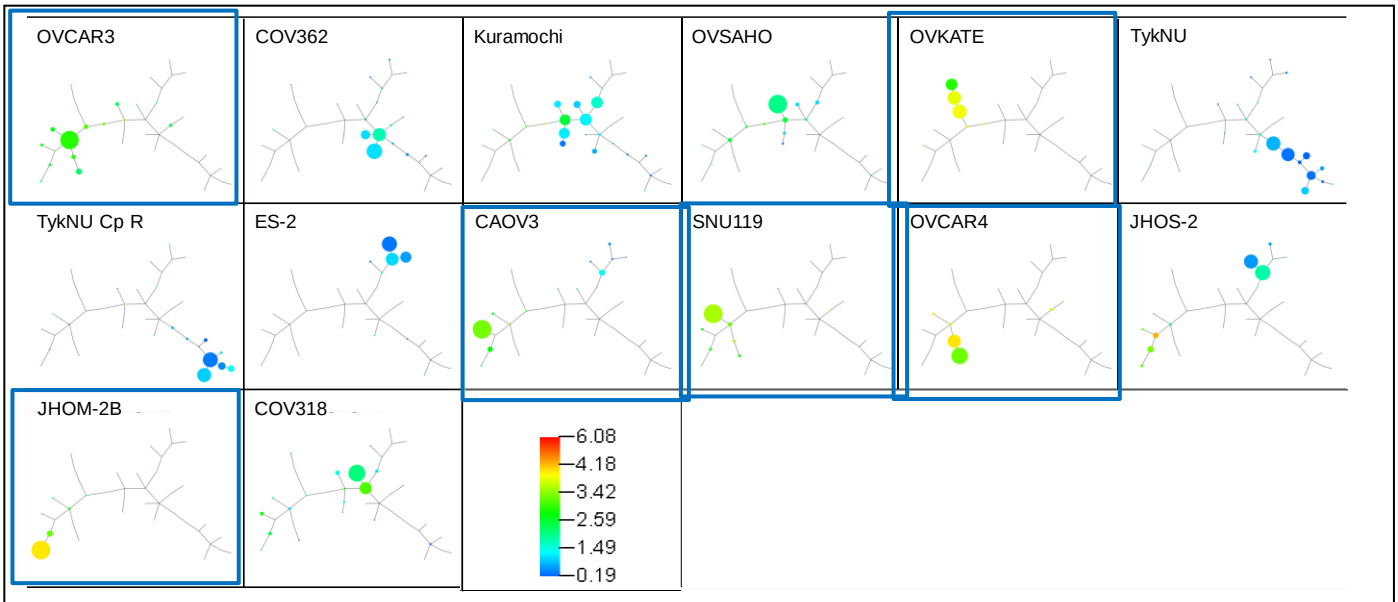

Figure 9: **E-cadherin** expression levels in HG-SOC cell lines. For details of the analysis see our manuscript in revision in the Appendix. Square blue boundaries call out cell lines with high E-cadherin expression levels and epithelial tumor characteristics (data not shown).

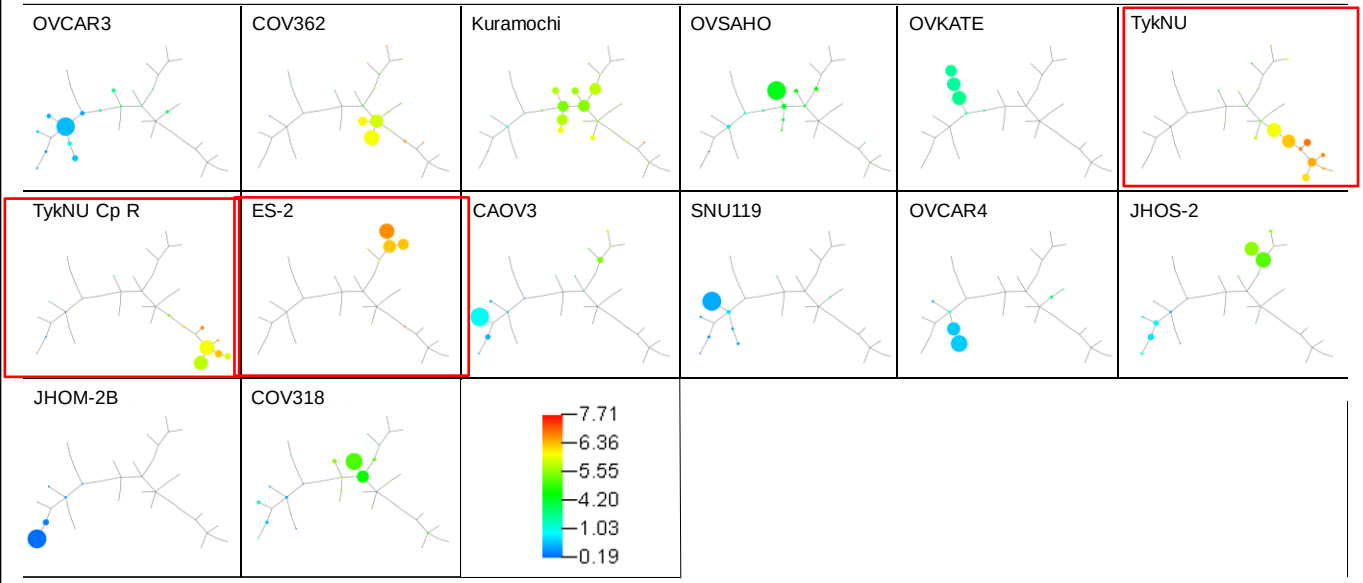

Figure 10: Vimentin expression levels in HGSOC cell lines[3]. For details of the analysis see our manuscript Gonzalez et al in in the Appendix. Square red boundaries call out cell lines with high vimentin expression levels and mesenchymal (metastatic) tumor characteristics (data not shown).

We then selected HGSOC cell lines and interrogated their systems-level response to DNA damage when exposed to the agents shown in **Table 1**. The analysis was based on measuring the DNA damage response for each phase of the cell cycle. The rationale for this is based on the known intricate coordination between DNA repair and cell cycle progression. In response to unrepaired DNA damage checkpoints are activated that arrest cell cycle progression at critical stages before or during DNA replication and before cell division (G2/M checkpoint). Under normal physiological conditions, this system is designed to prevent duplication and segregation of damaged DNA. Our detailed analysis is ongoing as part of a manuscript in preparation. Here we select some examples to show the power of multi-parameter single cell analysis in revealing the response of HGSOC cell lines. The differences seen, particularly for an epithelial versus mesenchymal phenotype cells have potential to make a contribution to the mechanistic understanding of PARP inhibitors as it pertains to understanding adverse events and resistance in HGSOC patients.

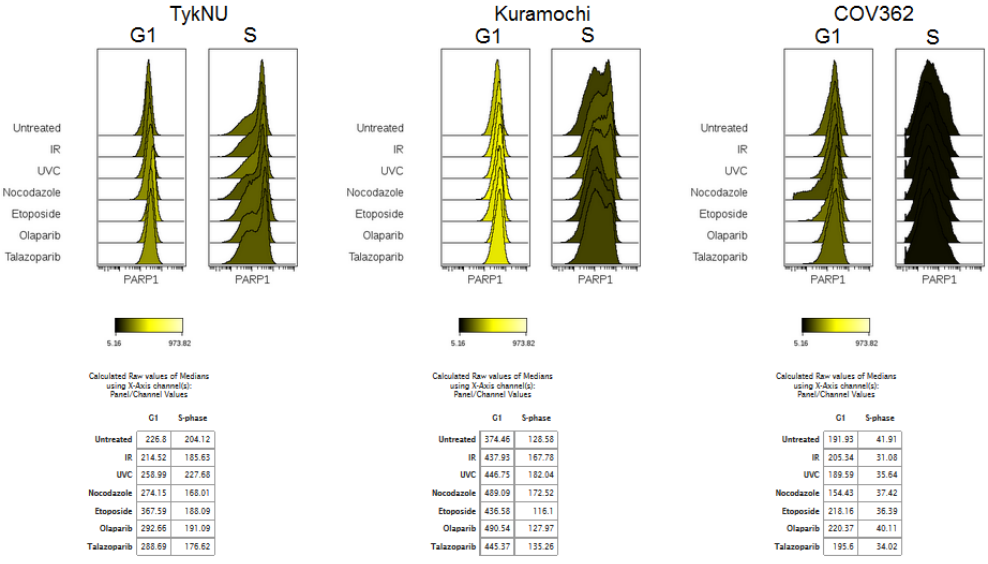

Figure 11: HGSOC cell lines exposed to the agents shown were analyzed using the CyTOF antibody panel shown in Figure 8. Histograms depict levels of **PARP1** protein in G1 and S.

Measurement of PARP1 expression levels reveal differences between cell lines and G1 and S-phases within an HGSOC cell line. Specifically, PARP1 levels are lower in S-phase and we

are investigating how this impacts cellular response to the PARPis olaparib and talazoparib.

As part of DDR work we also developed a single cell assay to measure protein-protein interactions. The numerous protein complexes makes this a perfect model system to measure such interactions simultaneously with their occurrence in the cell cycle. This work led to a publication: Burns TJ, Frei AP, Gherardini PF, Bava FA, Batchelder JE, Yoshiyasu Y, Yu JM, Groziak AR, Kimmey SC, Gonzalez VD, Fantl WJ, Nolan GP. High-throughput precision measurement of subcellular localization in single cells. *Cytometry A*. 2017 Feb;91(2):180-189. PMID: 28094900 (See Appendix).

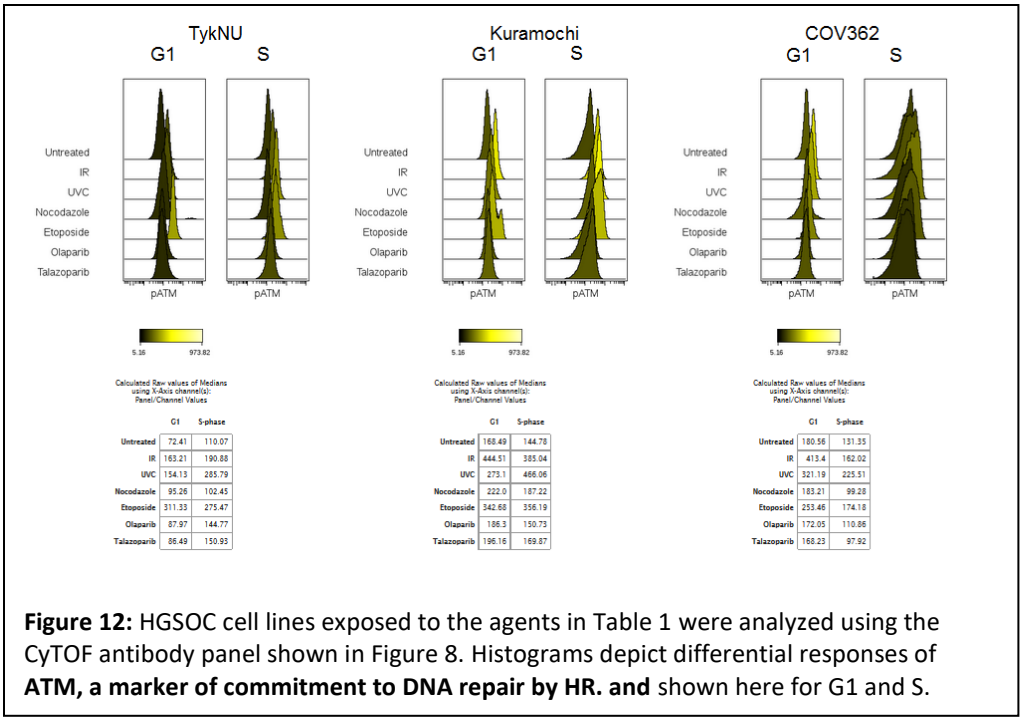

Figure 12: HGSOC cell lines exposed to the agents in Table 1 were analyzed using the CyTOF antibody panel shown in Figure 8. Histograms depict differential responses of **ATM, a marker of commitment to DNA repair by HR. and** shown here for G1 and S.

The data presented in Figures 12 and 13 depict differential phosphorylation/activation responses of ataxia telangiectasia mutated (ATM) and DNA –protein kinase catalytic subunit (DNA-PKcs) to the DNA damaging agents shown in Table 1. Focusing on the agents that induce double-stranded DNA breaks (*ionizing radiation and etoposide* (Table 1)) we note that the activation state of ATM is greatest in response to these two agents. This is consistent with its participation in DNA double-strand break repair by homologous recombination (HR) in which a protein complex termed MRN recruits ATM to the site of double strand DNA breaks and activates its kinase activity[2]. By contrast, DNA-PK is critically involved with a separate DNA double-strand break repair mechanism termed non-homologous end-joining (NHEJ). HR occurs exclusively in S and G2 of the cell cycle whereas NHEJ occurs throughout the cell cycle. Our continued analysis of the HGSOC cells and their response to genotoxic agents will reveal features that have clinical relevance for the administration of PARPis to HGSOC patients.

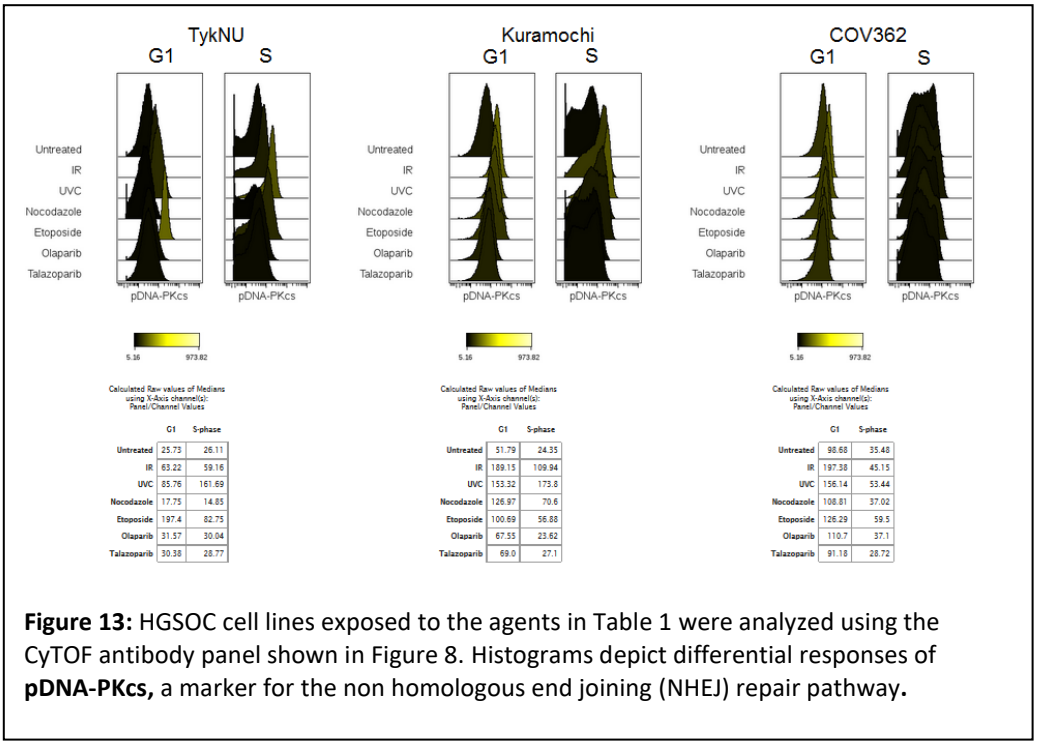

Figure 13: HGSOC cell lines exposed to the agents in Table 1 were analyzed using the CyTOF antibody panel shown in Figure 8. Histograms depict differential responses of **pDNA-PKcs,** a marker for the non homologous end joining (NHEJ) repair pathway**.**

D. KEY RESEARCH ACCOMPLISHMENTS

Publications

- **Gonzalez VD, Samusik N, Chen TJ, Savig ES, Aghaeepour N, Quigley DA, Huang Y-W, Giangarrà V, Borowsky AD, Hubbard NE, Chen S-Y, Han G, Ashworth , Kipps TJ Berek JS, Nolan GP. & Fantl WJ. Commonly occurring cell subsets in high grade serous ovarian tumors identified by single-cell mass cytometry. Cell Reports 2018. Feb 13 (22):1-14. Issue highlight and press release https://scopeblog.stanford.edu/2018/02/20/in-study-stanford-researchers-analyze-ovarian-cancer-cells-at-unprecedented-level-of-specificity/**

- **Burns TJ, Frei AP, Gherardini PF, Bava FA, Batchelder JE, Yoshiyasu Y, Yu JM, Groziak AR, Kimmey SC, Gonzalez VD, Fantl WJ, Nolan GP. High-throughput precision measurement of subcellular localization in single cells. *Cytometry A*. 2017 Feb;91(2):180-189. PMID: 28094900.**

Scientific findings

- Demonstrated that tumor heterogeneity characterized by CyTOF is far more limited than would be expected from the genetics.
- Identified three new tumor cell subsets with potential therapeutic and prognostic benefit.
- One cell subset that co-expresses vimentin, HE4 and cMyc pre-exists in diagnostic samples and correlates with relapse.
- Partner (Pierian, Frankville, Tennessee) identified to develop a test to quantify the frequency of these cells in newly diagnosed tumors
- More diversity within a tumor is associated with worse outcomes as quantified by Simpson's index of diversity.
- Combined our new computational tools with standard statistics; both descriptive and inferential as well as multiple hypothesis testing techniques to analyze the data.
- New correlation analyses identified new relationships between tumor and immune cell subsets.
- Specifically a decidual-like (d) NK cell subset is *positively correlated* with tumor cell abundance.
- Two macrophage cell types identified that are positively and negatively (respectively) correlated with vimentin/HE4/cMyc cells
- An exhausted T-cell subset is *anti-correlated* with tumor cell abundance
- The apparent immune tolerance conferred upon tumor cells by NK cells may be mediated by IL-35, thereby identifying a very new and novel target for HGSOC tumors

E. REPORTABLE OUTCOMES

E.1 Publications supported by this funding

1. Good, Z, Sarno,J, Jager, A Samusik, N, Aghaeepour, N, Simonds, EF, White, L Lacayo, N, Fantl, WJ, Fazio, G, Gaipa, G. Biondi, A. Tibshirani, R, Bendall, SC, Nolan. GP & Kara L Davis. Single-cell developmental classification of B cell precursor acute lymphoblastic leukemia at diagnosis reveals predictors of relapse. Nature medicine 2018 Mar 5. doi: 10.1038/nm.4505. [Epub ahead of print].

2. Gonzalez VD, Samusik N, Chen TJ, Savig ES, Aghaeepour N, Quigley DA, Huang YW, Giangarrà V, Borowsky AD, Hubbard NE, Chen SY, Han G, Ashworth A, Kipps TJ, Berek JS, Nolan GP, Fantl WJ. Commonly Occurring Cell Subsets in High-Grade Serous Ovarian Tumors Identified by Single-Cell Mass Cytometry. Cell Reports 2018 Feb 13;22(7):1875-1888.

3. Han G, Chen SY, Gonzalez VD, Zunder ER, Fantl WJ, **Nolan GP**. Atomic mass tag of bismuth-209 for increasing the immunoassay multiplexing capacity of mass cytometry. Cytometry A. 2017 Dec;91(12):1150-1163.

4. Dodd D, Spitzer MH, Van Treuren W, Merrill BD, Hryckowian AJ, Higginbottom SK, Le A, Cowan TM, **Nolan GP**, Fischbach MA, Sonnenburg JL. A gut bacterial pathway metabolizes aromatic amino acids into nine circulating metabolites. Nature. 2017 Nov 30;551(7682):648-652.

5. Kleppe M, Spitzer MH, Li S, Hill CE, Dong L, Papalexi E, De Groote S, Bowman RL, Keller M, Koppikar P, Rapaport FT, Teruya-Feldstein J, Gandara J, Mason CE, **Nolan GP**, Levine RL. Jak1 Integrates Cytokine Sensing to Regulate Hematopoietic Stem Cell Function and Stress Hematopoiesis. Cell Stem Cell. 2017 Oct 5;21(4):489-501.

6. Aghaeepour N, Ganio EA, Mcilwain D, Tsai AS, Tingle M, Van Gassen S, Gaudilliere DK, Baca Q, McNeil L, Okada R, Ghaemi MS, Furman D, Wong RJ, Winn VD, Druzin ML, El-Sayed YY, Quaintance C, Gibbs R, Darmstadt GL, Shaw GM, Stevenson DK, Tibshirani R, **Nolan GP**, Lewis DB, Angst MS, Gaudilliere B. An immune clock of human pregnancy. Sci Immunol. 2017 Sep 1;2(15).

7. Aghaeepour N, Kin C, Ganio EA, Jensen KP, Gaudilliere DK, Tingle M, Tsai A, Lancero HL, Choisy B, McNeil LS, Okada R, Shelton AA, **Nolan GP**, Angst MS, Gaudilliere BL. Deep Immune Profiling of an Arginine-Enriched Nutritional Intervention in Patients Undergoing Surgery. J Immunol. 2017 Aug 9. pii: ji1700421.

8. Mukherjee S, Jensen H, Stewart W, Stewart D, Ray WC, Chen SY, **Nolan GP**, Lanier LL, Das J. In silico modeling identifies CD45 as a regulator of IL-2 synergy in the NKG2D-mediated activation of immature human NK cells. Sci Signal. 2017 Jun 27;10(485).

9) O'Gorman WE, Kong DS, Balboni IM, Rudra P, Bolen CR, Ghosh D, Davis MM, **Nolan GP**, Hsieh EW. Mass cytometry identifies a distinct monocyte cytokine signature shared by clinically heterogeneous pediatric SLE patients. J Autoimmun. 2017 Apr 4.

10) Jensen H, Chen SY, Folkersen L, **Nolan GP**, Lanier LL. EBI3 regulates the NK cell response to mouse cytomegalovirus infection. Proc Natl Acad Sci U S A. 2017 Feb 14;114(7):1625-1630.

11) Spitzer MH, Carmi Y, Reticker-Flynn NE, Kwek SS, Madhireddy D, Martins MM, Gherardini PF, Prestwood TR, Chabon J, Bendall SC, Fong L, **Nolan GP**, Engleman EG. Systemic Immunity Is Required for Effective Cancer Immunotherapy. Cell. 2017 Jan 26;168(3):487-502.

11) Alcántara-Hernández M, Leylek R, Wagar LE, Engleman EG, Keler T, Marinkovich MP, Davis MM, **Nolan GP**, Idoyaga J. High-Dimensional Phenotypic Mapping of Human Dendritic Cells Reveals Interindividual Variation and Tissue Specialization. Immunity. 2017 Dec 19;47(6):1037-1050.e6. doi: 10.1016/j.immuni.2017.11.001. Epub 2017 Dec 5

12) Saito T, Miyagawa K, Chen SY, Tamosiuniene R, Wang L, Sharpe O, Samayoa E, Harada D, Moonen JAJ, Cao A, Chen PI, Hennigs JK, Gu M, Li CG, Leib RD, Li D, Adams CM, Del Rosario PA, Bill M, Haddad F, Montoya JG, Robinson WH, Fantl WJ, **Nolan GP**, Zamanian RT, Nicolls MR, Chiu CY, Ariza ME, Rabinovitch M. Upregulation of Human Endogenous Retrovirus-K Is Linked to Immunity and Inflammation in Pulmonary Arterial Hypertension. Circulation. 2017 Nov 14;136(20):1920-1935.

13) Vadstrup K, Galsgaard ED, Jensen H, Lanier LL, Ryan JC, Chen SY, Nolan GP, Vester-Andersen MK, Pedersen JS, Gerwien J, Jensen T, Bendtsen F. NKG2D ligand expression in Crohn's disease and NKG2D-dependent stimulation of $CD8^+$ T cell migration. Exp Mol Pathol. 2017 Aug;103(1):56-70.

14) Porpiglia E, Samusik N, Van Ho AT, Cosgrove BD, Mai T, Davis KL, Jager A, **Nolan GP**, Bendall SC, Fantl WJ, Blau HM. High-resolution myogenic lineage mapping by single-cell mass cytometry. Nat Cell Biol. 2017 May;19(5):558-567.

15) Savino AM, Sarno J, Trentin L, Vieri M, Fazio G, Bardini M, Bugarin C, Fossati G, Davis KL, Gaipa G, Izraeli S, Meyer LH, **Nolan GP**, Biondi A, Te Kronnie G, Palmi C, Cazzaniga G. The histone deacetylase inhibitor givinostat (ITF2357) exhibits potent anti-tumor activity against CRLF2-rearranged BCP-ALL.

E.2 Presentation
Nolan

EarthRise at IONS 09/2016 Petaluma, CA. *The Illusion of Heterogeneity in Cancer*

Stanford Immunology Scientific Conference 09/2016 Stanford, CA. *Organizing the Cancer/Immune System Heterogeneity Illusion with Deep Phenotypic Profiling.*

Amgen 09/16 San Francisco, CA. *Bringing Order to the Heterogeneity Illusion in Cancer.*

Animal Model Development Workshop 09/2016 Bethesda, MA. *Organizing the Diversity in Blood and Tissue via High Parameter Analysis.*

Medimmune 09/2016 Mountain View, CA. *The Illusion of Heterogeneity in Cancer*

Nature Conference 09/2016 Seattle, WA. *Single cell deep profiling of cancer and immunity.*

Cell Symposia 10/16 Berkley, CA. *A Defined "Structure" for the Immune System That Reflects Immune Surveillance & Mechanistic Processes.*

Human Cells 10/16 London, England. *A Defined "Structure" for the Immune System That Reflects Immune Surveillance & Mechanistic Processes.*

AACR 10/16 Boston, MA. *The Illusion of Heterogeneity in Cancer*

University of Pennsylvania, 10/16 Philadelphia, PA. *A Defined "Structure" for the Immune System That Reflects Immune Surveillance & Mechanistic Processes.*

Parker Institute Retreat 10/16 Middleburg, VA. Organizing the Cancer/Immune System Heterogeneity Illusion with Deep Phenotypic Profiling

UCSF Pathology Department 11/16 San Francisco, CA. Organizing the Cancer/Immune System Heterogeneity Illusion with Deep Phenotypic Profiling

17th Annual PI Meeting 12/16 Bethesda, MD. *A Defined "Structure" for the Immune System That Reflects Immune Surveillance & Mechanistic Processes.*

Genome Sciences Seminar UW 01/17 Seattle, WA. *The Heterogeneity Illusion: High Parameter Imaging of Cancer & Immunity.*

Mass Spectrometry: Applications to the Clinical Laboratory 01/17 Palm Springs, CA. *A Defined "Structure" for the Immune System That Reflects Immune Surveillance & Mechanistic Processes.*

Advances in Genome Biology and Technology – AGBT 02/17 Ft. Lauderdale, FL. *Sequencers as Flow Cytometers: Ultra-High Throughput Single Cell Analysis of Proteins and RNAs by Split-pool Synthesis.*

Immune Mediated Inflammatory Diseases 02/17 Wellcome, London, England. *Human immune response monitoring / Deep Immune Phenotyping.*

La Jolla Institute for Allergy and Immunology 03/17 La Jolla, CA. *A Defined "Structure" for Immune Systems that Reflects Immune Surveillance & Mechanistic Processes.*

Wayne State School of Medicine 03/17 Detroit, MI. A Defined "Structure" for Immune Systems that Reflects Immune Surveillance & Mechanistic Processes

Keystone 03/17 Vancouver, BC. A *Defined "Structure" for Immune Systems that Reflects Immune Surveillance & Mechanistic Processes.*

Association of Bimolecular Recourse Facilities – ABRF 03/17 San Diego, CA. *A Defined "Structure" for Immune Systems that Reflects Immune Surveillance & Mechanistic Processes.*

AACR Annual meeting 04/17 Washington, DC. *A Defined "Structure" for Immune Systems that Reflects Immune Surveillance & Mechanistic Processes.*

ISB Symposium 04/17 Seattle, WA. *A Defined "Structure" for Immune Systems that Reflects Immune Surveillance & Mechanistic Processes.*

UT Southwestern 04/17 Dallas, TX. *A Defined "Structure" for Immune Systems that Reflects Immune Surveillance & Mechanistic Processes.*

MD Anderson 04/17 Houston, TX. *A Defined "Structure" for Immune Systems that Reflects Immune Surveillance & Mechanistic Processes.*

PICI Institute 04/17 Santa Barbara, CA. *A Defined "Structure" for Immune Systems that Reflects Immune Surveillance & Mechanistic Processes.*

RNA Seq 2017 04/17 San Francisco, CA. *A Defined "Structure" for Immune Systems that Reflects Immune Surveillance & Mechanistic Processes.*

National Jewish Health, 05/17 Denver, CO. *A Defined "Structure" for Immune Systems that Reflects Immune Surveillance & Mechanistic Processes.*

Memorial Sloan Kettering 05/17 New York, NY. A Defined "Structure" for Immune Systems that Reflects Immune Surveillance & Mechanistic Processes

ASGCT 20th Annual meeting 05/17 Washington, DC. *A Defined "Structure" for Immune Systems that Reflects Immune Surveillance & Mechanistic Processes.*

Filovirus workshop 05/17 Rockville, MD. *A Defined "Structure" for Immune Systems that Reflects Immune Surveillance & Mechanistic Processes.*

Keystone 2017 05/17 Stockholm, Sweden. *A Defined "Structure" for Immune Systems that Reflects Immune Surveillance & Mechanistic Processes*

FOCIS 2017 06/17 Chicago, IL. A Defined "Structure" for Immune Systems that Reflects Immune Surveillance & Mechanistic Processes

Pezcoller Symposium 06/17. Trento, IT. *A Defined "Structure" for Immune Systems that Reflects Immune Surveillance & Mechanistic Processes.*

FDA Science Board 06/17 Silver Spring, MD. *A Defined "Structure" for Immune Systems that Reflects Immune Surveillance & Mechanistic Processes.*

FASEB 07/17 Snowmass Village, CO. *A Defined "Structure" for Immune Systems that Reflects Immune Surveillance & Mechanistic Processes.*

Fantl

Aduro Biotech, Emeryville, October 19th, 2016. *Organizing the Heterogeneity of Ovarian Cancer Will Accelerate Patient Benefit.*

Baxter Lab retreat, Quadrus, Stanford University, January 31st, 2017. *Understanding the Vulnerabilities of Ovarian Cancer by High Dimensional Single-Cell Profiling.*

Faculty speaker Stanford Center for Cancer Systems Biology, March 1st, 2017. *Unravelling the Heterogeneity of Ovarian Cancer: An Approach Toward Accelerating Patient benefit.*

Speaker, ObGyn Basic and Translational Science Retreat, Stanford Faculty Club, May 20th 2017. *Understanding the Vulnerabilities of Ovarian Cancer by high dimensional Single Cell Profiling.*

Cambridge Healthcare Institute, Immuno-Oncology Summit, Boston, August 29th 2017. *Immunotherapy for Ovarian Cancer: One Cell at a Time.*

Plexxicon Inc, Berkeley. September 21st 2017. *Characterizing Ovarian Cancer One Cell at a Time.*

Topics and Techniques in Cancer Immunotherapy, PICI sponsored symposium, Stanford, October 9th 2017. *Immunotherapy for Ovarian Cancer: One Cell at a Time.*

BRCA Collaborators' meeting, Dana Farber, Boston. October 16th 2017. *Characterization of Ovarian cancer One Cell at a Time.*

E.3 Inventions, patents and licenses

Non-provisional patent application:
"Methods of prognosis and diagnosis of ovarian cancer". US 15/275,043.
Inventors: Berek, Fantl. Gonzalez, Nolan, Samusik.

Invention disclosure:
Title: **A method to identify the most beneficial poly- ADP-ribose-polymerase inhibitor for cancer patients**
Submitted: 03/15/16 by Fantl, Wendy
About the Invention
Purpose:
To develop a blood test for cancer patients that will guide the selection of a PARPi maximizing efficacy while minimizing unwanted side-effects.

F. OTHER ACHIEVEMENTS

OC ambassadorship duties

Numerous seminars as above to national and international audiences.
As a member of the UCSF Center for BRCA Research W. Fantl attended several fundraising events for BRCA research as well as several (three) meetings with members of the BRCA Centre spanning UCSF, Dana-Farber and Stanford.

Interaction with the OC community

Participation in GCIG and COGi conferences in Lisbon November 2016 (WF/J. Berek).
Fundraising events for ovarian cancer research (Under One Umbrella fund raiser Stanford held every November) by J. Berek.

Your mentoring progress

Continue to mentor graduate students and post-docs in my lab (about 25) and at other institutions (GPN).
Committee member for six thesis committees (GPN).
Student mentor for three graduate students and four post-docs at Stanford (WF). One of the graduate students now applying technology he developed to our OC studies. Three post-docs are working on OC under guidance of WF and also clinical input from JB.
Graduate student mentor and pre-major advisor for eight Stanford undergraduates with interest in natural sciences and medicine (WF).
Ellen Weaver mentorship award to WF from the Bay Area Women in Science organization. Acceptance speech was focused around WF's work in ovarian cancer.

Your mentee's progress

During the past year, four of my post-docs received faculty positions (GPN).

Three graduate students graduated (GPN).
Mentoring rotation- graduate student working on ovarian cancer as one part of thesis (WF).
One undergraduate did a summer internship with WF focused on ovarian cancer. She continues to work in our lab during her school year demonstrating excellent planning and enthusiasm for the OC program.

G. CONCLUSIONS

OVERARCHING CONCLUSIONS FORM THIS FUNDING

- Established SOPs that are extensible to other solid tumors
  - Pre-analytical variables for tissue handling
  - Reagent validation and optimization
  - Understanding which data analysis tools to use

- Can we identify a "poor-prognosis" cell phenotype (comparable to vimentin/Myc/HE4 cells) in newly diagnosed kidney, bladder, prostate, other malignancies?
- Can we identify transitional EMT cells in other epithelial malignancies?

- With a new multi-parameter imaging technology CODEX, developed by the Nolan Lab (Goltsev et al Bioarchive 2017) can we characterize interplay between tumor cells & micro-environment by CODEX and CyTOF

Other conclusions

- See tumor diversity between samples, but within *a limited phenotypic hierarchy:*
  - For both surface markers and signaling molecules
  - See mutually exclusive expression of E-cadherin and vimentin in "epithelial" and "mesenchymal" compartments
  - See cells in transitional EMT that also co-express stem cell markers confirming what has been proposed in the literature.
  - Stem cell markers scattered throughout compartments: are there many ways to be a stem cell? Functional analysis can help answer this.
  - Great diversity in size of immune compartment across samples
  - We reproduce correlations between a tumor cell type with immune compartment size and immune cell type with tumor compartment size.
  - We reproduced the finding that the relative size of tumor and immune compartments anti-correlated.
  - We reproduce the finding that NK cell subsets are positively correlated with tumor compartment size and increase the likelihood that those NK cells could be decidual-like.
  - Highly regulated communication between immune and tumor compartments.
  - New level of detail regarding the immune compartment revealed by multi-parametric single cell mass cytometry.
  - We reproduced many aspects of the data from the two pilot studies which strongly validates our experiments at the technical level allowing us to makes inferences about HGSOC biology.
  - The information is foundational for following up with larger sample cohorts with the potential to inform treatments particularly immune-therapies for HGSOC.

H. REFERENCES

1 Ciccia, A. & Elledge, S. J. The DNA damage response: making it safe to play with knives. *Mol Cell* **40**, 179-204, doi:10.1016/j.molcel.2010.09.019 (2010).

2 Polo, S. E. & Jackson, S. P. Dynamics of DNA damage response proteins at DNA breaks: a focus on protein modifications. *Genes Dev* **25**, 409-433, doi:10.1101/gad.2021311 (2011).

3 Domcke, S., Sinha, R., Levine, D. A., Sander, C. & Schultz, N. Evaluating cell lines as tumour models by comparison of genomic profiles. *Nature communications* **4**, 2126, doi:10.1038/ncomms3126 (2013).

4 Bowtell, D. D. *et al.* Rethinking ovarian cancer II: reducing mortality from high-grade serous ovarian cancer. *Nat Rev Cancer* **15**, 668-679, doi:10.1038/nrc4019 (2015).

5 Matulonis, U. A. *et al.* Ovarian cancer. *Nat Rev Dis Primers* **2**, 16061, doi:10.1038/nrdp.2016.61 (2016).

6 Konecny, G. E. *et al.* Prognostic and therapeutic relevance of molecular subtypes in high-grade serous ovarian cancer. *J Natl Cancer Inst* **106**, doi:10.1093/jnci/dju249 (2014).

7 Krzystyniak, J., Ceppi, L., Dizon, D. S. & Birrer, M. J. Epithelial ovarian cancer: the molecular genetics of epithelial ovarian cancer. *Ann Oncol* **27 Suppl 1**, i4-i10, doi:10.1093/annonc/mdw083 (2016).
8 Tothill, R. W. *et al.* Novel molecular subtypes of serous and endometrioid ovarian cancer linked to clinical outcome. *Clin Cancer Res* **14**, 5198-5208, doi:10.1158/1078-0432.CCR-08-0196 (2008).
9 Integrated genomic analyses of ovarian carcinoma. *Nature* **474**, 609-615, doi:10.1038/nature10166 (2011).
10 Vogelstein, B. *et al.* Cancer genome landscapes. *Science* **339**, 1546-1558, doi:10.1126/science.1235122 (2013).
11 Bendall, S. C. & Nolan, G. P. From single cells to deep phenotypes in cancer. *Nature biotechnology* **30**, 639-647, doi:10.1038/nbt.2283 (2012).
12 Bendall, S. C., Nolan, G. P., Roederer, M. & Chattopadhyay, P. K. A deep profiler's guide to cytometry. *Trends in immunology* **33**, 323-332, doi:10.1016/j.it.2012.02.010 (2012).
13 Bendall, S. C. *et al.* Single-cell mass cytometry of differential immune and drug responses across a human hematopoietic continuum. *Science* **332**, 687-696, doi:10.1126/science.1198704 (2011).
14 Bjornson, Z. B., Nolan, G. P. & Fantl, W. J. Single-cell mass cytometry for analysis of immune system functional states. *Curr Opin Immunol* **25**, 484-494, doi:10.1016/j.coi.2013.07.004 (2013).
15 Spitzer, M. H. & Nolan, G. P. Mass Cytometry: Single Cells, Many Features. *Cell* **165**, 780-791, doi:10.1016/j.cell.2016.04.019 (2016).
16 Tanner, S. D., Baranov, V. I., Ornatsky, O. I., Bandura, D. R. & George, T. C. An introduction to mass cytometry: fundamentals and applications. *Cancer immunology, immunotherapy : CII* **62**, 955-965, doi:10.1007/s00262-013-1416-8 (2013).
17 Bruggner, R. V., Bodenmiller, B., Dill, D. L., Tibshirani, R. J. & Nolan, G. P. Automated identification of stratifying signatures in cellular subpopulations. *Proc Natl Acad Sci U S A* **111**, E2770-2777, doi:10.1073/pnas.1408792111 (2014).
18 Samusik, N., Good, Z., Spitzer, M. H., Davis, K. L. & Nolan, G. P. Automated mapping of phenotype space with single-cell data. *Nat Methods*, doi:10.1038/nmeth.3863 (2016).
19 Krishnaswamy, S. *et al.* Conditional density-based analysis of T cell signaling in single-cell data. *Science*, doi:10.1126/science.1250689 (2014).
20 Ideker, T. & Krogan, N. J. Differential network biology. *Molecular systems biology* **8**, 565, doi:10.1038/msb.2011.99 (2012).
21 Hotson, A. N. *et al.* Coordinate actions of innate immune responses oppose those of the adaptive immune system during Salmonella infection of mice. *Science signaling* **9**, ra4, doi:10.1126/scisignal.aaa9303 (2016).
22 Spitzer, M. H. *et al.* Systemic Immunity Is Required for Effective Cancer Immunotherapy. *Cell*, doi:10.1016/j.cell.2016.12.022 (2017).
23 Nelson, B. H. The impact of T-cell immunity on ovarian cancer outcomes. *Immunol Rev* **222**, 101-116, doi:10.1111/j.1600-065X.2008.00614.x (2008).
24 Gadducci, A. & Guerrieri, M. E. Immune Checkpoint Inhibitors in Gynecological Cancers: Update of Literature and Perspectives of Clinical Research. *Anticancer Res* **37**, 5955-5965, doi:10.21873/anticanres.12042 (2017).
25 Elliott, L. A., Doherty, G. A., Sheahan, K. & Ryan, E. J. Human Tumor-Infiltrating Myeloid Cells: Phenotypic and Functional Diversity. *Frontiers in immunology* **8**, 86, doi:10.3389/fimmu.2017.00086 (2017).
26 Obermajer, N., Muthuswamy, R., Odunsi, K., Edwards, R. P. & Kalinski, P. PGE(2)-induced CXCL12 production and CXCR4 expression controls the accumulation of human MDSCs in ovarian cancer environment. *Cancer Res* **71**, 7463-7470, doi:10.1158/0008-5472.CAN-11-2449 (2011).
27 Balermpas, P. *et al.* Head and neck cancer relapse after chemoradiotherapy correlates with CD163+ macrophages in primary tumour and CD11b+ myeloid cells in recurrences. *British journal of cancer* **111**, 1509-1518, doi:10.1038/bjc.2014.446 (2014).
28 Cunha, L. L. *et al.* Infiltration of a mixture of immune cells may be related to good prognosis in patients with differentiated thyroid carcinoma. *Clin Endocrinol (Oxf)* **77**, 918-925, doi:10.1111/j.1365-2265.2012.04482.x (2012).
29 Jackson, S. P. & Bartek, J. The DNA-damage response in human biology and disease. *Nature* **461**, 1071-1078, doi:10.1038/nature08467 (2009).
30 Ashworth, A. Drug resistance caused by reversion mutation. *Cancer Res* **68**, 10021-10023, doi:10.1158/0008-5472.CAN-08-2287 (2008).

31 Lord, C. J. & Ashworth, A. Mechanisms of resistance to therapies targeting BRCA-mutant cancers. *Nature medicine* **19**, 1381-1388, doi:10.1038/nm.3369 (2013).

APPENDIX

Resource

Cell Reports

Commonly Occurring Cell Subsets in High-Grade Serous Ovarian Tumors Identified by Single-Cell Mass Cytometry

Graphical Abstract

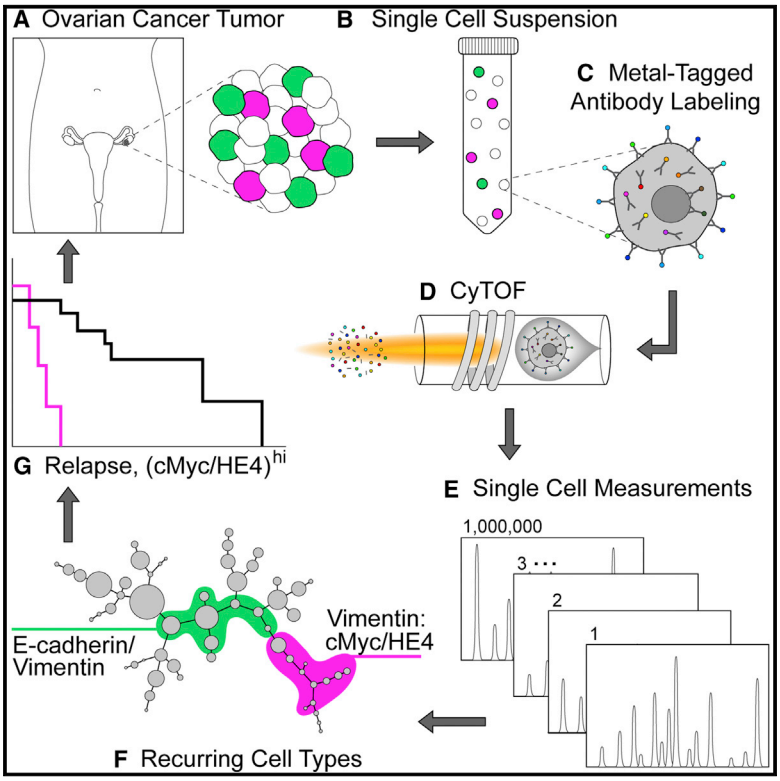

Highlights

- Cell types identified by CyTOF recur across newly diagnosed HGSOC tumors
- Greater frequency of vimentin/cMyc/HE4 cells correlates with poor prognosis
- A transitional EMT phenotype identified co-expressing E-cadherin and vimentin (EV)
- In relapse patients, EV cells are positively correlated with a metastatic trajectory

Authors

Veronica D. Gonzalez, Nikolay Samusik, Tiffany J. Chen, ..., Jonathan S. Berek, Garry P. Nolan, Wendy J. Fantl

Correspondence

wjfantl@stanford.edu

In Brief

Although genetic and proteomic data from bulk-processed HGSOC tumors exist, critical information about rare cell subsets is lost. Using multiparametric CyTOF analysis of viable single cells from HGSOC tumors, Gonzalez et al. uncover cell types recurring across tumors with potential roles in metastasis and disease progression.

Gonzalez et al., 2018, Cell Reports *22*, 1875–1888
February 13, 2018
https://doi.org/10.1016/j.celrep.2018.01.053

CellPress

Cell Reports
Resource

Commonly Occurring Cell Subsets in High-Grade Serous Ovarian Tumors Identified by Single-Cell Mass Cytometry

Veronica D. Gonzalez,[1,9] Nikolay Samusik,[1,9] Tiffany J. Chen,[1,10] Erica S. Savig,[1,11] Nima Aghaeepour,[1] David A. Quigley,[2,3] Ying-Wen Huang,[1] Valeria Giangarrà,[1] Alexander D. Borowsky,[4,5] Neil E. Hubbard,[4,5] Shih-Yu Chen,[1] Guojun Han,[1] Alan Ashworth,[2,6] Thomas J. Kipps,[7] Jonathan S. Berek,[8] Garry P. Nolan,[1] and Wendy J. Fantl[8,12,*]

[1]Baxter Laboratory for Stem Cell Biology, Department of Microbiology & Immunology, Stanford University School of Medicine, Stanford, CA 94305, USA
[2]Helen Diller Family Comprehensive Cancer Center, University of California, San Francisco, 1450 Third Street, San Francisco, CA 94158, USA
[3]Department of Epidemiology and Biostatistics, University of California, San Francisco, 1450 Third Street, San Francisco, CA 94158, USA
[4]Center for Comparative Medicine, University of California, Davis, Davis, CA 95616, USA
[5]Department of Pathology and Laboratory Medicine, Comprehensive Cancer Center, University of California, Davis School of Medicine, Sacramento, CA 95817, USA
[6]Department of Medicine, University of California, San Francisco, 1450 Third Street, San Francisco, CA 94158, USA
[7]Moores Cancer Center, University of California, San Diego, La Jolla, CA 92093, USA
[8]Stanford Comprehensive Cancer Institute and Department of Obstetrics and Gynecology, Stanford University School of Medicine, Stanford, CA 94305, USA
[9]These authors contributed equally
[10]Present address: Illumina, 5200 Illumina Way, San Diego, CA 92122, USA
[11]Present address: weLeap labs LLC, 8 Dover Street, San Carlos, CA 94070, USA
[12]Lead Contact
*Correspondence: wjfantl@stanford.edu
https://doi.org/10.1016/j.celrep.2018.01.053

SUMMARY

We have performed an in-depth single-cell phenotypic characterization of high-grade serous ovarian cancer (HGSOC) by multiparametric mass cytometry (CyTOF). Using a CyTOF antibody panel to interrogate features of HGSOC biology, combined with unsupervised computational analysis, we identified noteworthy cell types co-occurring across the tumors. In addition to a dominant cell subset, each tumor harbored rarer cell phenotypes. One such group co-expressed E-cadherin and vimentin (EV), suggesting their potential role in epithelial mesenchymal transition, which was substantiated by pairwise correlation analyses. Furthermore, tumors from patients with poorer outcome had an increased frequency of another rare cell type that co-expressed vimentin, HE4, and cMyc. These poorer-outcome tumors also populated more cell phenotypes, as quantified by Simpson's diversity index. Thus, despite the recognized genomic complexity of the disease, the specific cell phenotypes uncovered here offer a focus for therapeutic intervention and disease monitoring.

INTRODUCTION

High-grade serous ovarian cancer (HGSOC) is the most prevalent and lethal gynecological malignancy, characterized by TP53 mutations, inherited inactivating mutations in BRCA genes, defects in homologous recombination repair, and overall chromosomal instability (Bowtell et al., 2015; Ciriello et al., 2013; Matulonis et al., 2016). Using large-scale, high-throughput technologies, HGSOC primary tumors have also been characterized by RNA and miRNA expression signatures and promoter methylation status (Konecny et al., 2014; Krzystyniak et al., 2016; Cancer Genome Atlas Research Network, 2011; Tothill et al., 2008). Conclusions from these and other studies characterized HGSOC as a heterogeneous disease, with the term "heterogeneity" implying poor prognosis. Despite multiple studies linking molecularly based subtypes of HGSOC tumors to clinical outcomes, the findings have proved difficult to confirm in independent patient cohorts, partly because of the use of different algorithms (Chen et al., 2017; Konecny et al., 2014; Krzystyniak et al., 2016; Cancer Genome Atlas Research Network, 2011; Tothill et al., 2008; Wang et al., 2012). To date, however, aside from determining a patient's BRCA status, none of the molecular features reported have been incorporated into routine clinical practice for HGSOC patients.

Studies in cancer showed that genomic complexity converges upon a more limited set of phenotypes (Krogan et al., 2015; Vogelstein et al., 2013), implying that the well-recognized diversity of HGSOC may be more circumscribed at the proteomic level. In-depth proteomic analyses by mass spectrometry of HGSOC tumor cell lysates provided insight into how genetic and molecular changes affect the proteome of ovarian tumors (Coscia et al., 2016; Zhang et al., 2016). Although these datasets were linked to clinical outcomes, they only provide a valuable resource and await translation into clinical practice.

As an alternative proteomic approach, we applied multiparameter CyTOF to dissect HGSOC at the single-cell level, with the

goal of identifying clinically relevant cell subsets implicated in tumor development and drug resistance and with the potential to offer new therapeutic targets. CyTOF permits detailed characterization of subtly differing cell populations (large or small) that are lost within tumor cell lysates. With a panel of antibodies, each conjugated to a distinct stable metal isotope, CyTOF enables simultaneous detection of up to 50 parameters per cell (Bjornson et al., 2013; Spitzer and Nolan, 2016). Here, we present a detailed single-cell phenotypic characterization of more than 800,000 tumor cells dissociated from 17 newly diagnosed HGSOC tumors, simultaneously measuring expression of surface markers, intracellular signaling proteins, transcription factors, and cell-cycle proteins.

RESULTS

CyTOF Assay Optimization for Ovarian Tumors

Of 22 newly diagnosed ovarian tumors received (median follow-up post-surgery 26 months), 17 were confirmed as HGSOC and were the focus of this study (Table 1). Tumors were disaggregated using stringent protocols, generating more than 800,000 viable single-cells for analysis (Experimental Procedures). To evaluate the overall quality of the tumor tissue and any significant tumor necrosis, immunohistochemistry was performed on tissue sections that had been prepared within 30 min of tumor resection (Experimental Procedures; Figure S1; Table S1). Pathogenic mutations in TP53, a known molecular hallmark of HGSOC (Ahmed et al., 2010; Köbel et al., 2016) were confirmed by sequencing (Table S2).

Single-cell suspensions of HGSOC tumors were analyzed by CyTOF, which detects antibodies bound to cells via metal isotopes to which the antibodies are conjugated (Bjornson et al., 2013; Spitzer and Nolan, 2016). A panel of 41 antibodies was assembled that included 4 antibodies to allow for manual gating of viable tumor cells, with the remaining 37 (selected after an extensive review of the literature) used to interrogate HGSOC tumor biology (Figure 1; Experimental Procedures; Table S3) (Baldwin et al., 2014; Bowtell et al., 2015; Davidson et al., 2012; Lu et al., 2012; Matulonis et al., 2016; Stewart et al., 2011; Ye and Weinberg, 2015; Zhang et al., 2014). The final choice of antibodies relied upon the availability of high-quality antibody clones. Antibody performance and reproducibility of our methodology was demonstrated by analysis of CyTOF data from technical and biological replicates (Experimental Procedures; Figure S2).

Phenotypic Characterization of Ovarian Tumor Cell Subsets by Unsupervised Clustering

This study measured 37 proteins (surface and intracellular) simultaneously in more than 800,000 single cells to identify specific cell phenotypes and their recurrence across HGSOC tumors. Manual gating using CD45, FAP, and CD31 excluded immune, stromal, and blood vessel cells, respectively, from the analysis. An antibody against cleaved PARP (cPARP) was used to gate out non-viable tumor cells (Figure 1; Experimental Procedures; Figure S3). Initially, single-cell readouts for the tumor cells from all 17 samples were computationally merged without input of any biological or clinical features. These readouts were then clustered with a non-parametric, density-based algorithm called X-shift (Samusik et al., 2016). Markers for clustering were chosen to delineate cell identity, based on co-expression patterns for E-cadherin, CD73, CD61, CD90, CD151, CD49f, CD133, ROR1, CD10, CD13, endoglin, CD24, CD44, MUC16 (CA125), mesothelin, vimentin, and HE4. The 56 X-shift clusters generated by the X-shift algorithm were then visualized computationally along a minimum spanning tree (MST) such that neighboring clusters had similar marker co-expression patterns (Anchang et al., 2016; Samusik et al., 2016) (Figure S4). These MSTs enabled the visualization of a detailed substructure of component cell phenotypes within the tumors (Figures 2A and 2B).

Each composite MST representing the merged data of 800,000 cells is colored protein by protein (Figures 2A and 2B; Figure S5). Most cell clusters expressed E-cadherin, which was usually mutually exclusive of those expressing vimentin (Figure 2A). E-cadherin clusters co-expressed PAX8, CA125, and mesothelin, known tumor-associated antigens for HGSOC (Figure S5D) (Bowtell et al., 2015; Matulonis et al., 2016). However, expression patterns of putative stem cell markers differed throughout the MST, suggesting stem-progenitor plasticity and adaptation to the dynamic host microenvironment (Figure 2B) (McAllister and Weinberg, 2014).

Notably, seven cell clusters co-expressed E-cadherin and vimentin (EV), forming a bridge between the E-cadherin and vimentin branches of the MST and varying from low to high frequencies across individual tumors (Figure 2A; Table S6). Data support the link between transit through epithelial mesenchymal transition (EMT) and the acquisition of stem cell-like properties (Shibue and Weinberg, 2017; Ye and Weinberg, 2015). Consistent with this, EV cells expressed differing patterns of the putative cancer stem cell markers included in this study (CD24, CD13, CD10, CD73, CD61, CD49f, CD90, CD44, CD133, endoglin, and ROR1), as well as signaling proteins involved in conferring stemness (Sox-2, pSTAT3, pSTAT5, NFκB, pCREB, and β-catenin) (Ye and Weinberg, 2015). As described for E-cadherin and vimentin clusters, differing co-expression patterns for putative stem cell markers in EV cells are also consistent with cellular plasticity (Figures 2B and 2C; Figure S5; Table S4).

Further analysis of EV cell clusters revealed that expression levels of a subgroup of proteins mirrored either those in E-cadherin or vimentin clusters, emphasizing the hybrid properties of the EV cells (Figure 2C, upper plot with clustering markers and lower plot with intracellular markers). Of proteins expressed at increased levels in EV cells, compared to the E-cadherin or vimentin cells, five (CD24, CD49f, CD133, ROR, and β-catenin) are consistent with a stem cell phenotype (Davidson, 2016; Shibue and Weinberg, 2017; Stewart et al., 2011; Zhang et al., 2014), while three (pRb, cyclin B1, and pS6) are consistent with a dysregulated cell cycle as previously reported (Au-Yeung et al., 2017; Etemadmoghadam et al., 2010). Also observed in EV clusters were elevated levels of CD151, a metastasis-promoting protein implicated in ovarian cancer EMT (Baldwin et al., 2014; Hemler, 2014; Medrano et al., 2017).

Although detected in E-cadherin and EV clusters, HE4 and cMyc had significantly greater co-expression in the vimentin branch of the MST (Figure S5). HE4, an ovarian tumor-associated protein with a presumptive role in promoting invasion, metastasis,

Table 1. Clinical Characteristics of Patient Samples

Case No.	Patient ID	Age at Case Start (year)	Weight (kg)	BMI	Description	Localization	Histological Type	Stage	Radicality	Grade	Morphology	MUC16/CA-125 (U/mL)
1	X2617	63	79.0	29.0	malignant neoplasm of ovary	ovary	ovarian carcinoma, serous type	III C	R2	G3	serous cystadenocarcinoma, NOS	2,418.7
2	X2619	57	100.0	35.4	malignant neoplasm of ovary	ovary	ovarian carcinoma, serous type	IIC	R0	G2	serous cystadenocarcinoma, NOS	NA
3	Z289	79	65.0	25.4	malignant neoplasm of ovary	ovary	ovarian carcinoma, serous papillary type	III C	RX	G3	papillary serous cystadenocarcinoma	355.5
4	X2648[a]	67	78	27	malignant neoplasm of ovary	peritoneum	ovarian carcinoma, serous papillary type	III C	R1	G3	serous cystadenocarcinoma, NOS (C56.9)	461
5	Z378	71	77.0	26.6	malignant neoplasm of ovary	ovary	ovarian carcinoma, serous papillary type	III C	R0	G3	serous cystadenocarcinoma, NOS (C56.9)	44.4
6	X2643	53	77.0	24.3	malignant neoplasm of ovary	peritoneum	ovarian carcinoma, serous papillary type	III B	R0	G3	serous cystadenocarcinoma, NOS (C56.9)	614.2
7	Z403	82	71.0	27.1	malignant neoplasm of ovary	ovary	ovarian carcinoma	III C	RX	G3	serous surface papillary carcinoma (C56.9)	129.7
8	X2638	72	80.0	32.0	malignant neoplasm of ovary	ovary	adenocarcinoma	IV	R2	G3	adenocarcinoma, NOS	318
9	Z377[b]	56	108.0	35.7	malignant neoplasm of ovary	ovary	ovarian carcinoma, serous papillary type	IV	R0	G3	serous surface papillary carcinoma	541.5
10	Z467	48	72	24.3	malignant neoplasm of ovary	omentum	ovarian carcinoma, serous papillary type	III C	R0	G3	serous cystadenocarcinoma, NOS (C56.9)	135.1
11	R1116	67	72	27.4	malignant neoplasm of ovary	ovary	ovarian carcinoma, serous papillary type	III C	R1	G3	serous surface papillary carcinoma (C56.9)	481.6
12	R1118	84	53	19.2	malignant neoplasm of ovary	ovary	ovarian carcinoma, serous type	III A	RX	G3	serous cystadenocarcinoma, NOS (C56.9)	360.3
13	Z500	58	85	30.1	malignant neoplasm of ovary	ovary	ovarian carcinoma, serous papillary type	III C	R0	G3	serous surface papillary carcinoma (C56.9)	NA
14	X2661[a]	74	63	24.6	malignant neoplasm of ovary	peritoneum	ovarian carcinoma, serous papillary type	III C	R2	G3	serous surface papillary carcinoma (C56.9)	813.5
15	R1153	88	47	19.6	malignant neoplasm of ovary	ovary	ovarian carcinoma, serous papillary type	III C	R2	G3	papillary serous cystadenocarcinoma (C56.9)	90.4
16	Z536	82	56	19.8	malignant neoplasm of ovary	omentum	ovarian carcinoma, serous papillary type	III C	RX	G3	serous cystadenocarcinoma, NOS (C56.9)	1124
17	X2667	69	61	22.4	malignant neoplasm of ovary	ovary	ovarian carcinoma, serous papillary type	III C	R0	G3	serous surface papillary carcinoma (C56.9)	159.1

Chemo-naive tumors used in this study were all diagnosed as malignant neoplasms of the ovary. Most were late stage, and all patients underwent surgical debulking followed by a platinum-based chemotherapeutic regimen. See also Table S2.

[a]Clinical follow-up information was unavailable for patients X2648 and X2661.

[b]Patient Z377 died during surgery.

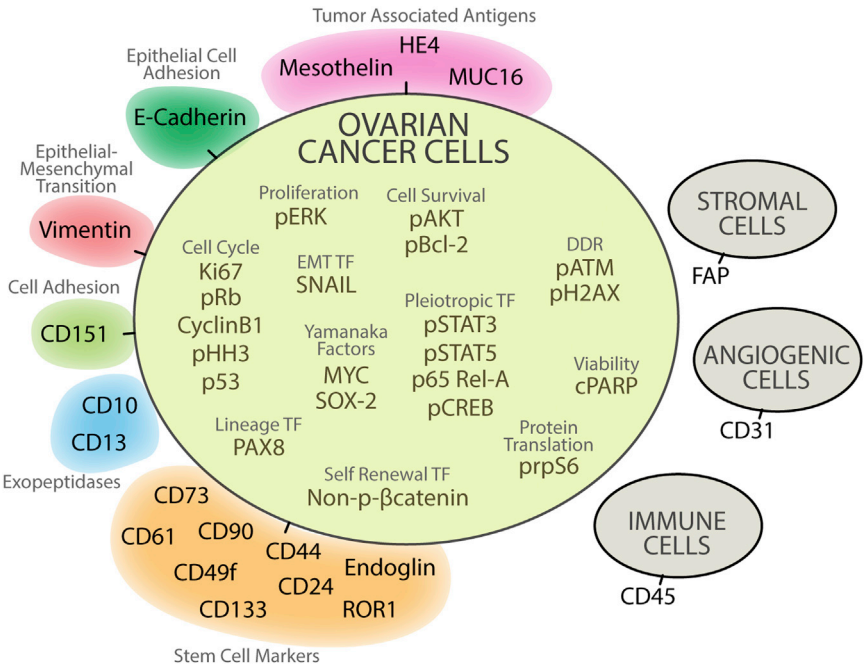

Figure 1. Antibody Panel for CyTOF

To detect proteins expressed by individual cells in ovarian tumor samples, 37 of 41 antibodies were selected. Colors indicate different categories of proteins. Because no prior cell sorting was undertaken before CyTOF, CD45, FAP, and CD31 were added to this panel to identify and subsequently exclude by manual gating, immune, angiogenic, and stromal cells. To select for viable cells, an antibody to cleaved PARP (cPARP) was also included in the panel (Experimental Procedures). See also Figure S3 and Table S3.

and drug resistance, is often used as a biomarker for the management of HGSOC (Li et al., 2017; Lu et al., 2012; Moore et al., 2014). MYC and WFDC2 (HE4) gene amplification in HGSOC is well documented (Jiang et al., 2013; Li et al., 2013; Lu et al., 2012; Cancer Genome Atlas Research Network, 2011), but co-expression of cMyc and HE4 with vimentin is revealed here and suggests a prominent role for these proteins in HGSOC metastasis.

Co-occurring Cell Subsets across Tumors

Reflecting the composite MST, MSTs for individual samples were enriched for cell clusters expressing E-cadherin, with differing expression patterns for individual proteins (Figure 2D; Figures S6 and S7). Both within and across the tumors, cluster sizes (denoting cell frequency) differed and defined the diversity of each tumor (Figure 2D; Tables S5 and S6).

Examination of the relative cell frequency distribution across all clusters revealed that each sample had a dominant cluster (DC) but that its relative cell frequency ranged from 16% to 83% (Figures 3A–3C; Tables S5 and S6). DC1 was present in all samples but was dominant in samples 1–6 (Figures 3B and 3C). DC2–DC10 were found across the remaining eleven samples. Of the ten DCs, seven resided within the E-cadherin part of the MST. DC4 and DC8 were within the EV and vimentin MST branches, respectively (Figures 2D and 3B). Comparing the phenotypic profiles across the DCs showed significant differences in the expression of clustering markers. This contrasts with the lower variability in the expression of the intracellular proteins and highlights their importance for tumor survival (Figure 3D).

Quantification of Heterogeneity by Simpson's Diversity Index

To determine whether the differences in cell frequency distribution across the 56 cell clusters (Figure 3A) were predictive of outcome, we performed a Simpson's diversity analysis, an algorithm used for determining the number of species and their abundance in eco-systems and applied to a CyTOF study of natural killer (NK) cells (Horowitz et al., 2013). A higher Simpson's diversity index, indicating greater tumor diversity, correlated with relapse within a year irrespective of whether vimentin-expressing cells were included ($p = 0.005$) or excluded ($p = 0.008$) from the computation (Figure 3D) and indicates that the diversity resides principally in the E-cadherin-expressing tumor cells.

Identification of Pre-existing Cell Subsets Associated with Relapse

After surgery, all HGSOC patients in this cohort were treated with a platinum-based therapeutic regimen. Within a year, six patients relapsed, but none of the DC or EV clusters correlated with this outcome (Figure 3A). However, tumor samples from relapse patients contained more vimentin-expressing cells (vimentin clade), consistent with poor prognosis ($p = 0.014$) (Figure S8). Furthermore, analysis of the vimentin clade uncovered a subpopulation of cells associated with relapse that co-expressed cMyc and HE4. This was corroborated by manual gating ($p = 0.01$) (Figures 4A and 4B). Kaplan-Meier analysis was performed to determine whether the pre-existing vimentin/cMyc/HE4 cells were linked to patient survival. Patients' tumors were divided into two groups based on the presence of vimentin/cMyc/HE4 cells above and below a 3% cell frequency threshold computed by k-means clustering. The plots showed that patients with tumors having a frequency of vimentin/HE4/cMyc cells > 3% were more likely to proceed to relapse after carboplatin treatment ($p = 0.002$, hazard ratio [HR] = 0.17) (Figure 4C).

Evaluating the Role of HE4 and cMyc in Carboplatin Resistance

To evaluate further a mechanistic role for carboplatin resistance in cells co-expressing vimentin, HE4, and cMyc, the TYK-nu HGSOC cell line was selected. It bore strictly mesenchymal traits, based on expression of vimentin and lack of detectable E-cadherin, and co-expressed high levels of cMyc and HE4. TYK-nu cells were cultured in the continuous presence of

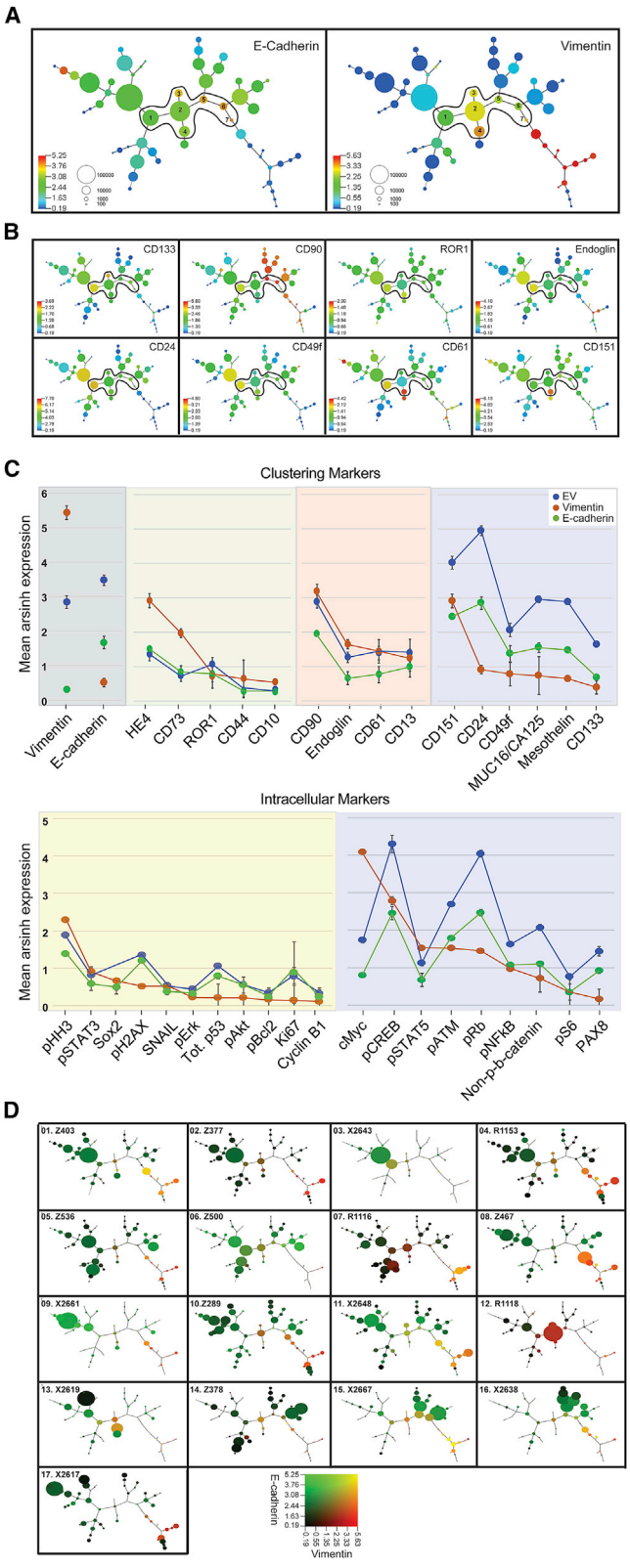

Figure 2. Mean Protein Expression Levels across 56 X-Shift Cell Clusters

(A) Composite MST of 17 HGSOC tumors shows mean expression of E-cadherin (E) (left-hand panel) and vimentin (V) (right-hand panel). Seven cell clusters co-expressing both E and V (EV clusters) are numbered and encircled. Scale shows cell frequency per bubble.

(B) Composite MST as in (A), showing expression levels of putative stem cell markers and CD151, a cell adhesion protein.

(C) Ranked mean protein expression levels with SEM shown for EV (blue), E-cadherin (green), and vimentin (orange) cell clusters (upper plot, clustering proteins; lower plot, intracellular proteins). Panels for the clustering markers show subgroups of EV proteins with expression levels that are comparable to E-cadherin (green background) or vimentin (orange background) or differ significantly from those in the E-cadherin or vimentin clusters. Panels for the intracellular markers show a subgroup of EV proteins with expression levels comparable to either E-cadherin or to both E-cadherin and vimentin (yellow background). The second subgroup of EV proteins have differing expression levels to both E-cadherin and vimentin (blue background).

(D) Cell distribution within the 56 clusters reveal different degrees of tumor diversity. Individual MSTs for each of the 17 tumor samples show co-expression of E-cadherin (green) and vimentin (red). Bubble sizes reflect the number of cells in each cluster ($\sqrt[3]{\textit{Absolute number of cells from all samples}}$). Scales represent median arsinh-transformed protein expression (Experimental Procedures). Blue (A and B) and black (D) represent a signal < 0.19 arcsinh-transformed and 1.0 in raw CyTOF counts. Range of expression > 0.19 up to the 99th percentile colored by quantile increases. See also Figures S5 and S6 and Tables S5 and S6.

carboplatin for 72 or 96 hr (Experimental Procedures). After CyTOF analysis and traditional flow cytometry gating, two main subpopulations of TYK-nu cells were revealed that co-expressed vimentin with either low (lo) cMyc^{lo}/HE4^{lo} or high (hi) cMyc^{hi}/HE4^{hi} (Figure 4D, blue and yellow gates, respectively). In the absence of carboplatin treatment, the mean frequency of cMyc^{lo}/HE4^{lo} cells was 27%, and it fell to 13% and 14% after continuous exposure to carboplatin for 72 and 96 hr, respectively. Concomitantly, levels of cPARP increased in this subpopulation from 0.5% in the absence of carboplatin to 12% and 14% at 72 and 96 hr continuous exposure, respectively, demonstrating a drug-responsive apoptotic trajectory in cMyc^{lo}/HE4^{lo} cells (Figure 4D). By contrast, the mean frequency of cMyc^{hi}/HE4^{hi} cells after carboplatin exposure did not change significantly (range of 42%–50% for untreated and treated). Their lack of drug responsiveness was further demonstrated by the low frequency of cells expressing cPARP (mean frequency of 0.33% with the absence of carboplatin to 2.5% and 7% at 72 and 96 hr continuous exposure, respectively). These data are consistent with our patient tumor data, in which the frequency of cells co-expressing vimentin with high levels of cMyc and HE4 is correlated with early relapse, presumably attributable to carboplatin resistance.

Correlation Analyses between HGSOC Clusters

Our unsupervised CyTOF data analysis allowed us to identify cell subsets that were present across multiple tumors. To gain a greater understanding of their relationships to one another and the changes a cell needs to undergo for metastatic conversion, we performed a network analysis to compare changes in correlations between specific cell types occurring in non-relapse and relapse samples (Hotson et al., 2016; Ideker and Krogan, 2012;

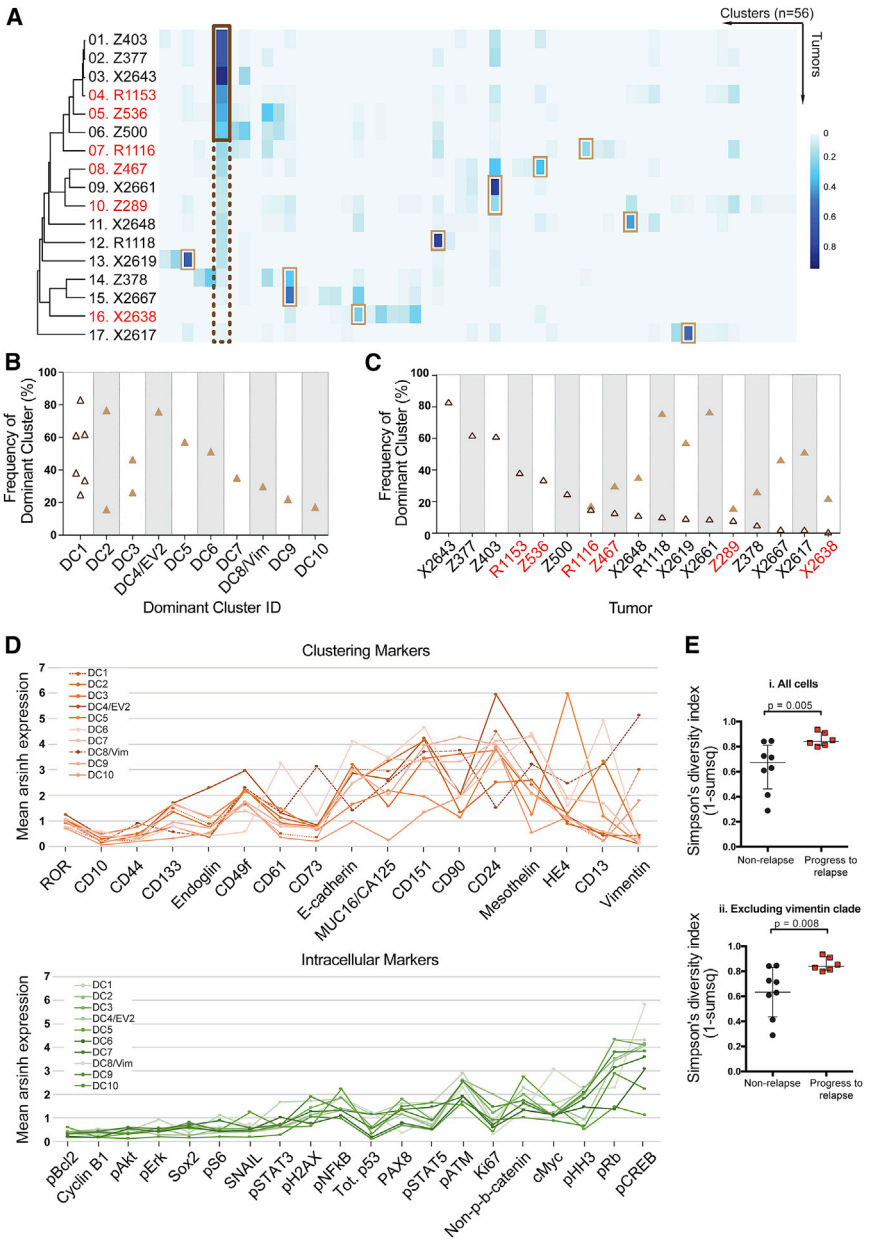

Figure 3. Novel and Dominant Cell Clusters across Individual HGSOC Tumors

(A) Heatmap depicting the cell frequency distribution within 56 clusters (columns) from each HGSOC sample (rows). Red font denotes relapse samples. Each tumor has a dominant cluster (DC), defined as a cluster with the highest frequency of cells for an individual sample. On the left-hand side, a dark brown box highlights that DC1 is dominant in tumors 1 to 6 (cell frequency > than 20%, outlined by a solid dark brown line) and is present, but not dominant, in the remaining tumors (cell frequency < 20%, outlined by a dotted dark brown line). Light brown boxes highlight DC2–DC10. DC1–DC3, DC5–DC7, DC9, and DC10 reside within the E-cadherin part of the tumor, whereas DC4 is also EV2 and DC8 is a vimentin-expressing cluster.

(B) Size (cell frequency) of DCs per tumor arranged in decreasing order. Size and co-occurrence for each DC are shown. DC1 (open dark brown triangles) occurs in six samples. DC2–DC10 are depicted by filled light brown triangles.

(C) Distribution of DCs across samples. DC1 (open triangle) is present in all tumors. DC2–DC10 (filled triangles) are present in tumors 7–17.

(D) Average mean expression levels for each of the ten DCs are shown for the 17 clustering proteins (upper panel) and 20 intracellular proteins (lower panel). The ordering of the proteins is based on the increase in variance across the DCs.

(E) Simpson's diversity index was significantly greater for patients that proceeded to relapse (n = 6) versus those that did not (n = 8). p = 0.005 or p = 0.008, including or excluding cells in the vimentin clade, respectively. Medians and interquartile ranges are shown.

See also Figure S9 and Tables S4–S6.

Spitzer et al., 2017). Pairwise Spearman correlation co-efficients were calculated, hierarchically clustered, and organized on a heatmap using the following parameters for every sample: (1) cell frequency in the 56 X-shift clusters, (2) cell frequency in the vimentin clade, (3) cell frequency in the HE4/cMyc manual gate, (4) total tumor cell frequency, and (5) Simpson's diversity index (Figure 5A). Although many correlations between the tumor cell types were interspersed within the non-relapse and relapse heatmaps, co-ordinated modules of correlations were evident. Specifically, pairwise correlations were predominantly negative for non-relapse samples (Figure 5B, block I) but overall were positive for the relapse samples (Figure 5C, block I). Pairwise positive correlations (r_s > 0.75) for relapse samples in block I were observed between cell frequencies in EV clusters 1–4, with a subgroup of E-cadherin-expressing (including DC5–DC7) and vimentin-expressing clusters. The frequency of cells in EV3 and EV4 was positively correlated with the frequency of cells in the vimentin clade. Thus, a switch from negative (non-relapse) to positive (relapse) correlations between E-cadherin clusters and vimentin clusters involves EV cells, which suggests a change in the tumor microenvironment where the metastatic trajectory in the EV cells is facilitated. By contrast, for block II, there were minimal differences in the correlations between the two patient outcomes and a notable absence of EV cluster correlations.

DISCUSSION

Genetic instability and clonal diversity characterize cancer cells and are a means by which tumors evolve and adapt to their microenvironment (Greaves, 2015; Marusyk et al., 2012; Schwarz et al., 2015). As postulated by the quasi-species

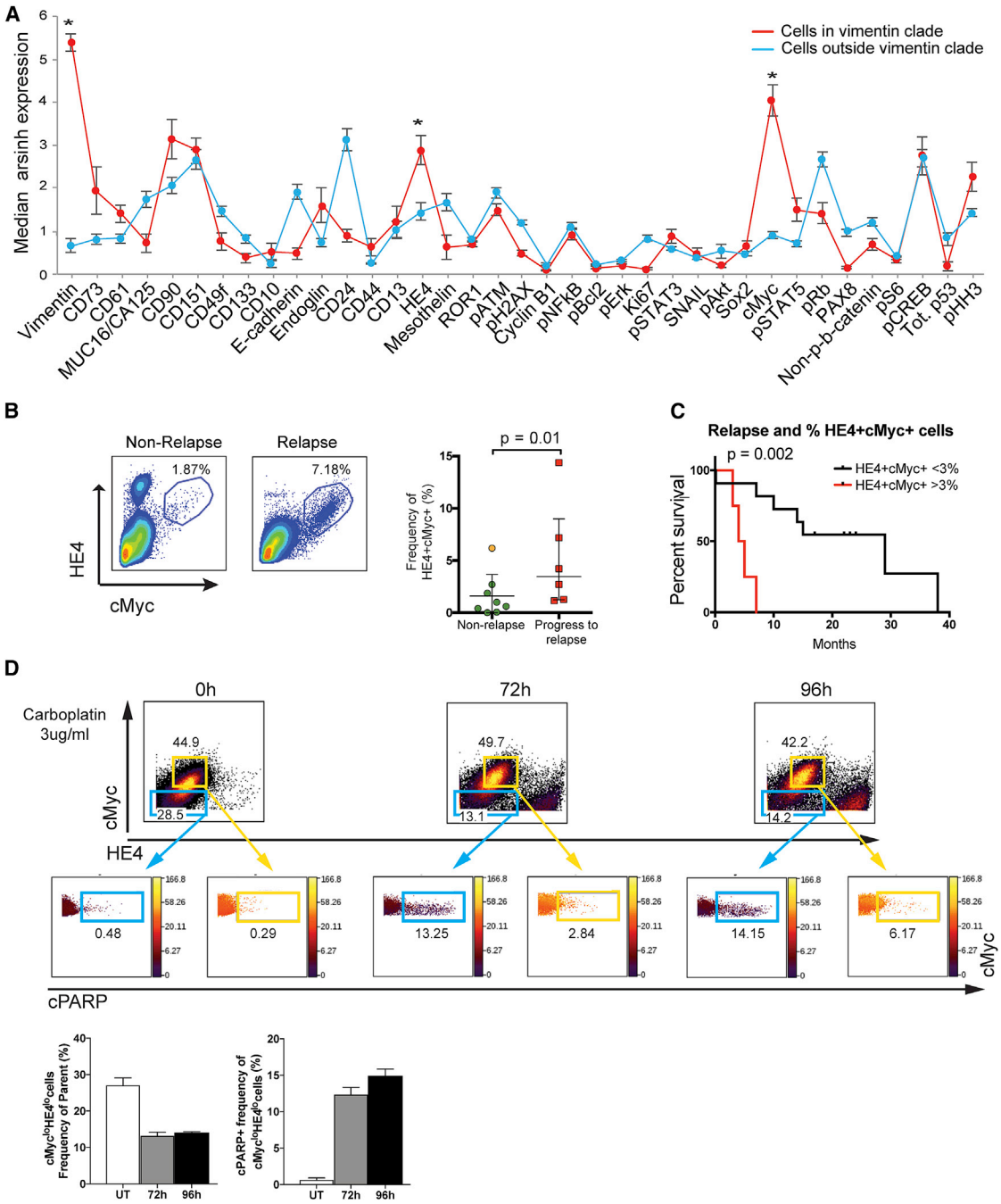

Figure 4. Novel Cell Phenotype Co-expressing Vimentin/cMyc/HE4, and Prognosis in HGSOC

(A) Median protein expression levels (95% confidence intervals) for cells inside and outside the vimentin clade (red and blue plots, respectively). Vimentin ($p = 1.62 \times 10^{-30}$), HE4 ($p = 0.0007$), and cMyc ($p = 2.3 \times 10^{-10}$) were expressed at significantly greater levels in the vimentin clade (asterisks) compared to all other tumor cells.

(B) Manual gating (representative samples shown) from the tumor cell parent population confirmed the presence of more cells co-expressing HE4 and cMyc in samples from patients that relapsed within 1 year (n = 6) versus those that did not (n = 8). The plot shows median and interquartile range for frequency of cell co-expressing HE4 and cMyc. The orange dot indicates a patient that relapsed in 13 months.

(C) Kaplan-Meier curves depict differences in time to relapse for HGSOC samples with >3% cMyc/HE4 cells (log rank test, $p = 0.0005$).

(D) TYK-nu cells were plated in 10 cm dishes and were untreated (UT) or exposed continuously to carboplatin (3 μg/mL) for 72 or 96 hr, respectively. Each 10 cm dish of cells was processed for CyTOF as described in Experimental Procedures. Flow plots show cells gated as $cMyc^{lo}/HE4^{lo}$ and $cMyc^{hi}/HE4^{hi}$ populations (blue and yellow outlines, respectively). Levels of cPARP are shown for each of these populations. The bar charts depict the mean frequency of $cMyc^{lo}/HE4^{lo}$ cells after carboplatin exposure (left) and their concomitant increases in cPARP (right). SDs are shown.

See also Figure S8.

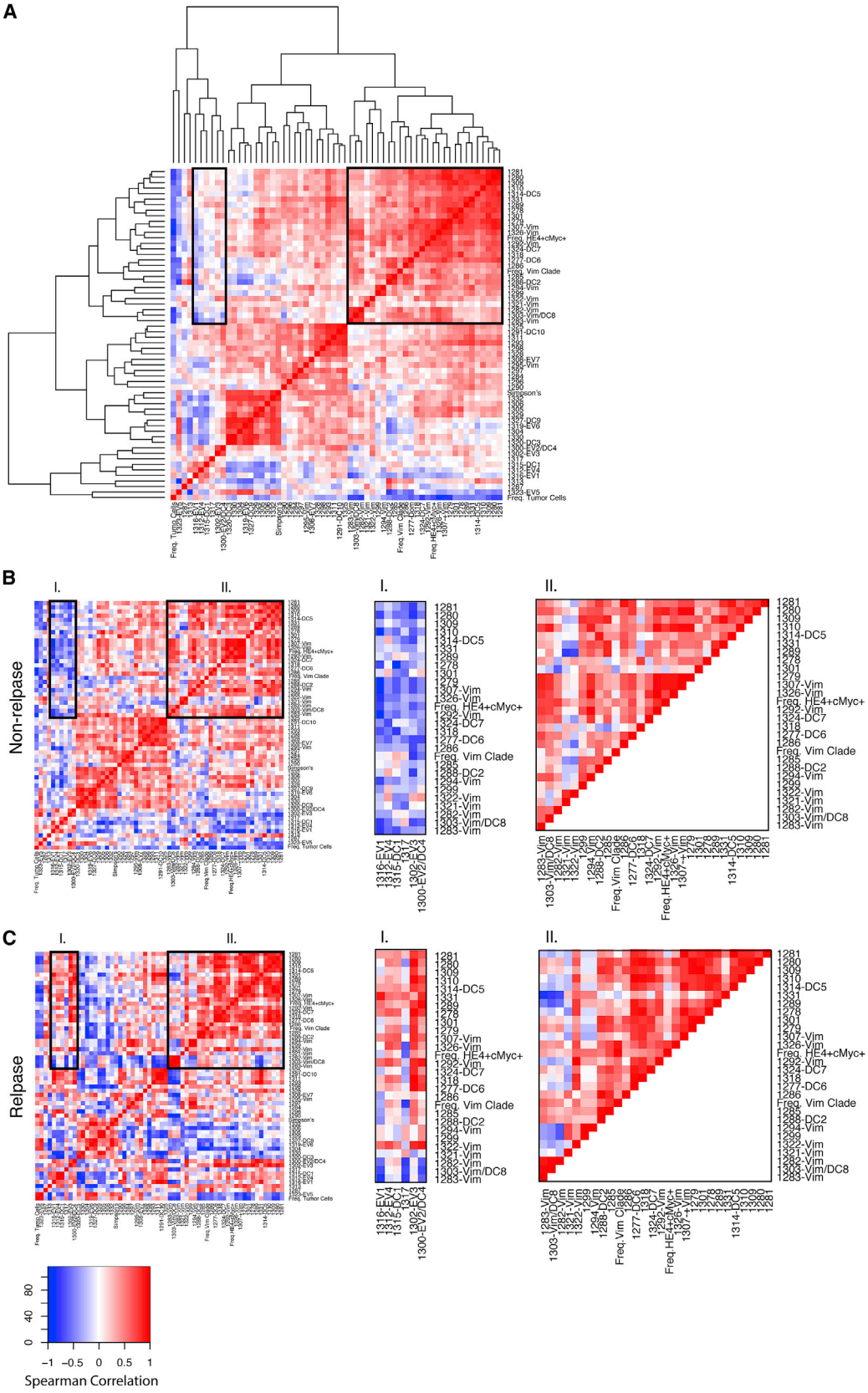

(legend on next page)

model of cancer development, constraints must exist that limit the extent of phenotypic diversity to allow tumor survival (Brumer et al., 2006). We have now shown that multiparameter single-cell CyTOF is well suited for understanding of the extent of tumor diversity. The major findings from our CyTOF study are the identification of rare HGSOC cell types recurring across the tumors, all of which would have been lost by bulk processing. Specifically, in each tumor, we identified (1) a dominant cell population, (2) EV cells with a potential role in EMT, and (3) cells co-expressing vimentin or HE4 and cMyc that correlated with poor prognosis. The revealed cell phenotypes, as well as identification of potential therapeutic targets (cell-cycle proteins, pCREB, and cMyc), present a re-evaluation of HGSOC.

Among the cell subtypes identified were ten DCs (Figures 3A–3C). The most striking finding for the DCs was that protein expression patterns for intracellular proteins showed low variability, while the clustering (mostly surface) proteins were more variable (Figure 3A). Although surface markers are often used to molecularly subclassify many tumors, measurements of intracellular signaling may be a truer reflection of disease state (Levine et al., 2015; Vogelstein et al., 2013). Specifically, the observed higher expression of pCREB and pRb in the DCs suggest a key role for these signaling molecules in ovarian cancer, as well as offering potential new therapeutic targets.

A second cell phenotype identified here involved seven EV cell clusters indicative of stabilized hybrid EMT phenotypes with the potential for metastatic conversion. These data also show the ability of CyTOF to discern subtle differences in closely related cell subtypes (Figures 2A–2C; Figure S1). The existence of an EV hybrid state has been described in ovarian cancer cell lines and inferred in HGSOC tumors based on a gene signature (Huang et al., 2013; Jolly et al., 2015, 2017), provising direct evidence of their existence in primary HGSOC tumors. The prospect of isolating EV cells by fluorescence-activated cell sorting (FACS) presents an opportunity to evaluate their roles in self-renewal, anoikis, metastasis, and therapeutic resistance (Davidson et al., 2012; Huang et al., 2013; Shibue and Weinberg, 2017; Ye and Weinberg, 2015).

A third cell phenotype pre-existing at low frequency (range < 1%–15%) in the tumors co-expressing vimentin/cMyc/HE4 and was identified in all 17 tumors. Revealing the presence of these low-frequency cells again supports the great value of single-cell analysis as enabled by CyTOF. Higher frequencies of these cells correlated with a significantly greater rate of relapse after carboplatin therapy (Figures 4B and 4C). In a follow-up experiment to elucidate the role of this cell phenotype in relapse and/or platinum resistance, we exposed the HGSOC TYK-nu cell line to carboplatin. We demonstrated that of two subpopulations co-expressing vimentin with either $cMyc^{lo}/HE4^{lo}$ or $cMyc^{hi}/HE4^{hi}$, the latter were far more resistant to carboplatin (Figure 4D). These data indicate a potential role for cMyc and HE4 acting in concert in the development of carboplatin resistance and are consistent with our patient relapse data, as well as with the recognized roles of cMyc in drug resistance (Ganesan, 2011). Sorting of vimentin/cMyc/HE4 tumor cells could confirm whether they express the transcriptomic mesenchymal signature associated with an adverse prognosis (Bowtell et al., 2015; Konecny et al., 2014; Cancer Genome Atlas Research Network, 2011). A study is in progress to develop a relatively simple and reliable test to enumerate the cells co-expressing vimentin/cMyc/HE4 for predicting response to carboplatin and/or extent of surgical debulking (Borley et al., 2012; Riester et al., 2014). In addition, these HGSOC patients may be good candidates for BrD4 inhibitors, small molecules known to disrupt cMyc function (Filippakopoulos and Knapp, 2014).

In addition, analysis of our data using the Simpson's diversity index showed that relapse cases had higher values and that the diversity resided principally within the E-cadherin-expressing (epithelial) tumor cell compartment (Figure 3E). Our results suggest that when a certain threshold of diversity in the epithelial tumor cell compartment is crossed, opportunities for metastatic conversion are increased. This agrees with data from other studies showing that increased tumor diversity is associated with poor survival (Schwarz et al., 2015; Tabassum and Polyak, 2015).

To assess how differences in tumor cell diversity influence changes in tumor cell organization, we undertook a pairwise Spearman correlation analysis and determined whether cell clusters close to a metastatic trajectory (EV) changed in concert with other cell clusters (Figure 5). In the more diverse relapse samples, positive correlations were identified between EV cell clusters and subsets of both E-cadherin- and vimentin-expressing clusters. These results supports a role for EV cells transitioning between the two compartments and, based on the clinical data, the equilibrium moving toward metastatic conversion.

In this study, we identified cell phenotypes that co-occurred across tumors with potentially critical roles in metastasis and relapse. These cells can be isolated from individual tumors and studied further, with the aim of targeted individualized therapies for HGSOC patients.

EXPERIMENTAL PROCEDURES

Ovarian Cancer Cell Lines

Kuramochi and TYK-nu cell lines (National Institute of Biomedical Innovation, Japanese Collection of Research Bioresources Cell Bank) were cultured in RPMI-1640 plus 2 mM L-glutamine (Gibco, Invitrogen) and Eagle's minimal essential medium (EMEM) (American Tissue Culture Collection), respectively. The COV362 cells (Sigma-Aldrich) were cultured in DMEM (Gibco, Invitrogen). All media were supplemented with 10% heat-inactivated fetal bovine serum (FBS) and 100 U/mL penicillin (Gibco, Invitrogen). Cells were

Figure 5. Correlations Heatmaps between Non-relapse and Relapse Patients

(A) Pairwise correlations and hierarchical clustering were performed to generate a parent heatmap with the parameters described in the text.

(B) Correlation heatmaps for non-relapse patients.

(C) Correlation heatmaps for relapse patients. Row order for (B) and (C) was imposed from hierarchical clustering of the parent heatmap (A). Two blocks of correlated modules were visually selected (black boundaries) to show differences (block I) and similarities (block II) between non-relapse and relapse patients. The colored scale shows Spearman correlation co-efficients.

split every 2–3 days and kept in a humidified cell culture incubator at 37°C with 5% CO_2.

Genomic Sequencing and Analysis for BRCA1/2 and TP53

DNA was extracted and enriched through multiplex PCR (QIAGEN QIAmp DNA Mini Kit and QIAGEN GeneRead DNaseq Targeted Ovarian V2 Panel, respectively). TrueSeq protocol was used to make an indexed Illumina sequencing library from the pooled sample amplicons. Individual sample libraries were quantitated (Qubit, Thermo Fisher Scientific), and size distribution was checked (BioAnalyzer 2100, Agilent). Pooled, normalized libraries were sequenced (Illumina MiSeq). Fastq files were generated and aligned to the HG19 build of the human genome using Burrows-Wheeler aligner (Li and Durbin, 2009). Gene variants were assessed using the Genome Analysis Toolkit (GATK) framework (McKenna et al., 2010). Pathogenic gene variants were identified using SnpEff (Cingolani et al., 2012) and annotations in dbSNP (https://www.ncbi.nlm.nih.gov/SNP) and the IARC TP53 database (http://p53.iarc.fr).

Collection of Tumor Tissue

Deidentified primary tumor samples prepared for CyTOF were purchased from Indivumed (Hamburg, Germany) over 2 years with a minimum 1-year follow-up. Two patients were lost to follow-up, and one patient died during surgery through unknown causes. This study was conducted in compliance with the Helsinki Declaration, and all patients gave written informed consent. The use of human tissue was approved and in compliance with data protection regulations regarding patient confidentiality. All patients included in the study were diagnosed with ovarian cancer. Institutional review board approval was obtained at the Physicians Association in Hamburg, Germany.

Tissue Dissociation to Prepare Single Cells

Tumor tissues were collected according to standard operating procedures to maintain sample quality while minimizing time from resection to processing. For this study, times ranged range from 2 to 5 hr, with a median of 3.5 hr. The dissociation procedure was developed at Stanford and transferred to Indivumed. The time post-resection to tumor dissociation includes placing the tumor chunk within minutes into ice-cold preservation media known to preserve phosphoproteins (Unger et al., 2015a, 2015b) for the transit time to the laboratory, where the single-cell dissociation protocol (~90 min) is performed. After surgical resection, tissue samples were transferred directly to tissue transport and preservation medium DMEM/F12 was supplemented with 10% fetal calf serum (FCS), 2 mM L-glutamine, 1% minimum essential medium (MEM) vitamins, 3% penicillin/streptomycin, 0.6% gentamicin (all from Pan Biotech), 5 μg/mL transferrin, 12.5 μg/mL fetuin, and 20 μg/mL insulin (all from Sigma-Aldrich) at 4°C–8°C and transported to the laboratory for immediate processing. After removal of fat and necrotic areas, tumor samples were chopped into small pieces for mechanical and enzymatic dissociation using settings for soft tumor dissociation on a GentleMACS Dissociator and human tumor dissociation kit (Miltenyi). Resulting single-cell suspensions were filtered through 100 and 70 μm meshes (BD Biosciences). Samples with cell viability < 60% (determined by trypan blue staining) were not included in this study, for which median viability was 74% (range of 62%–90%). Samples were then exposed to cisplatin, a live-dead exclusion marker for CyTOF (P4394, Sigma-Aldrich) (Fienberg et al., 2012). After washing, the cell pellet was resuspended and fixed in 5 mL Hank's buffered salt solution with paraformaldehyde (PFA) at a final concentration of 1.6% (Electron Microscopy Sciences) and incubated for 10 min at room temperature. Subsequently, 5 mL of cell-staining medium (CSM) (PBS with 0.5% BSA and 0.02% NaN_3) was added, the sample was centrifuged for at 2,000 rpm for 3 min, supernatants were discarded, and cell pellets were washed twice before suspension in CSM (5×10^6 cells per 0.5 mL) and then flash frozen and stored at −80°C.

Immunohistochemistry

Unstained slices (Indivumed) were from a location adjacent to the tumor piece used for single-cell dissociation. Tissue quality with low levels of necrosis was confirmed by an expert pathologist. Antigen retrieval was performed using a Decloaking Chamber (Biocare Medical) in citrate buffer at pH 6.0 at 125°C and 15 psi for 45 min. Incubation with primary antibodies was overnight at room temperature in a humidified chamber (Table S1). A Vectastain ABC Kit Elite and a Peroxidase Substrate Kit DAB (both from Vector Labs) were used for amplification and visualization of signal, respectively. Tissues known to express an antigen were used as positive controls. Antibody deletion controls were used for each antigen to confirm specific staining. All stained slides were scanned and digitized using the Aperio ScanScope AT Turbo to capture digital whole-slide images with a 20× objective lens and stored in the Aperio Spectrum Database. Quantitative image analysis was performed using Spectrum v.10 and v.11, based on the U.S. Food and Drug Administration (USFDA)-approved algorithms supplied by the manufacturer.

Antibodies for CyTOF

Antibodies (Table S3) in carrier-free PBS were conjugated to metal-chelated polymers (MaxPAR antibody conjugation kit, Fluidigm) according to the manufacturer's protocol. Antibody conjugation to bismuth was carried out using a recent protocol (Han et al., 2017). Metal-labeled antibodies were diluted to 0.2–0.4 mg/mL in antibody stabilization solution (CANDOR Biosciences) and stored at 4°C. Each antibody was titrated using cell lines and primary human samples as positive and negative controls. Antibody concentrations in experiments were based on an optimal signal-to-noise ratio (at least 2-fold for the phospho-antibodies and >6-fold for all other antibodies). Labeled ^{166}Er-CD44 and ^{89}Y-CD45 were purchased from Fluidigm. A pilot run of the entire panel was performed on three dissociated tumor samples.

Sample Processing and Antibody Staining for CyTOF

Frozen, fixed single-cell suspensions of ovarian tumors and control ovarian cancer cell lines were thawed at room temperature. For each sample, 1×10^6 cells were aliquoted into individual tubes and subjected to pre-permeabilization palladium barcoding as previously reported (Behbehani et al., 2014; Zunder et al., 2015). After barcoding, pooled cells were centrifuged and the cell pellet was incubated for 5 min at room temperature with FcX block (Biolegend) to block non-specific Fc binding. Cells were incubated with antibodies and processed for CyTOF as previously described (Bendall et al., 2011; Gaudillière et al., 2014; O'Gorman et al., 2015). Before loading into a CyTOF2 instrument (Fluidigm), cells were resuspended with a solution of normalization beads (Finck et al., 2013).

Assay Performance

CyTOF assay reproducibility was determined from tumor sample replicates in three experimental settings. In the first pilot experiment (performed in 2014), duplicates for ten samples were assayed on 2 separate days (data not shown). In the second experiment (performed in 2015 and the basis of this report), 22 samples were similarly assayed across 2 weeks. In a third experiment (2016), a subset of the 22 samples (11) was reassayed as additional quality control for long-term sample storage (Figure S2). Results were not influenced by batch effects, because samples assayed together did not group together in any of our analyses.

Evaluating the Role of HE4 and cMyc in Carboplatin Resistance

TYK-nu cells were cultured under conditions described earlier. Cell growth inhibitory effects of carboplatin (Sigma-Aldrich) were studied using the MTT assay (3-(4,5-dimethylthiazol-2-yl)-2,5-diphenyltetrazolium bromide) (Life Technologies). Carboplatin concentrations were chosen based on serum concentrations determined in patients (Arakawa et al., 2001) and our MTT half maximal inhibitory concentration (IC_{50}) values (data not shown). TYK-nu cells plated into 10 cm dishes were exposed continuously to 3 μg/mL carboplatin for either 72 or 96 hr in triplicate. All cells were harvested and bar-coded for CyTOF using procedures described earlier.

Algorithms and Data Analysis: Debarcoding

In an adaptation of the single-cell debarcoding algorithm for CyTOF data (Zunder et al., 2015), a single-cell debarcoding algorithm was written specifically for the HGSOC samples we analyzed, because they had highly varying cell sizes (e.g tumor versus immune cells). For the algorithm developed here, outliers are filtered out by applying a Pearson's correlation (r) for barcode intensity

of an individual cell to the centroid of each barcoded population. This differs from the previously reported Mahalonobis distance. Unlike the Mahalonobis distance, Pearson's r is a scaling-invariant measure, meaning that Pearson's r for two vectors remains the same when vectors are multiplied by a scalar. Invariance to vector scaling is a desirable property, because depending on their size, cells tend to absorb varying amounts of barcoding reagents and the aim was to achieve equivalent filtering for cells of all sizes. The debarcoding algorithm developed here entailed the following steps. First, the signal intensities of each barcoding channel were rescaled so that the 15th percentile became 0 and the 85th percentile became 1.0. Next, cells was assigned to a sample based on their maximum correlation to a barcode key. Then, the average intensity for the barcode channels was computed for each sample, thus creating a sample centroid vector. For each cell event, four filtering parameters were computed, which were designed to collectively identify debris, doublets, and misassigned cell events. The parameters were (1) sum of squares of barcoding channel intensities (low values, particularly those less than 1.0, are indicative of debris and removed), (2) a ratio of less than 2.0 for the averages between positive and negative barcode channels (low values, particularly less than 2.0, are indicative of doublets), (3) a Z score separation between positive and negative channels (low values, particularly those less than 2.4, are indicative of doublets), and (4) a correlation of the barcode channel profile to the sample centroid (low values, particularly those below 0.7, are indicative of cells incorrectly assigned to a given sample). Debarcoded cell events from each sample, after application of the four filtering parameters, were written into separate FCS flies (one per sample). The files were analyzed in Cytobank (http://www.cytobank.org/).

Initial Assessment of Data Quality and Gating

Initial data quality was determined using traditional cytometry statistics and visualization, such as histograms, dotplots, and heatmaps, with software available from Cytobank (Kotecha et al., 2010). Tumor cells gated as CD45−/CD31−/FAP− were used for further computationally driven analysis (Figure S3).

Clustering

The raw CyTOF data were subject to arsinh(x/5) transformation. Manually gated tumor cells from each sample were pooled together for clustering, resulting in ~800,000 cells. These cells were clustered with a density-based clustering method termed X-shift (Samusik et al., 2016). X-shift was developed to compute large multidimensional datasets and to automatically select the optimal number of cell clusters. X-shift uses the weighted K-nearest-neighbor density estimation to find the local maxima of data-point (cell event) density in a multidimensional marker space. X-shift computes the density estimate for each data point and then searches for the local density maxima, which become cell cluster centroids in a nearest-neighbor graph. The remaining data points are then connected to the centroids via density-ascending paths in the graph, thus forming cell clusters. Finally, the algorithm checks for the presence of density minima on a straight-line segment between the neighboring centroids, merging closely aligned cell clusters as necessary. Clusters separated by a Mahalanobis distance less than 2.0 were merged. The optimal nearest-neighbor parameter, K, was automatically selected to be 35 from the elbow point in a plot of the number of cell clusters versus K. All data processing was performed with the VorteX clustering environment (http://web.stanford.edu/~samusik/vortex).

MSTs

MSTs were generated by creating a graph in which all cell clusters were represented as nodes and edge weights were given by the angular distance between the median marker expression vectors, consecutively applying the standard reverse-delete algorithm on that graph (Kruskal, 1956). Layout and visualization were performed using the Gephi Toolkit 0.8.7 library. In the MST visualizations, cell clusters are arranged based on the similarity of their protein co-expression levels (Figures 2A, 2B, and 2D). Because cycles or loops are disallowed by the algorithm (MSTs are branched), clusters may be close to each other in multidimensional space yet appear farther from each other in the 2D tree representations. However, clusters on the MST that are adjacent to each other are also close in multidimensional space.

Dendrograms

Dendrograms based on the cell frequency distribution within MST clusters were generated using hierarchical agglomerative clustering implemented in the VorteX clustering environment (http://web.stanford.edu/~samusik/vortex) using an arccosine distance metric and average linkage (Figure 3A).

Statistical Analysis

All statistical analyses were performed in Microsoft Excel, Prism, and R.

Relapse versus Non-relapse Plots

One-tailed Student's t tests (uneven sample size and uneven variance) were performed on ranked transformed values due to non-normal distribution of the data. Tests were performed on eight non-relapse HGSOC samples and six that proceeded to relapse within 1 year. Three HGSOC samples were excluded from the analysis due to unavailable follow-up information (two patients lost to follow-up and one patient died during surgery from unknown causes).

Kaplan-Meier Analysis

Kaplan-Meier curves were plotted in prism. HGSOC tumor samples were stratified for time to relapse based on the presence of cMyc/HE4 cells within a sample using cell frequency thresholds computed either by k-means clustering or the median value after dividing the samples into two groups. Using a multivariate Cox-proportional hazards model, co-variates (age, weight, CA125 blood levels, and BMI) were shown to have minimal effects on the stratification (data not shown). The hazard ratio was calculated with 95% confidence intervals.

Simpson's Diversity Index

The Simpson's diversity index of the jth tumor sample was computed as $1 - \sum_{i=1}^{k} (n_{ij}/N_j)^2$, which sums each ith cluster, where i lies between 1 and k, with k being the total number of clusters. n_{ij} is the number of cells in the ith cluster that belong to the jth sample, and N_j is a total number of cells in the jth sample. The Simpson's diversity index did not correlate with either age or CA125 levels, r = 0.13 or −0.23, respectively (data not shown).

Correlation Network Analyses

For this analysis, performed in R, pairwise Spearman correlation co-efficients were calculated for all samples among the following parameters: (1) cell frequency for the 56 X-shift clusters, (2) frequency of cells in the vimentin clade, (3) frequency of manually gated HE4 and cMyc cells, (4) total tumor cell frequency, and (5) Simpson's diversity index. A heatmap was generated and organized from the hierarchical clustering of the Spearman correlation co-efficients. Using the row order from this parent matrix, the correlations were computed again for eight non-relapses and six relapse samples to produce two heatmaps (Figure 5). Modules I and II were depicted manually.

DATA AND SOFTWARE AVAILABILITY

The accession number for the CyTOF data reported in this paper is Mendeley Data: https://doi.org/10.17632/k45dgfsbhf.1. The debarcoding algorithm for CyTOF data is available at https://github.com/nolanlab/ScaleInvDBV.

SUPPLEMENTAL INFORMATION

Supplemental Information includes nine figures and six tables and can be found with this article online at https://doi.org/10.1016/j.celrep.2018.01.053.

ACKNOWLEDGMENTS

We thank Drs. James Brenton, Sylvia Plevritis, Margaret Shipp, and David Donner for critical discussions and reading the manuscript. We thank Dr. Eric Collisson, Dr. Jessica Van Ziffle, and John Greer for help with DNA sequencing. We thank Astraea Jager, Gina Jager, Angelica Trejo, Dr. James Ghadiali, Dr. Robert Balderas, and Dr. Teri Longacre for technical contributions. This work was supported by the Ovarian Cancer Teal Innovator Award

(to G.P.N. and W.J.F.) from the U.S. Department of Defense (OC110674 and W81XWH-14-1-0180) and by the NIH (grant U19AI100627-02 to G.P.N.). N.A. is supported by an Ann Schreiber Mentored Investigator Award from the Ovarian Cancer Research Fund (OCRF 292495), a Canadian Institute of Health Research (CIHR) Postdoctoral Fellowship (CIHR 321510), and an International Society for Advancement of Cytometry scholarship. E.S.S. is supported by a National Science Foundation Graduate Research Fellowship and the Gabilon Stanford Graduate Research Fellowship. T.J.K. is supported by the Chronic Lymphocytic Research Consortium (CRC).

AUTHOR CONTRIBUTIONS

V.D.G. designed and performed CyTOF experiments, analyzed and interpreted CyTOF data, and wrote the manuscript. N.S. designed experiments, analyzed and interpreted CyTOF data, and wrote the manuscript. E.S.S. designed and performed experiments. T.J.C. and N.A. designed experiments and analyzed CyTOF data. D.A.Q. analyzed genomic sequencing data. Y.-W.H., V.G., and S.-Y.C. performed CyTOF experiments. G.H. designed the bismuth conjugation protocol. A.D.B. and N.E.H. performed IHC and analyzed data. A.A., T.J.K., J.S.B., and G.P.N. designed experiments, interpreted data, and wrote the manuscript. W.J.F. designed experiments, analyzed and interpreted data, wrote the manuscript, and supervised the work.

DECLARATION OF INTERESTS

The authors declare no competing financial interests. V.D.G., N.S., J.S.B., G.P.N., and W.J.F. have a pending patent application, U.S. patent 15/275,043.

Received: December 13, 2016
Revised: December 18, 2017
Accepted: January 17, 2018
Published: February 13, 2018

REFERENCES

Ahmed, A.A., Etemadmoghadam, D., Temple, J., Lynch, A.G., Riad, M., Sharma, R., Stewart, C., Fereday, S., Caldas, C., Defazio, A., et al. (2010). Driver mutations in TP53 are ubiquitous in high grade serous carcinoma of the ovary. J. Pathol. *221*, 49–56.

Anchang, B., Hart, T.D., Bendall, S.C., Qiu, P., Bjornson, Z., Linderman, M., Nolan, G.P., and Plevritis, S.K. (2016). Visualization and cellular hierarchy inference of single-cell data using SPADE. Nat. Protoc. *11*, 1264–1279.

Arakawa, A., Nishikawa, H., Suzumori, K., and Kato, N. (2001). Pharmacokinetic and pharmacodynamic analysis of combined chemotherapy with carboplatin and paclitaxel for patients with ovarian cancer. Int. J. Clin. Oncol. *6*, 248–252.

Au-Yeung, G., Lang, F., Azar, W.J., Mitchell, C., Jarman, K.E., Lackovic, K., Aziz, D., Cullinane, C., Pearson, R.B., Mileshkin, L., et al. (2017). Selective targeting of cyclin E1-amplified high-grade serous ovarian cancer by cyclin-dependent kinase 2 and AKT inhibition. Clin. Cancer Res. *23*, 1862–1874.

Baldwin, L.A., Hoff, J.T., Lefringhouse, J., Zhang, M., Jia, C., Liu, Z., Erfani, S., Jin, H., Xu, M., She, Q.B., et al. (2014). CD151-α3β1 integrin complexes suppress ovarian tumor growth by repressing slug-mediated EMT and canonical Wnt signaling. Oncotarget *5*, 12203–12217.

Behbehani, G.K., Thom, C., Zunder, E.R., Finck, R., Gaudilliere, B., Fragiadakis, G.K., Fantl, W.J., and Nolan, G.P. (2014). Transient partial permeabilization with saponin enables cellular barcoding prior to surface marker staining. Cytometry A *85*, 1011–1019.

Bendall, S.C., Simonds, E.F., Qiu, P., Amir, E.-A.D., Krutzik, P.O., Finck, R., Bruggner, R.V., Melamed, R., Trejo, A., Ornatsky, O.I., et al. (2011). Single-cell mass cytometry of differential immune and drug responses across a human hematopoietic continuum. Science *332*, 687–696.

Bjornson, Z.B., Nolan, G.P., and Fantl, W.J. (2013). Single-cell mass cytometry for analysis of immune system functional states. Curr. Opin. Immunol. *25*, 484–494.

Borley, J., Wilhelm-Benartzi, C., Brown, R., and Ghaem-Maghami, S. (2012). Does tumour biology determine surgical success in the treatment of epithelial ovarian cancer? A systematic literature review. Br. J. Cancer *107*, 1069–1074.

Bowtell, D.D., Böhm, S., Ahmed, A.A., Aspuria, P.J., Bast, R.C., Jr., Beral, V., Berek, J.S., Birrer, M.J., Blagden, S., Bookman, M.A., et al. (2015). Rethinking ovarian cancer II: reducing mortality from high-grade serous ovarian cancer. Nat. Rev. Cancer *15*, 668–679.

Brumer, Y., Michor, F., and Shakhnovich, E.I. (2006). Genetic instability and the quasispecies model. J. Theor. Biol. *241*, 216–222.

Cancer Genome Atlas Research Network (2011). Integrated genomic analyses of ovarian carcinoma. Nature *474*, 609–615.

Chen, G.M., Kannan, L., Geistlinger, L., Kofia, V., Safikhani, Z., Gendoo, D.M.A., Parmigiani, G., Birrer, M., Haibe-Kains, B., and Waldron, L. (2017). Consensus on molecular subtypes of ovarian cancer. Published online July 12, 2017. 10.1101/162685.

Cingolani, P., Platts, A., Wang, L., Coon, M., Nguyen, T., Wang, L., Land, S.J., Lu, X., and Ruden, D.M. (2012). A program for annotating and predicting the effects of single nucleotide polymorphisms, SnpEff: SNPs in the genome of *Drosophila melanogaster* strain w1118; iso-2; iso-3. Fly (Austin) *6*, 80–92.

Ciriello, G., Miller, M.L., Aksoy, B.A., Senbabaoglu, Y., Schultz, N., and Sander, C. (2013). Emerging landscape of oncogenic signatures across human cancers. Nat. Genet. *45*, 1127–1133.

Coscia, F., Watters, K.M., Curtis, M., Eckert, M.A., Chiang, C.Y., Tyanova, S., Montag, A., Lastra, R.R., Lengyel, E., and Mann, M. (2016). Integrative proteomic profiling of ovarian cancer cell lines reveals precursor cell associated proteins and functional status. Nat. Commun. *7*, 12645.

Davidson, B. (2016). CD24 is highly useful in differentiating high-grade serous carcinoma from benign and malignant mesothelial cells. Hum. Pathol. *58*, 123–127.

Davidson, B., Tropé, C.G., and Reich, R. (2012). Epithelial-mesenchymal transition in ovarian carcinoma. Front. Oncol. *2*, 33.

Etemadmoghadam, D., George, J., Cowin, P.A., Cullinane, C., Kansara, M., Gorringe, K.L., Smyth, G.K., and Bowtell, D.D.; Australian Ovarian Cancer Study Group (2010). Amplicon-dependent CCNE1 expression is critical for clonogenic survival after cisplatin treatment and is correlated with 20q11 gain in ovarian cancer. PLoS ONE *5*, e15498.

Fienberg, H.G., Simonds, E.F., Fantl, W.J., Nolan, G.P., and Bodenmiller, B. (2012). A platinum-based covalent viability reagent for single-cell mass cytometry. Cytometry A *81*, 467–475.

Filippakopoulos, P., and Knapp, S. (2014). Targeting bromodomains: epigenetic readers of lysine acetylation. Nat. Rev. Drug Discov. *13*, 337–356.

Finck, R., Simonds, E.F., Jager, A., Krishnaswamy, S., Sachs, K., Fantl, W., Pe'er, D., Nolan, G.P., and Bendall, S.C. (2013). Normalization of mass cytometry data with bead standards. Cytometry A *83*, 483–494.

Ganesan, S. (2011). MYC, PARP1, and chemoresistance: BIN there, done that? Sci. Signal. *4*, pe15.

Gaudillière, B., Fragiadakis, G.K., Bruggner, R.V., Nicolau, M., Finck, R., Tingle, M., Silva, J., Ganio, E.A., Yeh, C.G., Maloney, W.J., et al. (2014). Clinical recovery from surgery correlates with single-cell immune signatures. Sci. Transl. Med. *6*, 255ra131.

Greaves, M. (2015). Evolutionary determinants of cancer. Cancer Discov. *5*, 806–820.

Han, G., Chen, S.Y., Gonzalez, V.D., Zunder, E.R., Fantl, W.J., and Nolan, G.P. (2017). Atomic mass tag of bismuth-209 for increasing the immunoassay multiplexing capacity of mass cytometry. Cytometry A. *91*, 1150–1163.

Hemler, M.E. (2014). Tetraspanin proteins promote multiple cancer stages. Nat. Rev. Cancer *14*, 49–60.

Horowitz, A., Strauss-Albee, D.M., Leipold, M., Kubo, J., Nemat-Gorgani, N., Dogan, O.C., Dekker, C.L., Mackey, S., Maecker, H., Swan, G.E., et al. (2013). Genetic and environmental determinants of human NK cell diversity revealed by mass cytometry. Sci. Transl. Med. *5*, 208ra145.

Hotson, A.N., Gopinath, S., Nicolau, M., Khasanova, A., Finck, R., Monack, D., and Nolan, G.P. (2016). Coordinate actions of innate immune responses oppose those of the adaptive immune system during Salmonella infection of mice. Sci. Signal. *9*, ra4.

Huang, R.Y., Wong, M.K., Tan, T.Z., Kuay, K.T., Ng, A.H., Chung, V.Y., Chu, Y.S., Matsumura, N., Lai, H.C., Lee, Y.F., et al. (2013). An EMT spectrum defines an anoikis-resistant and spheroidogenic intermediate mesenchymal state that is sensitive to e-cadherin restoration by a src-kinase inhibitor, saracatinib (AZD0530). Cell Death Dis. *4*, e915.

Ideker, T., and Krogan, N.J. (2012). Differential network biology. Mol. Syst. Biol. *8*, 565.

Jiang, S.W., Chen, H., Dowdy, S., Fu, A., Attewell, J., Kalogera, E., Drapkin, R., Podratz, K., Broaddus, R., and Li, J. (2013). HE4 transcription- and splice variants-specific expression in endometrial cancer and correlation with patient survival. Int. J. Mol. Sci. *14*, 22655–22677.

Jolly, M.K., Boareto, M., Huang, B., Jia, D., Lu, M., Ben-Jacob, E., Onuchic, J.N., and Levine, H. (2015). Implications of the hybrid epithelial/mesenchymal phenotype in metastasis. Front. Oncol. *5*, 155.

Jolly, M.K., Ward, C., Eapen, M.S., Myers, S., Hallgren, O., Levine, H., and Sohal, S.S. (2017). Epithelial-mesenchymal transition, a spectrum of states: role in lung development, homeostasis, and disease. Dev. Dyn., Published online July 21, 2017. 10.1002/dvdy.24541.

Köbel, M., Piskorz, A.M., Lee, S., Lui, S., LePage, C., Marass, F., Rosenfeld, N., Mes Masson, A.M., and Brenton, J.D. (2016). Optimized p53 immunohistochemistry is an accurate predictor of TP53 mutation in ovarian carcinoma. J. Pathol. Clin. Res. *2*, 247–258.

Konecny, G.E., Wang, C., Hamidi, H., Winterhoff, B., Kalli, K.R., Dering, J., Ginther, C., Chen, H.W., Dowdy, S., Cliby, W., et al. (2014). Prognostic and therapeutic relevance of molecular subtypes in high-grade serous ovarian cancer. J. Natl. Cancer Inst. *106*, dju249.

Kotecha, N., Krutzik, P.O., and Irish, J.M. (2010). Web-based analysis and publication of flow cytometry experiments. Curr. Protoc. Cytom. *53*, 10.17.1–10.17.24.

Krogan, N.J., Lippman, S., Agard, D.A., Ashworth, A., and Ideker, T. (2015). The cancer cell map initiative: defining the hallmark networks of cancer. Mol. Cell *58*, 690–698.

Kruskal, J.B. (1956). On the shortest spanning subtree of a graph and the traveling salesman problem. Proc. Am. Math. Soc. *7*, 48–50.

Krzystyniak, J., Ceppi, L., Dizon, D.S., and Birrer, M.J. (2016). Epithelial ovarian cancer: the molecular genetics of epithelial ovarian cancer. Ann. Oncol. *27* (*Suppl 1*), i4–i10.

Levine, J.H., Simonds, E.F., Bendall, S.C., Davis, K.L., Amir, A.D., Tadmor, M.D., Litvin, O., Fienberg, H.G., Jager, A., Zunder, E.R., et al. (2015). Data-driven phenotypic dissection of AML reveals progenitor-like cells that correlate with prognosis. Cell *162*, 184–197.

Li, H., and Durbin, R. (2009). Fast and accurate short read alignment with Burrows-Wheeler transform. Bioinformatics *25*, 1754–1760.

Li, J., Chen, H., Mariani, A., Chen, D., Klatt, E., Podratz, K., Drapkin, R., Broaddus, R., Dowdy, S., and Jiang, S.W. (2013). HE4 (WFDC2) promotes tumor growth in endometrial cancer cell lines. Int. J. Mol. Sci. *14*, 6026–6043.

Li, J., Chen, H., Curcuru, J.R., Patel, S., Johns, T.O., Patel, D., Qian, H., and Jiang, S.W. (2017). Serum HE4 level as a biomarker to predict the recurrence of gynecologic cancers. Curr. Drug Targets *18*, 1158–1164.

Lu, R., Sun, X., Xiao, R., Zhou, L., Gao, X., and Guo, L. (2012). Human epididymis protein 4 (HE4) plays a key role in ovarian cancer cell adhesion and motility. Biochem. Biophys. Res. Commun. *419*, 274–280.

Marusyk, A., Almendro, V., and Polyak, K. (2012). Intra-tumour heterogeneity: a looking glass for cancer? Nat. Rev. Cancer *12*, 323–334.

Matulonis, U.A., Sood, A.K., Fallowfield, L., Howitt, B.E., Sehouli, J., and Karlan, B.Y. (2016). Ovarian cancer. Nat. Rev. Dis. Primers *2*, 16061.

McAllister, S.S., and Weinberg, R.A. (2014). The tumour-induced systemic environment as a critical regulator of cancer progression and metastasis. Nat. Cell Biol. *16*, 717–727.

McKenna, A., Hanna, M., Banks, E., Sivachenko, A., Cibulskis, K., Kernytsky, A., Garimella, K., Altshuler, D., Gabriel, S., Daly, M., and DePristo, M.A. (2010). The Genome Analysis Toolkit: a MapReduce framework for analyzing next-generation DNA sequencing data. Genome Res. *20*, 1297–1303.

Medrano, M., Communal, L., Brown, K.R., Iwanicki, M., Normand, J., Paterson, J., Sircoulomb, F., Krzyzanowski, P., Novak, M., Doodnauth, S.A., et al. (2017). Interrogation of functional cell-surface markers identifies CD151 dependency in high-grade serous ovarian cancer. Cell Rep. *18*, 2343–2358.

Moore, R.G., Hill, E.K., Horan, T., Yano, N., Kim, K., MacLaughlan, S., Lambert-Messerlian, G., Tseng, Y.D., Padbury, J.F., Miller, M.C., et al. (2014). HE4 (WFDC2) gene overexpression promotes ovarian tumor growth. Sci. Rep. *4*, 3574.

O'Gorman, W.E., Hsieh, E.W., Savig, E.S., Gherardini, P.F., Hernandez, J.D., Hansmann, L., Balboni, I.M., Utz, P.J., Bendall, S.C., Fantl, W.J., et al. (2015). Single-cell systems-level analysis of human Toll-like receptor activation defines a chemokine signature in patients with systemic lupus erythematosus. J. Allergy Clin. Immunol. *136*, 1326–1336.

Riester, M., Wei, W., Waldron, L., Culhane, A.C., Trippa, L., Oliva, E., Kim, S.H., Michor, F., Huttenhower, C., Parmigiani, G., and Birrer, M.J. (2014). Risk prediction for late-stage ovarian cancer by meta-analysis of 1525 patient samples. J. Natl. Cancer Inst. *106*, dju048.

Samusik, N., Good, Z., Spitzer, M.H., Davis, K.L., and Nolan, G.P. (2016). Automated mapping of phenotype space with single-cell data. Nat. Methods *13*, 493–496.

Schwarz, R.F., Ng, C.K., Cooke, S.L., Newman, S., Temple, J., Piskorz, A.M., Gale, D., Sayal, K., Murtaza, M., Baldwin, P.J., et al. (2015). Spatial and temporal heterogeneity in high-grade serous ovarian cancer: a phylogenetic analysis. PLoS Med. *12*, e1001789.

Shibue, T., and Weinberg, R.A. (2017). EMT, CSCs, and drug resistance: the mechanistic link and clinical implications. Nat. Rev. Clin. Oncol. *14*, 611–629.

Spitzer, M.H., and Nolan, G.P. (2016). Mass cytometry: single cells, many features. Cell *165*, 780–791.

Spitzer, M.H., Carmi, Y., Reticker-Flynn, N.E., Kwek, S.S., Madhireddy, D., Martins, M.M., Gherardini, P.F., Prestwood, T.R., Chabon, J., Bendall, S.C., et al. (2017). Systemic immunity is required for effective cancer immunotherapy. Cell *168*, 487–502.e15.

Stewart, J.M., Shaw, P.A., Gedye, C., Bernardini, M.Q., Neel, B.G., and Ailles, L.E. (2011). Phenotypic heterogeneity and instability of human ovarian tumor-initiating cells. Proc. Natl. Acad. Sci. USA *108*, 6468–6473.

Tabassum, D.P., and Polyak, K. (2015). Tumorigenesis: it takes a village. Nat. Rev. Cancer *15*, 473–483.

Tothill, R.W., Tinker, A.V., George, J., Brown, R., Fox, S.B., Lade, S., Johnson, D.S., Trivett, M.K., Etemadmoghadam, D., Locandro, B., et al.; Australian Ovarian Cancer Study Group (2008). Novel molecular subtypes of serous and endometrioid ovarian cancer linked to clinical outcome. Clin. Cancer Res. *14*, 5198–5208.

Unger, F., Bentz, S., Kruger, J., Rosenbrock, C., Schaller, J., Pursche, K., Sprussel, A., Juhl, H., and David, K. (2015a). Precision cut cancer tissue slices in anti-cancer drug testing. J. Mol. Pathophysiol. *4*, 108.

Unger, F.T., Krüger, J., Juhl, H., and David, K.A. (2015b). Drug profiling in precision cut cancer tumor slices: analysis of therapeutic antibodies in colorectal cancer. Int. J. Cancer Immunol. Immun. *1*, 1–8.

Vogelstein, B., Papadopoulos, N., Velculescu, V.E., Zhou, S., Diaz, L.A., Jr., and Kinzler, K.W. (2013). Cancer genome landscapes. Science *339*, 1546–1558.

Wang, Z.C., Birkbak, N.J., Culhane, A.C., Drapkin, R., Fatima, A., Tian, R., Schwede, M., Alsop, K., Daniels, K.E., Piao, H., et al.; Australian Ovarian Cancer Study Group (2012). Profiles of genomic instability in high-grade serous ovarian cancer predict treatment outcome. Clin. Cancer Res. *18*, 5806–5815.

Ye, X., and Weinberg, R.A. (2015). Epithelial-mesenchymal plasticity: a central regulator of cancer progression. Trends Cell Biol. *25*, 675–686.

Zhang, S., Cui, B., Lai, H., Liu, G., Ghia, E.M., Widhopf, G.F., 2nd, Zhang, Z., Wu, C.C., Chen, L., Wu, R., et al. (2014). Ovarian cancer stem cells express ROR1, which can be targeted for anti-cancer-stem-cell therapy. Proc. Natl. Acad. Sci. USA *111*, 17266–17271.

Zhang, H., Liu, T., Zhang, Z., Payne, S.H., Zhang, B., McDermott, J.E., Zhou, J.Y., Petyuk, V.A., Chen, L., Ray, D., et al.; CPTAC Investigators (2016). Integrated proteogenomic characterization of human high-grade serous ovarian cancer. Cell *166*, 755–765.

Zunder, E.R., Finck, R., Behbehani, G.K., Amir, E.-A.D., Krishnaswamy, S., Gonzalez, V.D., Lorang, C.G., Bjornson, Z., Spitzer, M.H., Bodenmiller, B., et al. (2015). Palladium-based mass tag cell barcoding with a doublet-filtering scheme and single-cell deconvolution algorithm. Nat. Protoc. *10*, 316–333.

ORIGINAL ARTICLE

Cytometry PART A
Journal of the International Society for Advancement of Cytometry

MIFlowCyt

High-Throughput Precision Measurement of Subcellular Localization in Single Cells

Tyler J. Burns,[1] Andreas P. Frei,[2†] Pier F. Gherardini,[2†] Felice A. Bava,[2] Jake E. Batchelder,[3] Yuki Yoshiyasu,[4] Julie M. Yu,[5] Amanda R. Groziak,[6] Samuel C. Kimmey,[7] Veronica D. Gonzalez,[2] Wendy J. Fantl,[8‡⋆] Garry P. Nolan[9‡⋆]

[1]Department of Cancer Biology, Stanford University School of Medicine, Stanford, California

[2]Stanford University School of Medicine, Baxter Laboratory for Stem Cell Biology, Stanford, California

[3]Immunology and Microbial Pathogenesis, Joan and Sanford I. Weill Medical College of Cornell University, New York, New York

[4]Department of Medicine, University of Texas Health Science Center at San Antonio, San Antonio, Texas

[5]Department of Biological Sciences, University of California Berkeley, Berkeley, California

[6]Department of Biology, Barnard College, New York, New York

[7]Developmental Biology, Stanford University School of Medicine, Stanford, California

[8]Stanford Comprehensive Cancer Institute and Department of Obstetrics and Gynecology, Stanford University, Stanford, California

[9]Department of Microbiology and Immunology, Stanford University, Stanford, California

Received 13 October 2016; Revised 13 December 2016; Accepted 28 December 2016

Additional Supporting Information may be found in the online version of this article.

†These authors contributed equally to this work.
‡Co-senior authors.

ISAC
International Society for Advancement of Cytometry

• **Abstract**

To quantify visual and spatial information in single cells with a throughput of thousands of cells per second, we developed Subcellular Localization Assay (SLA). This adaptation of Proximity Ligation Assay expands the capabilities of flow cytometry to include data relating to localization of proteins to and within organelles. We used SLA to detect the nuclear import of transcription factors across cell subsets in complex samples. We further measured intranuclear re-localization of target proteins across the cell cycle and upon DNA damage induction. SLA combines multiple single-cell methods to bring about a new dimension of inquiry and analysis in complex cell populations.

• **Key terms**

proximity ligation assay; subcellular localization; nuclear localization; DNA damage response

CELLS can efficiently respond to a dynamic environment by re-localizing proteins both between and within intracellular compartments. Thus, quantifying localization of proteins to specific intracellular structures is fundamental for understanding cell behavior, both in normal and diseased conditions.

Immunofluorescence microscopy (IFM) is often used for obtaining such information. With IFM one can visually estimate co-localization of a protein with intracellular structures provided there exist antibodies or dyes for each, though throughput is typically low. In addition, imaging flow cytometry (1) has been a useful addition to the field with a much higher throughput than IFM (up to 5000 cells per second), but currently limited availability.

It would be optimal to obtain such information with traditional flow cytometry, a well-entrenched technology with throughput of >10,000 cells per second, and a much wider availability in both hospitals and laboratories (2). Within flow cytometry, one can use phosphorylation of specific proteins as an approximation for their activation (e.g. phosphorylation of a transcription factor associated with nuclear localization), provided one has an antibody for a phosphorylation site sufficiently studied to make such an assumption (3). Thus, a flow cytometric readout of a single phosphorylation site of a specific protein may only provide limited information about its varied activation states, and is therefore not always a suitable proxy for localization. Moreover, protein localization to "protein neighborhoods" within cells is important. The presence of two or more proteins in a given locale is often an indicator of a series of mechanistically determined events whose consummation is the goal of the machine being built.

Other than nanoscale imaging, proxies have been developed to indicate locale. One approach used for over 30 years is fluorescence resonance energy transfer, either

*Correspondence to: Garry P. Nolan; Microbiology and Immunology, Stanford University, CCSR R3205 269 Campus Drive, Stanford, CA 94305.
E-mail: gnolan@stanford.edu and Wendy J. Fantl, Stanford Comprehensive Cancer Institute and Department of Obstetrics and Gynecology, Stanford University, Stanford, CA. E-mail: wjfantl@stanford.edu

Published online 17 January 2017 in Wiley Online Library (wileyonlinelibrary.com)
DOI: 10.1002/cyto.a.23054

with chemical or genetically encoded fluorophores (4). This requires previous tagging of the molecules in question and might interfere with their supposed functions. Another method involves "splitting" of enzymatic functions into separate sub-proteins (5). Again, this involves most often the creation of genetic fusion events. In each of these cases the co-localization of proteins in the cell creates an "event" that can thus be read. Finally, a method recently described allows for rough approximation of protein location within a given cell by analyzing pulse width and height of a fluorescently labeled protein with flow cytometry (6). However, one may want a quantitative readout based not on location within a cell or phosphorylation, but rather from molecularly tagging these said events at specific subcellular structures of interest by relative proximity without creating genetic fusion events.

Here, we utilized the Proximity Ligation Assay (7) method to measure proximal co-localization of specific proteins to specific subcellular compartments with flow cytometry. This adaptation, herein termed Subcellular Localization Assay (SLA), is extensible to IFM, CyTOF, MIBI, and other detection systems. SLA quantifies localization of any given protein, for which there exists a representative antibody, and a second molecular tag for the subcellular structure with which the first protein interacts. The system is compatible with simultaneous detection of additional cell surface or intracellular markers in primary cells. Importantly, the method does not require instrument modifications or new analysis software.

We first measured nuclear import with flow cytometry by detecting proximity of antibodies against transcription factors to a previously validated antibody against double-stranded DNA (dsDNA) (8). We next measured DNA repair by re-localization of nuclear proteins to sites of DNA damage. This was achieved by detecting proximity of antibodies against DNA repair protein BRCA1 to antibodies against DNA damage marker γH2AX. Changes in localization were quantified by the increase or decrease in the observed SLA signal. Here, we performed SLA simultaneously with a DAPI stain for cell cycle analysis. Combining quantitative and high throughput measurements of subcellular localization with protein function in primary cells provide opportunities for understanding basic cellular mechanisms with implications in health and disease.

Methods and Materials

Cell Lines and Samples

All cell lines described below were of human origin. Non-adherent cell lines (U-937, THP-1, Jurkat) were purchased from ATCC (Manassas, VA). U-937 and THP-1 cell lines are monocytic, and the Jurkat cell line is T-lymphocytic. These cell lines were cultured in Dulbecco's RPMI-1640 (Life Technologies, Carlsbad, CA), with 10% FBS (Thermo Fisher Scientific, Waltham, MA), 1% Penicillin/Streptomycin (Life Technologies) and 1% Glutamine (Life Technologies) added, maintaining a density on average between 500K and 1M cells per mL. The TYK-nu cell line was derived from an ovary with undifferentiated carcinoma. It was obtained from JCRB Cell Bank (Ibaraki, Japan) for our use. TYK-nu cells were cultured in Eagle's Minimum Essential Medium (ATCC) with 10% FBS and 1% Penicillin/Streptomycin added. All aforementioned cell lines were cultured at 37°C in a 5% CO_2 atmosphere.

Human peripheral blood was obtained from the Stanford University Blood center from anonymous healthy human donors. Collection procedure followed a Stanford University Institutional Review Board-approved protocol. SLA experiments used peripheral blood mononuclear cells (PBMCs) isolated using Ficoll Plaque Plus (Thermo Fisher Scientific). For these experiments, PBMCs were used fresh.

Cell Stimulation, Treatment, and Processing

U937 and THP-1 human monocytic cells were stimulated with 10 ng/mL recombinant human TNFα (R&D Systems, Minneapolis, MN) for 15 min, and Jurkat cells as well as human PBMCs were stimulated with 250 nM PMA (Sigma-Aldrich) and 1 μM ionomycin (Sigma-Aldrich, St. Louis, MO) for 60 min in complete RPMI. PBMCs were stimulated with 50 ng/mL TNFα or 5 μg/mL ultrapure lipopolysaccharide (LPS) (InvivoGen, San Diego, CA) for times specified in complete RPMI. Cells were incubated gentle shaking at 37°C. TYK-nu cells were treated with 10 Gy of γ radiation using Cesium 137 at a dose of 8 gy/min. Following irradiation, cells were incubated at 37° for 6 h before they were processed.

Following pathway stimulation treatments described above, cell lines were fixed at a density of 1×10^6 cells/mL, and PBMCs were fixed at a density of 5×10^6 cells/mL. Fixation occurred in 1.6% paraformaldehyde (Electron Microscopy Services, Hatfield, PA) for 10 min at room temperature. Of note, all paraformaldehyde solutions described in this manuscript came from 16% stock samples, diluted into relevant cell culture media. Following fixation, cells were permeabilized in 100% methanol (Thermo Fisher Scientific) on ice for 15 min. These fixation and permeabilization conditions are a standard for our lab, as previously described (9).

For DNA damage experiments, irradiated cells were pre-extracted with 0.5% NP-40 (Abcam, Cambridge, England) in PBS (Life Technologies) for 5 minutes on ice, and fixed in 4% paraformaldehyde (Electron Microscopy Services) for an additional 20 min at room temperature as described previously (10). The higher percentage of paraformaldehyde was used to

counteract the increase in cell loss observed in pre-extracted cells during each wash step. Pre-extracted cells were not permeabilized with methanol.

Preparation of Proximity Probes

Donkey anti-mouse and anti-rabbit secondary antibodies (Jackson Immunoresearch Labs, West Grove, PA) were conjugated to a heterobifunctional sulfo-SMCC linker (Thermo Fisher Scientific). The linker was added at a molar excess of 25 to 1 with an antibody concentration of 1.3 mg/mL. Samples were incubated at room temperature for 45 min. Unconjugated SMCC linker was removed using 50-kDa Centricon filters (Thermo Fisher Scientific). Samples were filtered twice with addition of PBS after a spin at 12,000 g for 10 min. Samples were resuspended in 50 μL in PBS.

Oligonucleotides with a C6-thol modifier conjugated on the 5′ end (Stanford Protein and Nucleic Acid facility, Stanford, CA) were conjugated to the respective antibody-SMCC linker conjugates. In parallel to the antibody-SMCC incubation step, oligonucleotides were deprotected using 5 mM TCEP (Thermo Fisher Scientific) in 0.5× PBS for 20 min at 37°C. TCEP was removed by precipitation from 0.3M sodium acetate and 70% ethanol. Oligonucleotides were resuspended in PBS with 1 M NaCl. Oligonucleotides were added at a 5 to 1 molar excess to 1.3 mg/mL SMCC-conjugated antibody and incubated overnight at 4°C. Samples were then purified through Centricon filters as described above. PBS-based antibody stabilizer (Boca Scientific, Boca Raton, FL) was added until the antibody concentration was approximately 1 mg/mL. In total, this procedure takes approximately one and a half hours of physical labor on day one, an overnight incubation, and another 30 min for the purification step on day two. Efficacy of antibody-oligonucleotide conjugation was evaluated by SDS-PAGE using Simply Blue Safe Stain (Life Technologies) for protein detection and SYBR-Gold (Life Technologies) for DNA detection. Each conjugate was further evaluated by SLA for the dsDNA:histone H3 interaction over a range of concentrations to optimize signal-to-noise ratio.

SLA Protocol

For all experiments with PBMCs, cells were barcoded according to treatment condition with different concentrations of Pacific Orange NHS fluorophores (Thermo Fisher Scientific) as previously described (11). Cells were then placed into PCR tubes for antibody staining and subsequent steps at a density of 1 million cells per 100 μL. The following primary antibodies were used in this study: CD45 (Biolegend, clone H130, San Diego, CA) 2 μg/mL, dsDNA (Abcam, clone 35I9) 0.5 μg/mL, NF-κB (Abcam, polyclonal) 2 μg/mL, histone H3 (Abcam, polyclonal), 2 μg/mL, NFAT (Cell Signaling Technology, Danvers, MA), 1:200 dilution—mass not specified, Cytochrome C (Cell Signaling Technology), 1:500—mass not specified, COXIV (Cell Signaling Technology), 1:500—mass not specified, H2AX, pSer139 (Millipore, clone JBW301, Darmstadt, Germany), BRCA1 (Santa Cruz Biotechnology, clone C20, Dallas, TX). Barcoded samples were incubated with the antibodies at 4°C overnight (approximately 15 h) in PBS with 5 mg/mL BSA (Santa Cruz Biotechnology) and 0.02% sodium azide (Sigma-Aldrich). Cells were subsequently washed three times with PBS containing 5 mg/mL BSA and 0.02% sodium azide, and secondary antibodies conjugated to proximity probes were added. The master mix contained 100 μg/mL sheared salmon sperm DNA (Life Technologies) and 3 μg/mL proximity probes (anti-mouse and anti-rabbit) in the aforementioned wash buffer. Cells were incubated for 1 h at room temperature on an inverter. For subsequent steps to the end, cells were washed in PBS with 0.1% Tween. Following secondary antibody incubation, 100 nM backbone and 100 nM insert oligonucleotides with 10 μg/mL of salmon sperm DNA were added in PBS with 0.1% tween. Cells were incubated for 30 min at 37°C. Next, the oligonucleotides were ligated in 1× ligation buffer (Thermo Fisher Scientific), T4 DNA Ligase 10 U/mL, and 10 μg/mL sheared salmon sperm DNA. Following this, rolling circle amplification of the circularized oligonucleotide product was performed in 1× phi29 polymerase buffer (Thermo Fisher Scientific), 125 U/mL phi29 polymerase (Thermo Fisher Scientific), and 250 μM each dNTP (Thermo Fisher Scientific). Samples were incubated for 90 min at 37°C. We determined that longer amplification times (as long as overnight) could be used for interactions that produce low signals, After three washes with PBST, detection oligonucleotides labeled with Alexa 647 were added for a final concentration of 200 nM (Olink Biosciences, Uppsala, Sweden). It was also determined that this surface/intracellular staining step could occur following the addition of the secondary oligonucleotide conjugated probes in the beginning of the procedure, but the strength of signal was no different (data not shown), and the simultaneous staining with the detection reagents saved time. For experiments containing PBMCs, the following fluorescently conjugated antibodies were added for additional surface and intracellular staining: IκBα Alexa 488 (Cell Signaling Technology, clone L35A5), CD3 PE (BD Biosciences, Clone HIT3A, San Jose, CA), CD7 Alexa 700 (BD Biosciences, Clone M-T701). Samples were incubated at 37°C for 30 min. For DNA damage experiments, one subsequent step was added, wherein cells were incubated with 0.25μg/mL DAPI (Sigma-Aldrich) for 30 min. In total, the SLA procedure described above takes approximately one hour for cell prep and primary antibody staining on day one, followed by an overnight incubation, followed by six hours of on the second day for the remaining steps and flow cytometry.

Data Acquisition and Analysis

Following SLA, cells were analyzed on an LSRII flow cytometer (BD Biosciences), equipped with 405, 488, and 633 nm lasers. All flow cytometry data was subsequently analyzed using Cytobank software (Mountain View, CA). For PBMCs, compensation was performed using Protein A/G bead standards for all antibodies used. For Pacific Orange dye, a mixture PBMCs with and without the dye was used. A compensation matrix was made within Cytobank. All images were acquired with a Marianas Spinning Disk Confocal microscope (Zeiss, Oberkochen, Germany), using the aforementioned primary antibody clones followed by incubation with fluorescent secondary antibodies

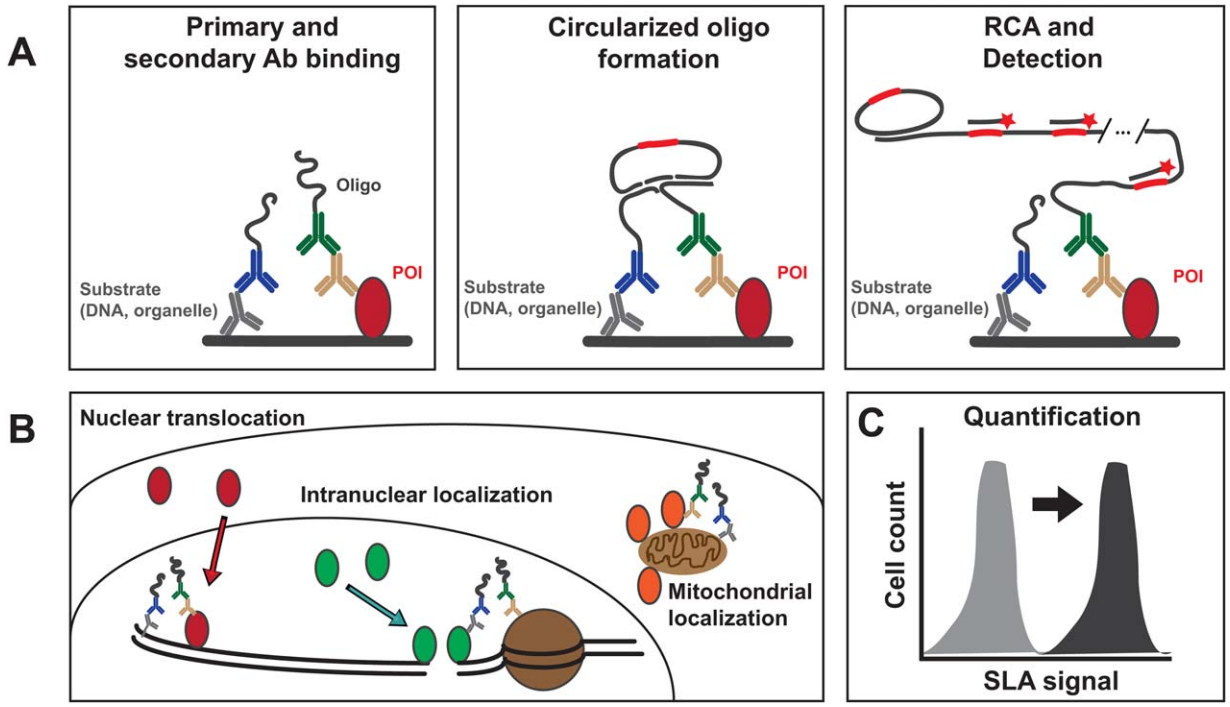

Figure 1. SLA detects localization to distinct subcellular structures in single cells. (**A**) Working principle. Antibodies (Abs) to protein of interest (POI) and abundant material in organelle of interest are bound by oligonucleotide (oligo)-conjugated secondary antibodies. When secondary antibodies are in proximity, oligonucleotides can be circularized, amplified, and detected by fluorophore-conjugated probes. Dotted line indicates the length of the amplified region is much greater than depicted. (**B**) SLA has been optimized to detect nuclear localization, localization to specific regions in the nucleus (damaged DNA), and mitochondrial localization, (**C**) leading to flow cytometric readouts of these aspects of subcellular localization.

conjugated to Alexa-fluor 488 and Alexa-fluor 647 fluorophores (Invitrogen, Carlsbad, CA) for 30 min at room temperature. Following this, cells were counterstained with Hoechst (Life Technologies) for 5 min for cell nuclei. Cell samples (10 μL) were pipetted into wells of a Lab Tek chamber slide (Thermo Fisher Scientific), incubated in the dark for 10 min to allow cells to sink to the bottom of the slide, and imaged using the SlideBook 6.0 software (3i, Denver, CO). Images were further processed using ImageJ software (National Institutes of Health, Bethesda, MD). Bar plots were constructed using the ggplot2 R package.

Statistics

Statistical tests were performed using the stats R package. Specifically, the Welch Two Sample *t* test was used, and all tests were two-tailed. For time-course experiments shown in Figure 3, data were transformed by the inverse hyperbolic sine (arcsinh), and therefore, compared in arcsinh space. This is similar to a log transformation done on flow cytometry data to make relationships between expression levels and biological conditions more clear. The arcsinh transformation and its comparison to log transformation is described in previous work from our lab (9), and additional work comparing different data transformations commonly used in flow cytometry (12).

Results

The SLA Approach

SLA uses the Proximity Ligation Assay (7,13–18) to bring protein subcellular localization, normally accounted for by visual and spatial observation, to the traditionally non-visual flow cytometer. Proximity ligation assays traditionally measure protein-protein interactions via antibodies against the respective proteins of interest. Here, this method is adapted such that one antibody is against an abundant macromolecule marking an organelle or cell structure of interest. These antibodies are bound by oligonucleotide-conjugated secondary antibodies used for proximity detection (Fig. 1A, left panel). If the two secondary antibodies are within 40 nanometers of each other (7), the reaction proceeds and the product can be measured either by microscopy or flow cytometry with fluorophore-conjugated detection oligonucleotides (Fig. 1A, middle and right panel).

Measuring Transcription Factor Localization to Organelles

In initial experiments, SLA was used to measure the nuclear import, and presumed DNA binding, of the p65/RelA subunit of transcription factor NF-κB by quantifying its interaction with an antibody against dsDNA used previously (8). In these experiments, proximity probes for the interaction between CD45 and Histone H3 (Supporting

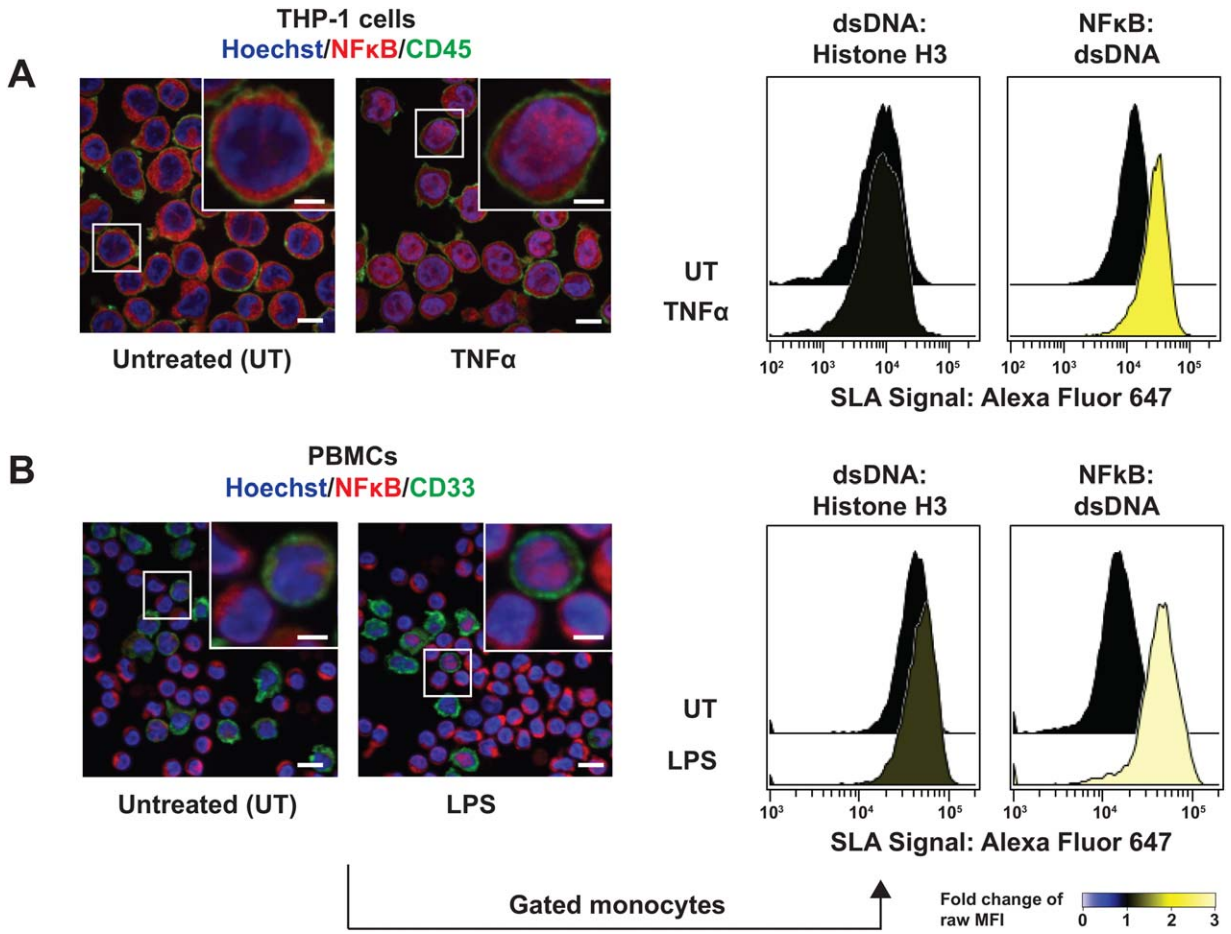

Figure 2. SLA detects nuclear import of NF-κB in cell lines and primary samples. (**A**) Confocal microscopy (left) and SLA (right) in THP-1 monocytic cell line. Magnified image in upper right is of boxed cells. DNA was stained with Hoechst (blue), and CD45 (green) was used as a cell surface marker. SLA readouts are for the dsDNA-histone H3 interaction (not expected to be affected by TNFα), and NF-κB and dsDNA interaction in THP-1 cells. (**B**) Confocal microscopy (left) and SLA (right) for NF-κB in PBMCs, illustrated as in (A) with CD33 is used as a monocyte marker. Scale bars represent 10 μm (main images), 4 μm (insets).

Information Fig. S1A) (not expected to interact), and proximity probes for the expected interaction between dsDNA and Histone H3 (Fig. 2) were used as controls, where the signal was not expected to change between untreated and treated conditions. Nuclear import of p65/RelA (which will be referred to as NF-κB) was induced by treatment with NF-κB pathway activator tumor necrosis factor alpha (TNFα) (Fig. 2B, Supporting Information Fig. S1A). SLA detected an increase in nuclear NF-κB for both cell lines and gated monocytes from human PBMCs, consistent with what was observed by IFM of traditional fluorescent antibody staining (Fig. 2A).

Additionally, SLA was used to measure nuclear import of transcription factor NFAT in the Jurkat T cell line upon combined treatment of NFAT pathway activators phorbol-12-myristate-13-acetate (PMA) and Ionomycin (Supporting Information Fig. S2). Here, treatment with PMA and Ionomycin led to a strong increase in nuclear NFAT SLA signal both in Jurkat cell lines and lymphocytes gated out of healthy human PBMCs. Of note, $CD3^+$ T cells appeared to have a unanimous increase in SLA signal, suggesting that the nuclear NFAT translocation behavior is sufficiently similar among the numerous T cell subsets therein that they cannot be distinguished by these conditions. On the contrary, two populations were observed in $CD3^-$ lymphocytes after PMA and Ionomycin, suggesting diversity of nuclear NFAT translocation behavior among the remaining cell subsets (e.g., B cells, Natural Killer cells) under these conditions.

To test the efficacy of SLA on other macromolecular structures, mitochondrial localization of cytochrome C was measured using a pair of antibodies against cytochrome C and mitochondrial protein COXIV (Fig. 1B, Supporting Information Fig. S1B). The NF-κB interaction with Cytochrome C was used as a negative control. Here, a small subset of cells had an increased SLA signal for this interaction (though still very low). Given the weakness of signal, this is likely due to experimental background noise, but it could also be due to NF-κB protein existing in or near the mitochondria of these cells, which has been reported previously (19).

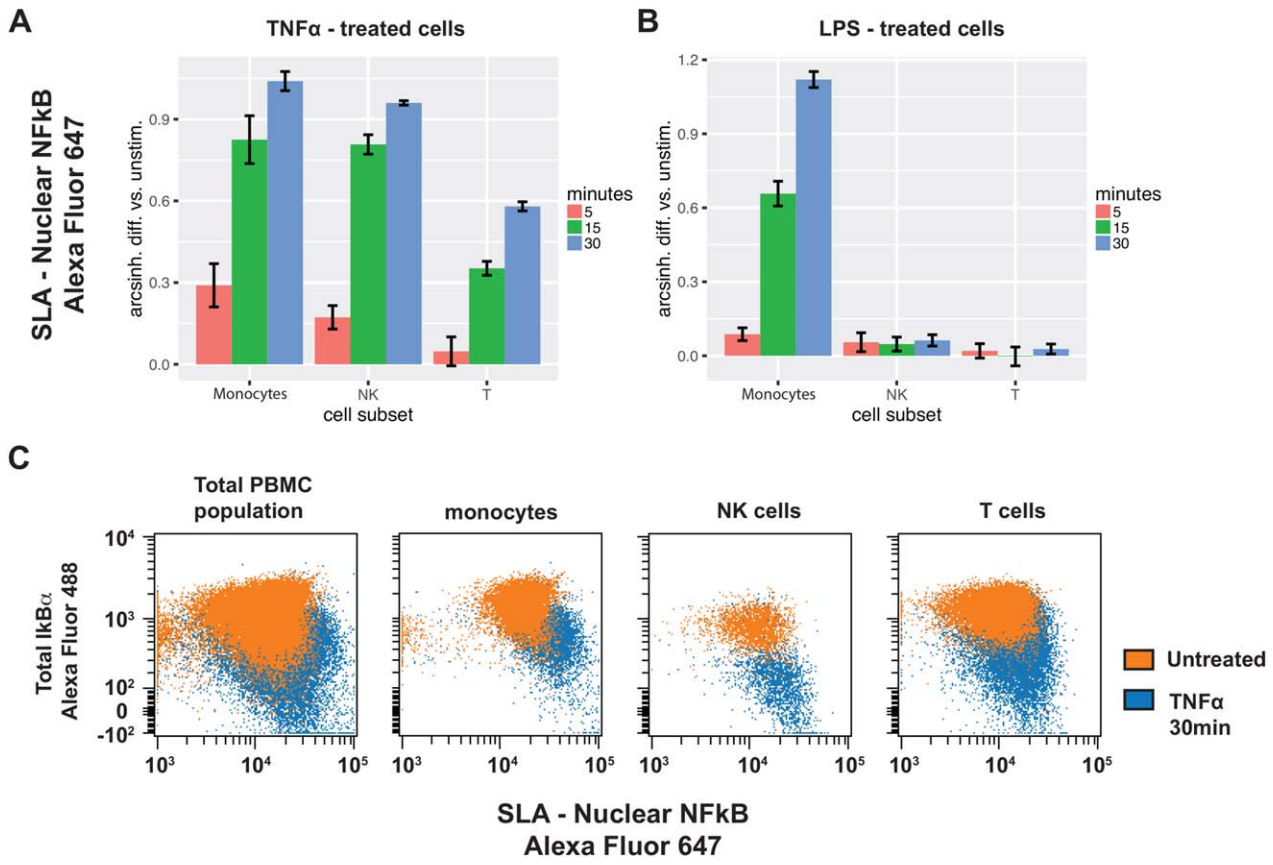

Figure 3. NF-κB nuclear import kinetics and its relationship with total IκBα in single cells across multiple cell subsets in PBMCs. (**A**) Time course experiment in which PBMCs were treated with TNFα for 5, 15, or 30 min. SLA for the NF-κB and dsDNA interaction is indicated as "nuclear NF-κB." NF-κB nuclear translocation was calculated as the difference of inverse hyperbolic sine (arcsinh) medians of the indicated timepoint post-treatment compared to that timepoint's untreated control. Bars represent the mean ± SEM ($n = 4$) (**B**) Same experimental setup as (A), but using LPS as the pathway activator. (**C**) SLA for nuclear NF-κB with simultaneous intracellular antibody staining for negative regulator IκBα reveals their relationship at the single-cell level across multiple cell subsets.

IFM with fluorescent staining of the same primary antibodies validated the results for the aforementioned localizations (Supporting Information Figs. S1–S4). Taken together, these experiments demonstrated that SLA measures protein localization to multiple intracellular locales by flow cytometry.

Profiling Nuclear Localization across Cell Subsets in Primary Samples

Given SLA was validated above in cell lines, we leveraged the throughput of the method to interrogate transcription factor nuclear localization across multiple cell subsets in complex primary samples. SLA was adapted for use with primary PBMCs from healthy human donors. Light forward and side scatter properties were maintained by following the SLA protocol, which allowed for singlet and monocyte/lymphocyte cell gating. The protocol was adapted to include staining with antibodies that had been previously selected to delineate specific immune cell subsets (Supporting Information Fig. S3). In addition to TNFα, bacterial LPS was used as a NF-κB pathway activator to induce nuclear import of NF-κB exclusively in monocytes (20).

SLA revealed differences in NF-κB nuclear translocation across cell subsets and between stimulation conditions. While TNFα led to nuclear import of NF-κB in both monocyte and lymphocyte cell subsets, LPS led to nuclear import exclusively in monocytes (Figs. 3A and 3B). By comparing SLA activity across multiple time points in arcsinh space (9), we observed that NF-κB response kinetics in PBMCs differed across pathway activation conditions and cell types. For example, in both TNFα and LPS treated monocytes, we observed an initial increase in nuclear NF-κB levels in the first 15 min after treatment. TNFα treated cells had only a 25% additional increase in nuclear import between 15 and 30 min (Fig. 3A, Supporting Information Table S1), whereas LPS-treated monocytes had an additional 70% increase in nuclear NF-κB levels between 15 and 30 min (Fig. 3B, Supporting Information Table S1). These results suggest that nuclear import of NF-κB in monocytes is more gradual when induced by LPS, as opposed to TNFα. These observations are consistent with and build upon previous nuclear NF-κB kinetics studies done in

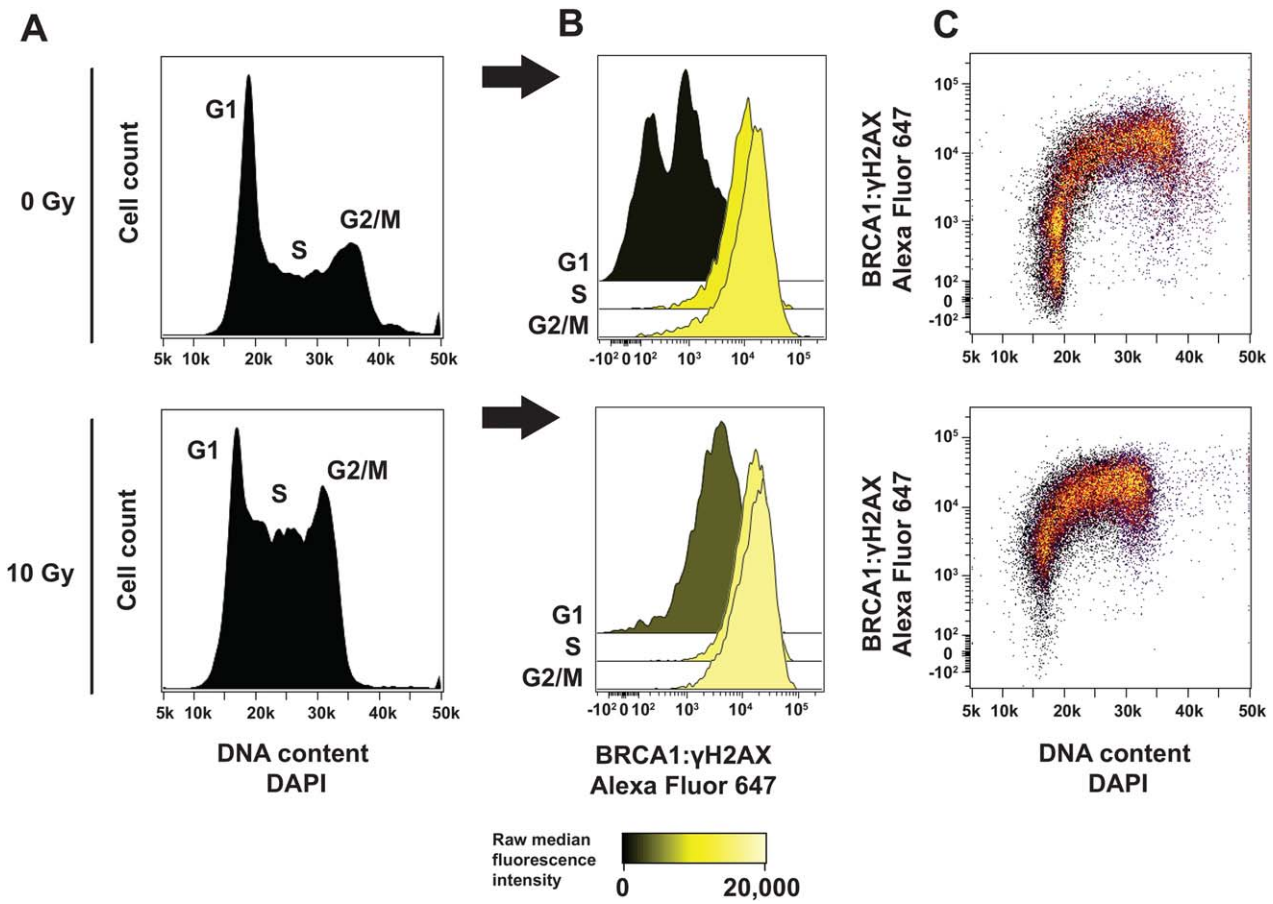

Figure 4. SLA quantifies BRCA1 localization to DNA damage sites. (**A**) Cells were either untreated (top) or irradiated (bottom), and stained with DAPI for DNA content during the SLA procedure to gate between G1, S, and G2/M phase. (**B**) Gating reveals differences in the BRCA1-γH2AX interaction between cell cycle phases. (**C**) Dot plots reveal single-cell topology of the BRCA1-γH2AX interaction as a function of the cell cycle.

vitro (21). Such differences in NF-κB response kinetics were observed across cell types even within the same pathway activation conditions. Between TNFα-treated cell subsets, monocyte and NK cells exhibited a more rapid response than T cells. Following an initial increase in nuclear NF-κB levels in the first 15 min of treatment, NK cells had only a 19% increase in nuclear NF-κB levels between 15 and 30 min. In contrast, T cells had an additional 66% increase in nuclear NF-κB levels between 15 and 30 min (Fig. 3A, Supporting Information Table S1). Taken together, SLA revealed that the kinetics of NF-κB nuclear translocation differ across multiple cell subsets, multiple conditions, and multiple time points in complex primary samples.

The NF-κB pathway is negatively regulated by IκBα, which sequesters NF-κB in the cytoplasm until pathway activation leads to the degradation of NF-κB (22,23). To determine if IκBα showed the expected kinetics relative to p65/RelA release into the nucleus, we simultaneously performed SLA with intracellular staining of total IκBα. We confirmed the inverse relationship between nuclear NF-κB and total IκBα at the single-cell level, as the median fluorescence intensities of the former increased and the latter decreased upon treatment with TNFα or LPS (Fig. 3C). These results demonstrate SLA's ability to interrogate nuclear localization simultaneously with upstream regulators of a cell-signaling pathway.

SLA also quantified NFAT nuclear translocation in PBMCs treated with PMA and Ionomycin, with nuclear import of NFAT being detected in T-cells but not monocytes (Supporting Information Fig. S2B). These results taken together with those for nuclear NF-κB suggest SLA can be a versatile determinant of regional localization and complex formation in primary samples.

Measuring Intranuclear Relocalization to Damaged DNA

While transcription factor binding is a global event that occurs across multiple target loci, it was important to determine if SLA could be used to assay for other, less frequent, cellular events. We therefore sought to quantify DNA repair in terms of specific proteins localized to damaged DNA (Fig. 1B). Traditional identification and quantification of DNA lesions is accomplished by assaying DNA repair foci with microscopy (Supporting Information Fig. S4) (24,25), which is not (under most circumstances) considered a high throughput regime. We focused on the tumor suppressor BRCA1,

which forms intranuclear foci both in S-phase and upon DNA damage induction (24,26,27). BRCA1 is essential for the end-resection step of DNA double-stranded break repair by homologous recombination (28). DNA double-strand breaks are marked by phosphorylation of nearby Histone H2AX proteins at Serine 139 (γH2AX)[3]. As such, when DNA is being repaired by homologous recombination, BRCA1 will localize to the DNA damage site in proximity to γH2AX. Therefore, SLA provides a convenient means to measure this specific DNA repair mechanism and others like it by measuring proximity of specific DNA repair proteins (in this case, BRCA1) to γH2AX at the single-cell level (Fig. 4).

It is known that the DNA double-stranded break repair mechanisms are regulated differently at distinct phases of the cell cycle (29). We therefore added a simultaneous DAPI stain (DNA content per cell) which allows for visualization of the cell cycle (Fig. 4A) (30). To detect exclusively chromatin-bound BRCA1 in proximity to γH2AX, we utilized a detergent pre-extraction protocol which removes proteins from the nucleus which are not chromatin-bound (10).

We observed a BRCA1-γH2AX interaction signal that was significantly higher in S and G2 phases of untreated cells (Fig. 4B, Supporting Information Fig. S6, Supporting Information Table S2). These results recapitulated previous IFM observations from foci counting (24). SLA was able to quantify this interaction in 20,000 cells in under a minute. Of note, there appeared to be two peaks in the SLA signal for untreated cells in G1, suggesting that this particular interaction (though relatively low) may vary in a discrete manner across G1 (Fig. 4B). Dot plots with SLA signal and DAPI provided a more detailed interpretation of the relationship between the BRCA1-γH2AX interaction by visualizing the cell cycle as a continuum rather than a series of gates (Fig. 4C). We further confirmed that the levels of the BRCA1-γH2AX interaction (SLA signal) differ from the individual protein levels of BRCA1 and γH2AX across the cell cycle. This highlights the additional layer of information one can obtain from measuring interactions in this manner (Fig. 4, Supporting Information Fig. S5).

To induce DNA double-strand breaks and subsequent repair, we treated cells with ionizing radiation (IR) (31). In these irradiated cells, the G1 specific BRCA1-γH2AX interaction was significantly higher than that of untreated cells (Fig. 4B, Supporting Information Fig. S6, Supporting Information Table S2). This was an unexpected result, given that BRCA1 co-localization with γH2AX as viewed with microscopy is typically observed in S/G2 phase and not G1 (24). These data suggest that BRCA1 may be playing a role in IR-specific DNA repair in G1 as well. Furthermore, these data suggest that SLA has sufficient resolution to identify interactions that are either novel or difficult to detect by microscopy.

Taken together, these results demonstrate SLA can provide a high-throughput and quantitative readout of co-localization that can compliment classical lower throughput methods such as IFM-based foci counting. Furthermore, SLA can be enhanced with DAPI staining for cell cycle and detergent pre-extraction for detecting only chromatin-bound nuclear proteins.

Discussion

SLA enables measurements of spatial localization with a resolution of 40 nm and a throughput of thousands of cells per second. SLA can be performed simultaneously with surface and intracellular antibody staining, allowing for interrogation of subcellular localization across multiple subpopulations in complex samples, like human PBMCs.

SLA allowed for the interrogation of pathway activation in terms of transcription factor nuclear localization across tens of thousands of cells. In this study, we identified differences in NF-κB signaling kinetics across cell subsets of human PBMCs stimulated by TNFα or LPS (Fig. 2). Furthermore, SLA allows for one to study the relationship between nuclear localization of a transcription factor and activation of upstream regulatory proteins in a signaling pathway, as we investigated with NF-κB and IκBα (Fig. 2).

The combination of SLA with surface antibodies allows for this method to be expanded to complex primary samples without the need for cell sorting. Given SLA was optimized in this report in healthy human PBMCs, this method should be readily expandable to study immune signaling dysregulation in disease. Signaling in tissue specimens may be studied with SLA as well, though one must optimize single-cell suspension to retain cell surface markers of interest.

We further used SLA to study the DNA damage response through the proximity of DNA repair protein BRCA1 and DNA damage marker γH2AX across the cell cycle in the TYK-nu ovarian cancer cell line. We showed the cells in S/G2 have higher levels of BRCA1 localized to γH2AX, as compared to cells in G1. This interaction was expected given that BRCA1 plays a role in the end-resection step of homologous recombination repair in S/G2 (32,33). Furthermore, IR treatment led to increased localization of BRCA1 to γH2AX in G1 as well. Our data suggest that BRCA1 could be playing a role in G1-specific DNA repair, such as non-homologous end joining (33), in ovarian cancer cells.

The protocol modifications specific to studying the DNA damage response have potential for studying additional biological phenomena. SLA was adapted for a simultaneous DAPI stain for cell cycle analysis without the need for cell cycle-specific markers or thymidine analog (e.g., BrdU) treatment. This modification allows for study of cell cycle-specific mechanisms, like the shuttling of cyclins in and out of the nucleus (34,35).

Furthermore, SLA was optimized for compatibility with detergent pre-extraction of cells to study exclusively chromatin-bound nuclear proteins. Thus, one can robustly interrogate complexes and structures across various contexts and across the cell cycle. These readouts have strong potential in clinical settings, where reliance on low-throughput methods such as foci-counting with microscopy is the current gold-standard for measuring DNA repair mechanisms important for targeted cancer therapy (29,36,37).

As needed, SLA readouts of multiple simultaneous interactions could be achieved using unique backbone and insert sequences for each antibody pair of interest that will bind

detection oligonucleotides with different fluorophores, as demonstrated in recent work from our lab (17). Taken together, by adapting Proximity Ligation Assay to study subcellular localization with flow cytometry, one can interrogate a variety of biological phenomena with quantitative single-cell resolution and high throughput, including but not limited to transcription factor dynamics and DNA repair.

Acknowledgments

We would like to acknowledge Alex Loktev in the lab of Peter Jackson at Stanford University for his assistance with the confocal microscopy in this manuscript, and the laboratory of Peter Jackson for allowing us to use their confocal microscope accordingly. We would like to acknowledge Alan Ashworth at UCSF, for his expert feedback throughout the DNA damage section of this project and Markus Covert for his expert feedback on the NF-κB signaling work.

This work was supported by the US National Institutes of Health, grants R33CA0183692, U19AI057229, 1U19AI100627, 7500108142, R01CA184968, 1R33 CA183654-01, 1R01GM10983601, 1R21CA183660, 1R01NS08953301, 5UH2AR067676, 1R01CA19665701, R01HL120724, N01-HV-00242 HHSN26820100034C, 41000411217, 5R01AI073724, U54-UCA149145A (to G.P.N); US Department of Defense Congressionally Directed Medical Research Programs, grants OC110674, W81XWH-14-1-0180 (to G.P.N); Bill and Melinda Gates Foundation, grant OPP1113682 (to G.P.N); Pfizer, Inc, grant 123214 (to G.P.N); US Food and Drug Administration, grants BAA-15-00121, HHSF223201210194C (to G.P.N); Novartis Pharmaceuticals Corp, grant CMEK162AUS06T (to G.P.N); Juno Therapeutics Inc, grant 122401 (to G.P.N); California Institute for Regenerative Medicine, grant DR1-01477 (to G.P.N); Gilead Sciences, Inc. Research Agreement (to G.P.N); NWCRA Entertainment Industry Foundation (to G.P.N); DiaTools, grant 259796 (to G.P.N); Cancer Biology Training Grant, grant 2T32CA009302-36A1 (to T.J.B); and the Rachford and Carlota A. Harris Endowed Chair (to G.P.N.).

Author Contributions

T.J.B. conceived and designed the method, drove the project's direction, and wrote the manuscript. A.P.F. and P.F.G. adapted the general Proximity Ligation method to flow cytometry for SLA. F.A.B. designed PBMC time-course experiments. J.E.B. conceived and validated the idea to study the relationship between nuclear NF-κB and IκBα. Y.Y adapted SLA for use in PBMCs. J.M.Y. validated idea to study the relationship between nuclear NF-κB and IκBα. A.R.G validated cell stimulatory conditions for foundational SLA experiments. S.C.K. performed time-course SLA experiments in PBMCs. V.D.G designed experiments and validated antibodies for SLA directed at DNA repair. W.J.F designed experiments for SLA directed at DNA repair and edited the manuscript. G.P.N supervised the work and wrote the manuscript.

Literature Cited

1. Basiji DA, Ortyn WE, Liang L, Venkatachalam V, Morrissey P. Cellular image analysis and imaging by flow cytometry. Clin Lab Med 2007;27:653–670.
2. Bendall SC, Nolan GP, Roederer M, Chattopadhyay PK. A deep profiler's guide to cytometry. Trends Immunol 2012;33:323–332.
3. Irish JM, Hovland R, Krutzik PO, Perez OD, Bruserud O, Gjertsen BT, Nolan GP. Single cell profiling of potentiated phospho-protein networks in cancer cells. Cell 2004;118:217–228.
4. Heim R, Tsien RY. Engineering green fluorescent protein for improved brightness, longer wavelengths and fluorescence resonance energy transfer. Curr Biol 1996;6: 178–182.
5. Rossi F, Charlton CA, Blau HM. Monitoring protein-protein interactions in intact eukaryotic cells by beta-galactosidase complementation. Proc Natl Acad Sci USA 1997;94:8405–8410.
6. Ramdzan YM, Polling S, Chia CPZ, Ng IHW, Ormsby AR, Croft NP, Purcell AW, Bogoyevitch MA, Ng DCH, Gleeson PA, et al. Tracking protein aggregation and mislocalization in cells with flow cytometry. Nat Methods 2012;9:467–470.
7. Söderberg O, Gullberg M, Jarvius M, Ridderstråle K, Leuchowius K-J, Jarvius J, Wester K, Hydbring P, Bahram F, Larsson L-G, et al. Direct observation of individual endogenous protein complexes in situ by proximity ligation. Nat Methods 2006;3: 995–1000.
8. Angelo M, Bendall SC, Finck R, Hale MB, Hitzman C, Borowsky AD, Levenson RM, Lowe JB, Liu SD, Zhao S, et al. Multiplexed ion beam imaging of human breast tumors. Nat Med 2014;20:436–442.
9. Bendall SC, Simonds EF, Qiu P, Amir E-AD, Krutzik PO, Finck R, Bruggner RV, Melamed R, Trejo A, Ornatsky OI, et al. Single-cell mass cytometry of differential immune and drug responses across a human hematopoietic continuum. Science 2011;332:687–696.
10. Jackson SP, Forment JV. A flow cytometry–based method to simplify the analysis and quantification of protein association to chromatin in mammalian cells. Nat Protocols 2015;10:1297–1307.
11. Krutzik PO, Clutter MR, Trejo A, Nolan GP. Fluorescent Cell Barcoding for Multiplex Flow Cytometry. Hoboken, NJ: Wiley; 2001:1–22. 22 p.
12. Finak G, Perez J-M, Weng A, Gottardo R. Optimizing transformations for automated, high throughput analysis of flow cytometry data. BMC Bioinf 2010;11: 546–513.
13. Leuchowius K-J, Clausson C-M, Grannas K, Erbilgin Y, Botling J, Zieba A, Landegren U, Söderberg O. Parallel visualization of multiple protein complexes in individual cells in tumor tissue. Mol Cell Proteomics 2013;12:1563–1571.
14. Weibrecht I, Gavrilovic M, Lindbom L, Landegren U, Wählby C, Söderberg O. Visualising individual sequence-specific protein–DNA interactions in situ. New Biotechnol 2012;29:589–598.
15. Weibrecht I, Lundin E, Kiflemariam S, Mignardi M, Grundberg I, Larsson C, Koos BOR, Nilsson M, Söderberg O. In situ detection of individual mRNA molecules and protein complexes or post-translational modifications using padlock probes combined with the in situ proximity ligation assay. Nat Protocols 2013;8:355–372.
16. Leuchowius K-J, Weibrecht I, Landegren U, Gedda L, Söderberg O. Flow cytometric in situproximity ligation analyses of protein interactions and post-translational modification of the epidermal growth factor receptor family. Cytometry Part A 2009; 75A:833–839.
17. Frei AP, Bava F-A, Zunder ER, Hsieh EWY, Chen S-Y, Nolan GP, Gherardini PF. Highly multiplexed simultaneous detection of RNAs and proteins in single cells. Nat Methods 2016;13:269–275.
18. Jarvius M, Paulsson J, Weibrecht I, Leuchowius K-J, Andersson A-C, Wählby C, Gullberg M, Botling J, Sjöblom T, Markova B, et al. In situ detection of phosphorylated platelet-derived growth factor receptor beta using a generalized proximity ligation method. Mol Cell Proteomics 2007;6:1500–1509.
19. Johnson RF, Perkins ND. Nuclear factor-κB, p53, and mitochondria: Regulation of cellular metabolism and the Warburg effect. Trends Biochem Sci 2012;37: 317–324.
20. Sabroe I, Jones EC, Usher LR, Whyte MKB, Dower SK. Toll-like receptor (TLR)2 and TLR4 in human peripheral blood granulocytes: A critical role for monocytes in leukocyte lipopolysaccharide responses. J Immunol 2002;168:4701–4710.
21. Tay S, Hughey JJ, Lee TK, Lipniacki T, Quake SR, Covert MW. Single-cell NF. Nature 2010;466:267–271.
22. Nolan GP, Ghosh S, Liou H-C, Tempst P, Baltimore D. DNA binding and IκB inhibition of the cloned p65 subunit of NF-κB, a rel-related polypeptide. Cell 1991;64: 961–969.
23. Scott ML, Fujita T, Liou HC, Nolan GP, Baltimore D. The p65 subunit of NF-kappa B regulates I kappa B by two distinct mechanisms. Genes Dev 1993;7:1266–1276.
24. Feng L, Li N, Li Y, Wang J, Gao M, Wang W, Chen J. Cell cycle-dependent inhibition of 53BP1 signaling by BRCA1. Nature Publishing Group 2015:1:15019.
25. Tarsounas M, Davies D, West SC. BRCA2-dependent and independent formation of RAD51 nuclear foci. Oncogene 2003;22:1115–1123.
26. Scully R, Chen J, Ochs RL, Keegan K, Hoekstra M, Feunteun J, Livingston DM. Dynamic changes of BRCA1 subnuclear location and phosphorylation state are initiated by DNA damage. Cell 1997;90:425–435.
27. Pageau GJ, Lawrence JB. BRCA1 foci in normal S-phase nuclei are linked to interphase centromeres and replication of pericentric heterochromatin. J Cell Biol 2006; 175:693–701.
28. Lord CJ, Ashworth A. BRCAness revisited. Nature Reviews Cancer: Nature Publishing Group; 2016. pp.1–11.
29. Turner N, Tutt A, Ashworth A. Hallmarks of "BRCAness" in sporadic cancers. Nat Rev Cancer 2004;4:814–819.
30. Krishan A. Rapid flow cytofluorometric analysis of mammalian cell cycle by propidium iodide staining. J Cell Biol 1975;66:188–193.

31. Ward JF. DNA damage produced by ionizing radiation in mammalian cells: Identities, mechanisms of formation, and reparability. Prog Nucl Acid Res Mol Biol 1988;35:95–125.
32. Cruz-García A, López-Saavedra A, Huertas P. BRCA1 accelerates CtIP-mediated DNA-end resection. Cell Rep 2014;9:451–459.
33. Bunting SF, CallEn E, Wong N, Chen H-T, Polato F, Gunn A, Bothmer A, Feldhahn N, Fernandez-Capetillo O, Cao L, et al. 53BP1 inhibits homologous recombination in Brca1-deficient cells by blocking resection of DNA breaks. Cell 2010;141:243–254.
34. Yang J, Bardes ES, Moore JD, Brennan J, Powers MA, Kornbluth S. Control of cyclin B1 localization through regulated binding of the nuclear export factor CRM1. Genes Dev 1998;12:2131–2143.
35. Shimura T, Kobayashi J, Komatsu K, Kunugita N. DNA damage signaling guards against perturbation of cyclin D1 expression triggered by low-dose long-term fractionated radiation. Oncogenesis 2014;3:e132–e138.
36. Graeser M, McCarthy A, Lord CJ, Savage K, Hills M, Salter J, Orr N, Parton M, Smith IE, Reis-Filho JS, et al. A marker of homologous recombination predicts pathologic complete response to neoadjuvant chemotherapy in primary breast cancer. Clin Cancer Res 2010;16:6159–6168.
37. Farmer H, McCabe N, Lord CJ, Tutt ANJ, Johnson DA, Richardson TB, Santarosa M, Dillon KJ, Hickson I, Knights C, et al. Targeting the DNA repair defect in BRCA mutant cells as a therapeutic strategy. Nature 2005;434:917–921.

Participants & Other Collaborating Organizations

Name:	Veronica Gonzalez, Ph.D.
Project Role:	Senior Research Scientist
Researcher Identifier (e.g. ORCID ID):	N/A
Nearest person month worked:	2.4 Calendar months
Contribution to Project:	Dr. Gonzalez helped drive the project over the years. Designed and performed experiments, analyzed data, co-wrote manuscript that came out of the study.
Funding Support:	

Name:	Ying—Wen Huang MS
Project Role:	Life Science Research Scientist
Researcher Identifier (e.g. ORCID ID):	N/A
Nearest person month worked:	12 Calendar Months
Contribution to Project:	Performed experiments and contributed to manuscripts.
Funding Support:	

Name:	Benjamin Neel, Ph.D.
Project Role:	Co-Investigator
Researcher Identifier (e.g. ORCID ID):	0000-0002-9589-585X
Nearest person month worked:	
Contribution to Project:	Dr. Neel will be responsible for the successful completion of all of the xenograft studies proposed in this application. He will be directly involved in experimental design, data analysis, and determining the timetable for completion of the proposed work.
Funding Support:	

Name:	Dana Pe’er, Ph.D.
Project Role:	Collaborating PI
Researcher Identifier (e.g. ORCID ID):	0000-0002-9259-8817
Nearest person month worked:	
Contribution to Project:	The PI will develop the algorithms along with the postdoc and oversee the entire contribution of the Pe'er lab to this project.
Funding Support:	

Name:	Wendy Fantl
Project Role:	Co-PI
Researcher Identifier (e.g. ORCID ID):	0000-0003-3452-7292
Nearest person month worked:	2.4 Calendar months
Contribution to Project:	Overall direction of project and regular updates with Dr. Nolan.
Funding Support:	

Name:	Garry P. Nolan, Ph.D.
Project Role:	PI
Researcher Identifier (e.g. ORCID ID):	N/A
Nearest person month worked:	0.6 Calendar months
Contribution to Project:	Dr. Nolan oversaw the project.
Funding Support:	